N O T I C E

THIS DOCUMENT HAS BEEN REPRODUCED FROM MICROFICHE. ALTHOUGH IT IS RECOGNIZED THAT CERTAIN PORTIONS ARE ILLEGIBLE, IT IS BEING RELEASED IN THE INTEREST OF MAKING AVAILABLE AS MUCH INFORMATION AS POSSIBLE

(NASA-CR-161451) SPECTROPHOTOVOLTAIC ORBITAL POWER GENERATION Final Report, Aug. 1979 - Feb. 1980 (Honeywell, Inc.) 195 p HC A09/MF A01 CSCL 10A
N80-24757
Unclas
G3/44 20989

SPECTROPHOTOVOLTAIC ORBITAL POWER GENERATION

FINAL REPORT

February 1980

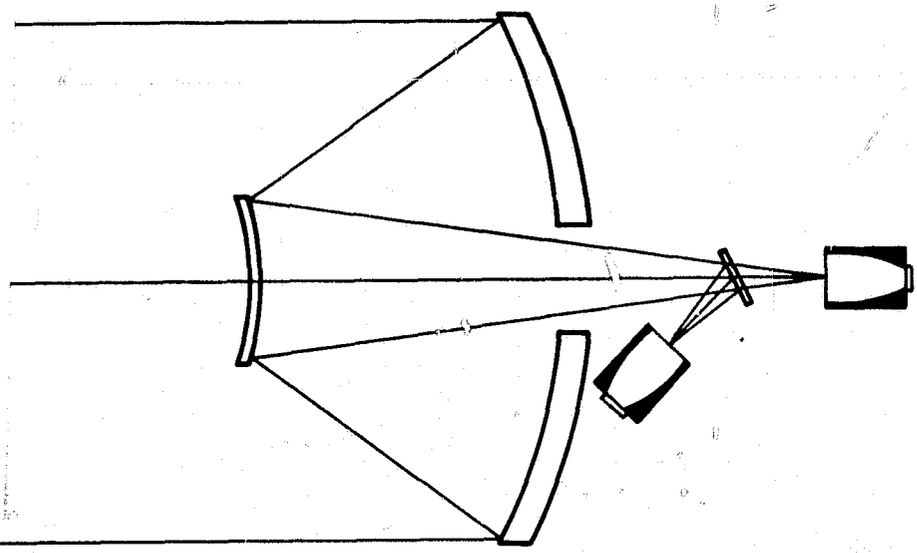

for

GEORGE C. MARSHALL SPACE FLIGHT CENTER

Contract NAS 8-33511

by

Honeywell, Inc.
Systems and Research Center
2600 Ridgway Parkway
Minneapolis, Minnesota 55413

SPECTROPHOTOVOLTAIC ORBITAL POWER GENERATION

FINAL REPORT

February 1980

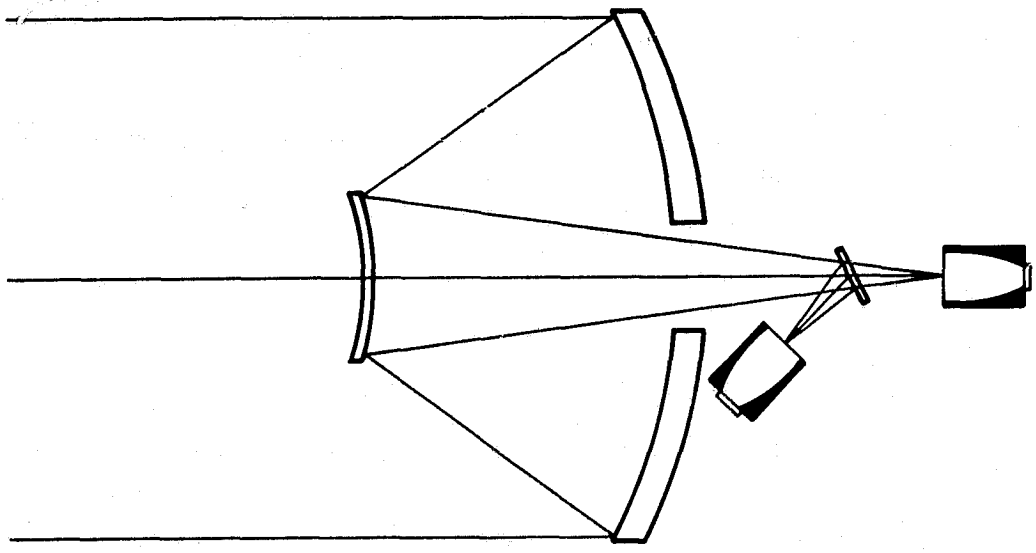

for

GEORGE C. MARSHALL SPACE FLIGHT CENTER

Contract NAS 8-33511

by

Honeywell, Inc.
Systems and Research Center
2600 Ridgway Parkway
Minneapolis, Minnesota 55413

FOREWORD

This report summarizes the results obtained during the first phase of the Spectrophotovoltaic Orbital Power Generation program for NASA/George C. Marshall Space Flight Center. The purpose of the program is to define a spectrophotovoltaic approach that offers a significant overall improvement over conventional array technology.

An analysis was performed showing the feasibility of a spectrophotovoltaic orbital power generation system that optically concentrates solar energy. A dichroic beam-splitting mirror is used to divide the solar spectrum into two wavebands. Absorption of these wavebands by GaAs and Si solar cell arrays with matched energy bandgaps increases the cell efficiency while decreasing the amount of heat that must be rejected. The projected cost per peak watt of this system is $\$2.50/W_p$.

Joan R. Onffroy of Honeywell's Systems and Research Center (SRC) organized this report, with support from the project team at SRC. Dave Stoltzmann did the optical design; Ray Lin did the beam-splitter design; Gary Knowles did the thermal analysis; and Joan Onffroy did the solar cell analysis and system-level trade-off analysis. This report was edited by Chris Johnston.

The Spectrophotovoltaic Orbital Power Generation Program is under the sponsorship and direction of NASA/George C. Marshall Space Flight Center, Huntsville, Alabama. Mr. W.L. Crabtree of that agency is the designated Principal Representative of the Contracting Officer for this program, Mr. E.M. Harper.

PRECEDING PAGE BLANK NOT FILMED

CONTENTS

Section		Page
1	INTRODUCTION AND SUMMARY	1
2	CONCENTRATION OPTICS	7
	2.1 Design Parameters for the Cassegrain Telescope	9
	2.2 Design Parameters for the CPC	16
	2.3 Collector/Concentrator Optical Design	20
	2.3.1 Cassegrain Surface Tolerance Analysis	24
	2.4 System Comparisons	27
3	DICHROIC MIRROR BEAM SPLITTER	42
	3.1 Design Concept	43
	3.2 Selection of Coating Materials	45
	3.3 Beam Splitter Design and Performance Predictions	50
4	SOLAR CELLS	64
	4.1 Methodology for Predicting Solar Cell Performance	65
	4.1.1 Multi-Solar-Cell System Efficiency	65
	4.1.2 Power Maximization for a Given Photocurrent	67
	4.1.3 Diode Dark Current	70
	4.2 Identification of Optimum Bandgaps for One-, Two-, Three-, and Four-Solar-Cell Systems	72
	4.2.1 Calculation of Output Power as a Function of Photocurrent	72

PRECEDING PAGE BLANK NOT FILMED

CONTENTS (continued)

Section			Page
	4.2.2	Calculation of the Photocurrent	74
	4.2.3	Calculation of the Ideal Efficiencies for Multi-Cell Systems	76
	4.2.4	Results for One-Cell Systems	77
	4.2.5	Results for Two-Cell Systems	79
	4.2.6	Results for Three-Cell Systems	85
	4.2.7	Results for Four-Cell Systems	87
	4.2.8	Comparison of One-, Two-, Three-, and Four-Cell Systems	92
	4.2.9	Comparison of Optimum Bandgaps and Those Determined by an Equal-Current Requirement	93
	4.3	Validity of Using the Low-Injection Approximation for 1000-Sun Intensities	96
	4.3.1	Methodology	96
	4.3.2	Si n/p Cell	98
	4.3.3	GaAs p/n Cell	99
	4.4	Evaluation of Multi-Cell Systems Composed of Ge, Si, GaAs, and GaP Solar Cells	101
5	SYSTEM TRADE-OFF ANALYSIS		127
	5.1	Limits on System Parameters	127
	5.2	Component Cost Estimates	131

CONTENTS (concluded)

Section		Page
	5.3 Selection of an Optical System	136
	5.4 Selection of Candidate Solar-Cell/ Beam-Splitter Systems	146
	5.5 Impact of New Solar Cell Development on Total System Cost	150
6	FINAL DESIGN OF OPTIMUM SYSTEM	158
	6.1 Optical Design	158
	6.2 Thermal Design Analysis	169
REFERENCES		181

LIST OF ILLUSTRATIONS

Figure		Page
1	Schematic of Optical System	8
2	Basic Cassegrain Telescope Schematic	10
3	Typical Three-Cell System Schematic	14
4	Beam Splitter and CPC Layouts for Different f-Numbers in a Three-Cell System	17
5	CPC and the Coordinate System for Describing a CPC Concentrator	18
6	Cassegrain Concentration Ratio Dependence on System f-Number	28
7	Axial Separation Between the Image Plane and the Primary Mirror as a Function of System f-Number	30
8	Beam-Splitter Area as a Function of System f-Number	31
9	System Length Dependence on f-Number and f_1/D_1	32
10	Secondary Mirror Magnification Dependence on System f-Number and f_1/D_1	33
11	Secondary Mirror Diameter Dependence on System f-Number and Primary Mirror Focal Length f_1/D_1 for Multi-Cell Systems	34
12	Obscuration Efficiency Dependence on System f-Number and f_1/D_1	36
13	CPC Concentration Ratio Dependence on System f-Number and Primary Mirror Local Length f_1 for Multi-Cell Systems	38

LIST OF ILLUSTRATIONS (continued)

Figure		Page
14	Solar Cell Area Dependence on System f-Number and f_1	39
15	CPC Area Dependence on f-Number	40
16	Spectrum-Splitting Concept for Three-Cell Configuration	44
17	Refractive Index vs Transmission Cut-Off Wavelength for Several UV-Transparent Materials	47
18	Relative Power Spectral Response of GaP, GaAs, and Si Solar Cells	51
19	Details of the 43-Layer ThO_2/MgF_2 Beam-Splitter Coating Design (t = physical thickness)	52
20	Computed Spectral Reflectance of a 0.3 to 0.5 μm Reflective ThO_2/MgF_2 Beam Splitter (43-layer double stack, θ = 0 deg)	53
21	Computed Spectral Reflectance of a 0.3 to 0.5 μm Reflective ThO_2/MgF_2 Beam Splitter (43-layer double stack, θ = 22 deg)	54
22	Computed Spectral Reflectance of a 0.3 to 0.5 μm Reflective ThO_2/MgF_2 Beam Splitter (43-layer double stack, θ = 45 deg)	55
23	Computed Spectral Reflectance of a 0.9 to 1.1 μm Reflective MgF_2/TiO_2 Beam Splitter (21 layers, θ = 0 deg)	57
24	Details of the 21-Layer MgF_2/TiO_2 Beam-Splitter Coating Design (t = physical thickness)	58
25	Details of the 24-Layer MgF_2/TiO_2 Beam-Splitter Coating Design (t = physical thickness)	58

LIST OF ILLUSTRATIONS (continued)

Figure		Page
26	Computed Spectral Reflectance of a 0.9 to 1.1 μm Reflective MgF_2/TiO_2 Beam Splitter (24 layers, θ = 0 deg)	59
27	Computed Spectral Reflectance of a 0.9 to 1.1 μm Reflective MgF_2/TiO_2 Beam Splitter (24 layers, θ = 22 deg)	60
28	Computed Spectral Reflectance of a 0.9 to 1.1 μm Reflective MgF_2/TiO_2 Beam Splitter (24 layers, θ = 45 deg)	61
29	Details of the 24-Layer SiO_2/ThO_2 Beam-Splitter Coating Design (t = physical thickness)	62
30	Computed Spectral Reflectance of a 0.9 to 1.1 μm Reflective SiO_2/ThO_2 Beam Splitter (24 layers, θ = 22 deg)	63
31	Equivalent Circuit of a Solar Cell	68
32	Maximum Photocurrent for a Given Energy Gap for AM0 Conditions	75
33	Output Power as a Function of Photocurrent for Si, Ge, and GaAs Solar Cells (T = 300K, R_sA_d = 0 and 0.01Ω-cm^2)	78
34	Ideal Efficiency for a One-Cell System as a Function of Energy Bandgap	79
35	Output Power as a Function of Silicon Photocurrent for Two- and Three-Cell Configurations (T = 300K, R_sA_d = 0, AM0)	80
36	Efficiency of a Two-Cell System for GaAs Conditions as a Function of the Higher Energy Bandgap	82
37	Efficiency of a Two-Cell System for Si Conditions as a Function of the Higher Energy Bandgap	82

LIST OF ILLUSTRATIONS (continued)

Figure		Page
38	Efficiency of a Two-Cell System: 1) Si Conditions for $E_g < 1.3$ eV and 2) GaAs Conditions for $E_g \geq 1.3$ eV as a Function of the Higher Energy Bandgap	83
39	Range of Energy Bandgaps for a Two-Cell System in Which the Efficiency is Greater than 40%	84
40	Efficiency for a Three-Cell System as a Function of Highest Energy Gap	86
41	Efficiency of a Three-Cell System as a Function of Lowest Energy Bandgap	88
42	Efficiency of a Four-Cell System for Si/GaAs Conditions as a Function of Highest Energy Bandgap	89
43	Efficiency of a Four-Cell System as a Function of Lowest Energy Bandgap	91
44	Ideal Efficiency of a Multi-Solar-Cell System Composed of One, Two, Three, and Four Solar Cells	92
45	Efficiency Comparison of Si/GaAs Conditions for Two-, Three-, and Four-Cell Systems; for Which 1) the Currents from All Cells are Required to Be Equal and 2) there is No Restriction on Currents	94
46	Intrinsic Absorption Coefficients of Ge, Si, GaAs, and GaP	106
47	Calculated Spectral Responses of Ge, Si, GaAs, and GaP	107
48	Output Power as a Function of Photocurrent for Ge, Si, GaAs, and GaP Solar Cells ($T = 300K$, $R_s A_d = 0$)	110

LIST OF ILLUSTRATIONS (continued)

Figure		Page
49	Minimum Beam-Splitter Areas Allowed for $T_{bs} \leq 350°C$	130
50	Normalized Output Power (P_{out}/D_1^2) where D_1^2 is in Square Meters as a Function of System f-Number and Primary Focal Length (f_1)	138
51	Normalized Cost of the Secondary Mirror as a Function of System f-Number and Primary Focal Length (f_1)	140
52	Normalized Cost of Radiator as a Function of System f-Number and Primary Focal Length (f_1)	141
53	Normalized Cost of CPCs as a Function of System f-Number	142
54	Normalized Cost of the Beam Splitters as a Function of System f-Number	143
55	Normalized Cost of the Solar Cells as a Function of System f-Number and Primary Focal Length (f_1)	144
56	Normalized System Cost as a Function of System f-Number and Primary Focal Length (f_1)	145
57	System Cost per Peak Watt as a Function of System f-Number and Primary Focal Length, f_1	147
58	Breakdown of System Costs as a Function of f-Number for a Primary Focal Length of $f_1/D_1 = 0.7$	148
59	System Costs per Peak Watt of the Best Candidate Systems	155
60	Estimate of Total Cost per Peak Watt of a GeAs/Ge System as a Function of the Number of 100-kW Systems to Be Built	157

LIST OF ILLUSTRATIONS (concluded)

Figure		Page
61	Final Optical System Design Schematic	159
62	Optical Layout for Solar Concentrator	161
63	On-Axis Bundle Ray Trace	163
64	Off-Axis Bundle Ray Trace	164
65	Final System Design CPC Profile, Scaled to Primary Diameter = 1	165
66	Solar Cell Mount Cross-Section	170
67	Placement of Solar Cells within the Focal Plane	170
68	Radiator Panel Location	177

LIST OF TABLES

Table		Page
1	Cassegrain and CPC Parameters Based on Ideal System Concentration of 1000 Suns	23
2	Dependence of System Parameters on System f-Number, f_1/D_1, and Number of Cells	41
3	Key Properties of Candidate Coating Materials	48
4	Device Parameters	73
5	Additional Device Parameters	74
6	Optimum Bandgaps and Maximum Efficiencies for Two-Cell Systems	83
7	Optimum Bandgaps and Maximum Efficiencies for Three-Cell Systems	85
8	Optimum Bandgaps and Maximum Efficiencies for Four-Cell Systems	90
9	Optimum Energy Bands and Maximum Efficiencies for 1000 Suns, AM0 Conditions	93
10	Candidate Materials and Predicted Efficiencies for 1000 Suns, AM0 Conditions	94
11	Bandgaps and Efficiencies of Solar Cells Connected in Series	95
12	Excess Carrier Densities for Silicon n/p Solar Cells	100
13	Excess Carrier Densities for Gallium Arsenide p/n Solar Cells	100
14	Structure Factors	103

LIST OF TABLES (concluded)

Table		Page
15	Device Modeling Parameters	105
16	Absorption Factors	108
17	Results for One-Cell Configurations	111
18	Results for Two-Cell Configurations	112
19	Results for Three-Cell Configurations	114
20	Results for Four-Cell Configurations	118
21	Cost of Systems Requiring No New Solar Cell Development	149
22	Cost of Systems Requiring Development of One New Solar Cell	151
23	Cost of Systems Requiring Development of Two New Solar Cells	153
24	Solar Concentrator Final Design	167
25	Solar Cell Mount Component Dimensions	171
26	Conductive Temperature Drops Within the Solar Cell Mount	172
27	Freon-21 Transport Property Data Near T = 270K	

SECTION 1

INTRODUCTION AND SUMMARY

The purpose of the Spectrophotovoltaic Orbital Power Generation program is to define a spectrophotovoltaic approach that offers a significant overall improvement over conventional array technology in the production of power space applications.

Small amounts of electrical power sufficient for the needs of most earth satellites are supplied by arrays of solar cells in a flat plate configuration. Projections of this concept consider increased power levels, from a fraction of a kilowatt to multikilowatt levels and further to megawatt and gigawatt output for transmission to Earth. The existing arrays, with a moderate number of solar cells, grow with these projections into enormous arrays of cells with spectacular cost and weight.

Cell number, cost, and weight can be reduced by using high-efficiency solar cells and by using optical elements to concentrate the solar energy. This report summarizes the results of a feasibility analysis which predicts that a considerable savings can be obtained with a multi-cell approach for systems with 100-kW output levels.

In our proposed concept the solar energy is concentrated by a two-stage optical system with an effective concentration ratio of 1000 to 1. The first concentration stage employs a Cassegrain telescope. The output from this stage is spectrally split by a dichroic beam splitter. The two bands are

then directed to two compound parabolic concentrators which comprise the second stage of concentration. A trade-off analysis was performed to determine the most cost-effective system. This system is composed of a Cassegrain which has an effective system f-number of 3.5 and a primary which has an f-number of 0.7. The concentration ratios of the Cassegrain and the compound parabolic concentrators are 270 and 4.6, respectively. The product of the concentration ratios was taken to be greater than 1000 in order to compensate for inefficiencies in the optics. The solar cell arrays chosen for the system are GaAs and Si. For a 100-kW output level the primary mirror diameter is 20.43m and the solar cell array diameters are 57.6 cm. The predicted cost per peak watt is $\$2.50/W_p$, with most of the cost being for the primary mirror and the radiator, which is used to hold the solar cell array temperatures at 300K.

Our feasibility analysis consisted of 1) a study of various collector/concentrator concepts, 2) a design of two beam splitters for a candidate three-cell system, GaP/Si/GaAs, 3) an analysis of ideal efficiencies for one-, two-, three-, and four-cell systems in order to determine optimum solar cell bandgaps, 4) a more realistic calculation of the potential efficiencies of solar cell systems composed of Ge, Si, GaAs, and GaP, 5) a trade-off analysis to determine the most cost-effective system, and 6) a preliminary design of the optimum system.

The candidate collector/concentrator concepts are discussed in Section 2. The design parameters for the Cassegrain and the compound parabolic concentrators were used to generate numerous system configurations for comparison in the subsequent cost trade-off analysis. The beam-splitter areas and the system length were minimized with the constraint that adequate

clearance be allowed for the housing of the compound parabolic concentrators. All length dimensions of the system were normalized to the diameter of the primary mirror. Each of the design parameters was calculated as a function of system f-number and primary mirror f-number, which was limited to a minimum of f/0.7. The Cassegrain concentration ratio decreases dramatically with f-number while the CPC area and the axial separation between the primary mirror and the image plane increase. The beam-splitter area is a minimum at f/3.5. The secondary mirror diameter decreases with system f-number while the solar cell area increases. All areas and length, except the solar cell area, increase as the primary mirror f-number increases.

The beam-splitter designs are described in Section 3. In order to demonstrate the feasibility of using dichroic mirrors for splitting the solar spectrum, two beam splitters were designed for a candidate three-cell configuration--GaP/Si/GaAs. The basic requirements of a beam splitter to be used in a high-concentration solar-cell system include a transparent substrate, beam-splitting coatings applied to the front side of the substrate, and wideband antireflection coatings applied to the back side of the substrate. Fused silica is a good candidate material for the substrate because of its transmitting properties and its high thermal stability. The beam-splitter coatings consist of multilayer stacks of transparent dielectric materials. By depositing alternating high- and low-refractive-index layers onto silica substrates, very high reflectivities can be achieved over a well-defined spectral region. The spectral width of the reflection band is determined by the ratio of refractive indexes used in the stack.

The first beam splitter reflects 0.3- to 0.5-μm radiation to the GaP solar cell while transmitting the longer wavelengths. Its coating is a 43-layer double stack of ThO_2/MgF_2 that is resistant to ultraviolet radiation. The second beam splitter reflects 0.9- to 1.1-μm radiation to the Si solar cell and transmits both the shorter wavelengths from 0.5 to 0.9 μm and the longer wavelengths beyond 1.1 μm. Its coating is a 24-layer stack of MgF_2/TiO_2. A 22-deg incident angle is required to keep the reflection bands sharp.

Solar-cell/beam-splitter system efficiencies are addressed in Section 4. Efficiencies were calculated for one-, two-, three-, and four-cell solar-cell/beam-splitter systems. It was assumed that 1000 suns under AM0 conditions are incident on the solar cells, less any losses due to the beam splitters, and that the solar cells are held at a temperature of 300K. Ideal maximum efficiencies were calculated in order to determine the optimum bandgaps. These efficiencies ranged from 32% for a one-cell system to 53% for a four-cell system.

Although it is possible to fabricate semiconductors with nearly any bandgap, it is more cost-effective to use materials which have already been developed for solar cell applications. Also ideal efficiencies close to the maximum ones can be obtained with some of these well-developed materials. The ideal efficiencies, such as those calculated here and also presented in the literature, are extremely optimistic. For realistic predictions, losses due to nonunity spectral response, grid shadowing, cell reflection, and the dichroic mirrors must be taken into account.

For the reasons stated in the preceding paragraph, more realistic calculations were made for solar-cell systems using Ge, Si, GaAs, and GaP. Although Ge and GaP are not well-developed solar cells, they were chosen because both materials have been well studied. Germanium transistors were used before Si electronics were developed, and GaP is used in light-emitting diodes and visible radiation detection. Efficiency and excess power removal requirements were determined for all possible systems using these materials as solar cells. The efficiencies ranged from 23.7% for a one-cell system to 33.3% for a four-cell system.

In Section 5 the trade-off analysis, which was used to determine the most cost-effective optical and solar-cell/beam-splitter system, is described. Realistic cost estimates were made for the optics, solar cells, and beam splitters. The costs per peak watt of all system configurations described above were calculated. The two-cell systems were found to be more cost-effective than those with more or less cells. With exclusion of the cost of development of new solar cells, a GaAs/Ge system was found to have the smallest cost per peak watt--$\$2.35/W_p$. However, for a GaAs/Si system, for which high-efficiency solar cells are already well developed, the cost per peak watt was found to be $\$2.50/W_p$. The impact of new solar cell development on total system cost was evaluated by considering the number of systems to be built. It was assumed that each unit would have a 100-kW output power level. For Ge solar-cell-development costs ranging from $2M to $5M it was found that 143 to 357 GaAs/Ge systems would have to be built in order for these systems to be competitive with GaAs/Si systems. It was concluded that for near-term applications GaAs/Si systems are the most cost-effective. However, new solar cells are currently being developed which

have more optimum energy bandgaps; this technology should be pursued in order to lower the cost of solar power even further.

The final system design is presented in Section 6. A performance analysis of the optical system shows that it is capable of concentrating the solar energy on the solar cell arrays with a concentration ratio of 1000 to 1. The possibility of using fresnel lenses for the Cassegrain is discussed. A preliminary thermal design analysis was conducted to provide sizing and performance data which could be used in the optimization of the system mount and radiator design. A non-optimized concept was analyzed in order to illustrate the methodology required to predict performance.

SECTION 2

CONCENTRATION OPTICS

A survey of collector-concentrator concepts was conducted. In order to meet the desired system concentration ratio of 1000, a two-stage concentration system concept was required. The first concentration stage was chosen to be a Cassegrain telescope because this type of optics keeps the collector close to the spacecraft. The second stage of concentration employs a compound parabolic concentrator (CPC). A schematic of a typical three-cell system is shown in Figure 1.

In order to obtain an energy concentration ratio of 1000 on the solar cells, less any loss due to the beam splitters, the optical concentration ratio was increased to greater than 1000 to account for losses inherent in the optics, such as obscuration in the Cassegrain. This is discussed in more detail in subsection 2.4.

The first-stage concentration of the Cassegrain is the ratio of the area of the entering beam to the area of the image; the second-stage concentration of the CPC is the ratio of the areas of the entrance and exit apertures, assuming the exit aperture is the same size as the solar cell array. For a matched combination of the telescope and the CPC, where the area of the image of the telescope is equal to the entrance aperture of the CPC and the numerical apertures of the two are the same, the resultant optical concentration of the system is the product of the concentration of the

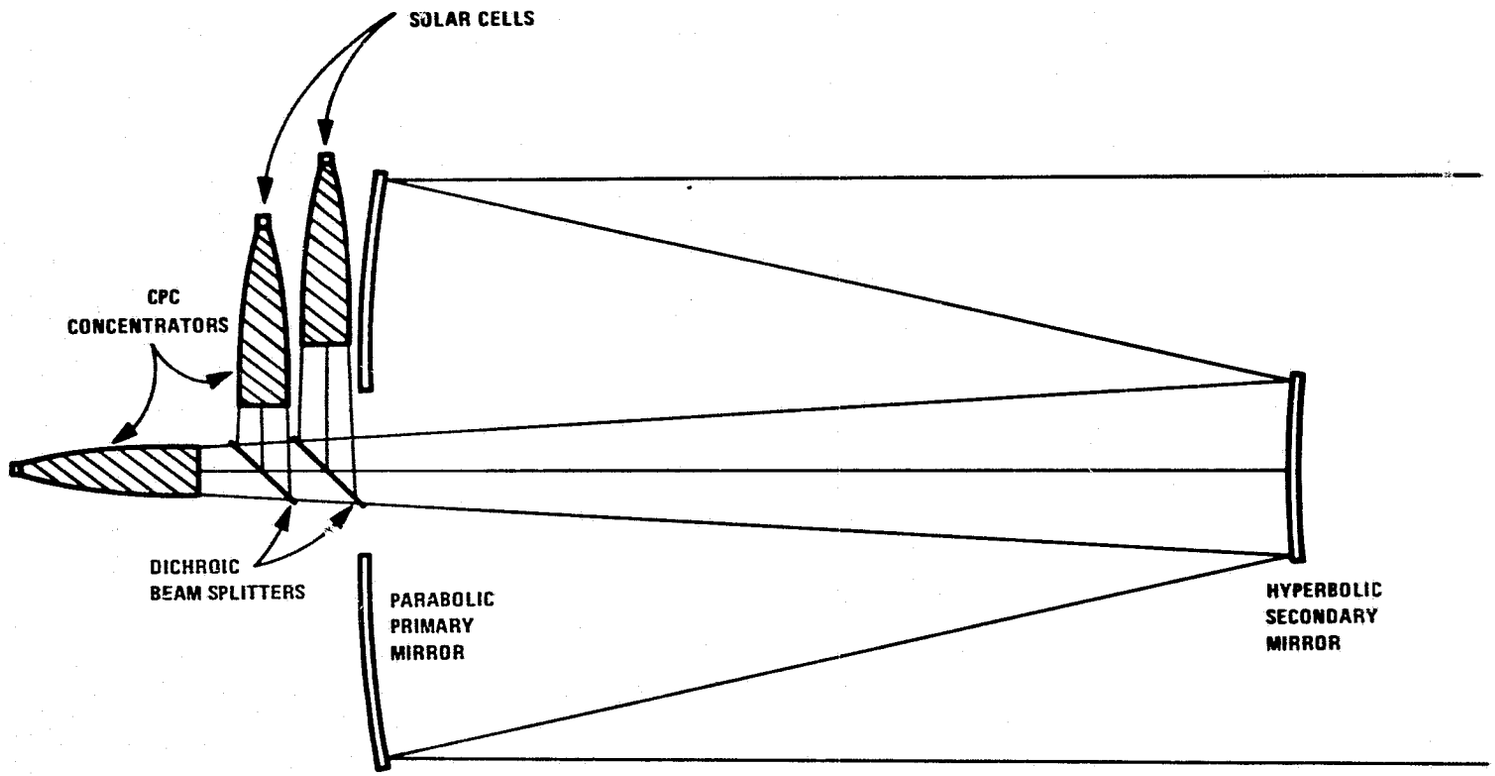

Figure 1. Schematic of Optical System

telescope and that of the CPC. Hence, the optical concentration ratio of the system is the ratio of the area of the entering beam, that is the area of the primary mirror, to the area of the solar cell array. The system concentration ratio, corrected for inefficiencies in the optics, is 1000.

The output from the first stage of concentration is spectrally selected with dichroic beam splitters and directed to individual CPC concentrators. The solar cell associated with each CPC is matched in spectral sensitivity to the output from the dichroic beam splitter.

2.1 DESIGN PARAMETERS FOR THE CASSEGRAIN TELESCOPE

The classical Cassegrain optical system, shown in Figure 2, uses a parabolic primary mirror with a hyperbolic secondary. The following parameters pertain to the design of the Cassegrain:

D_1 = primary mirror diameter

f_1 = primary mirror focal length

D_2 = secondary mirror diameter

f_2 = secondary mirror focal length

t_1 = axial separation between primary and secondary mirrors

t_2 = axial separation between primary mirror and the image plane

β = sun field-of-view (FOV)/2 where $\tan \beta = 0.0087/2$

α = angular degradation factor due to imperfections in the telescope

L_s = image diameter

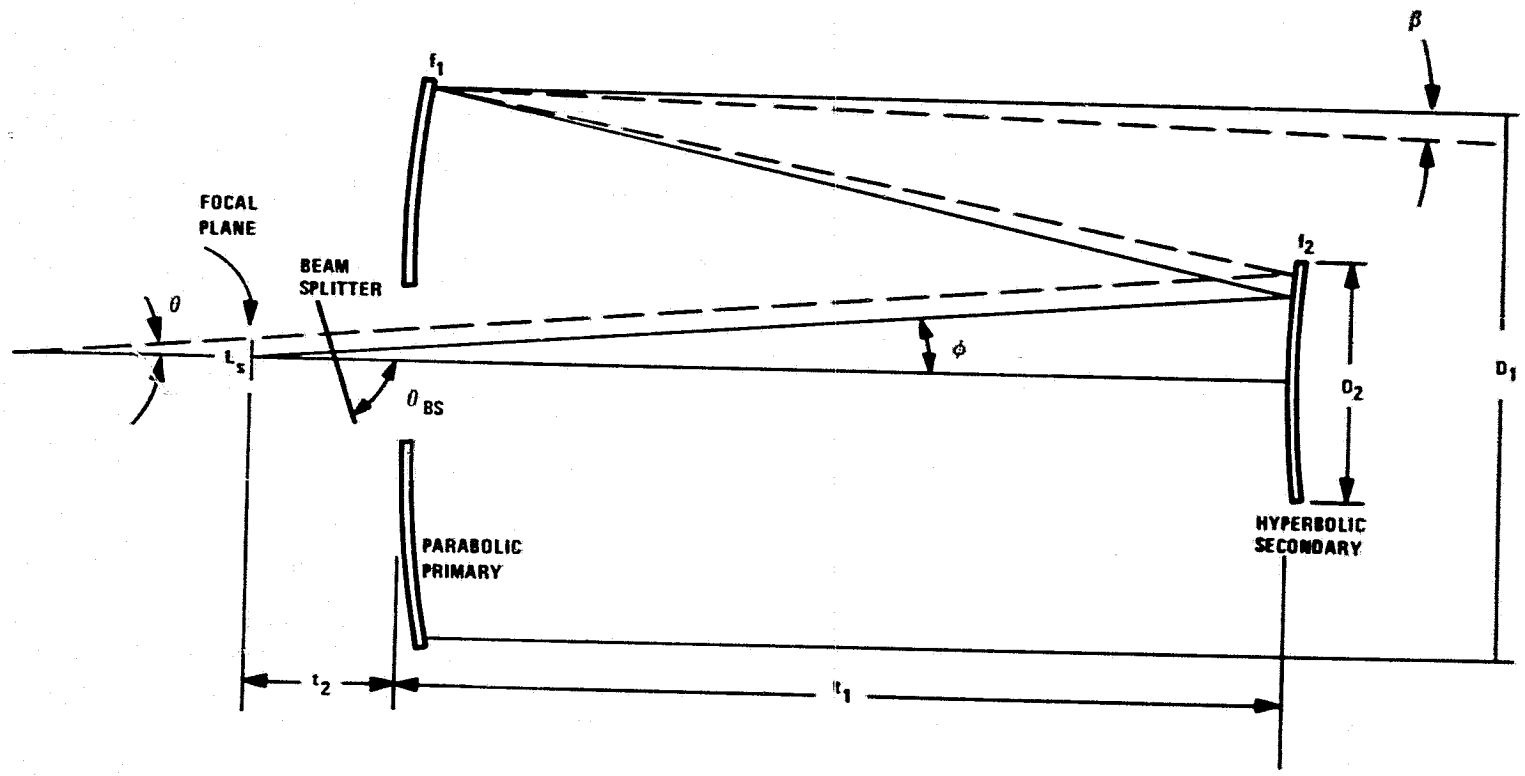

Figure 2. Basic Cassegrain Telescope Schematic

F = focal length of telescope

$f/\#$ = system f-number

θ = semi-angular energy convergence cone of telescope

d = image diameter of sun formed by the primary mirror

m = secondary magnification

θ_{bs} = tilt angle of beam splitters

ϕ = semi-angular axial ray convergence angle

k_1 = conic constant of primary = -1

k_2 = conic constant of secondary

Basically, the telescope images the sun a distance, t_2, behind the primary mirror. The size of the image, L_s, depends on the focal length, F, of the telescope; the sun FOV; and the angular degradation factor, α, due to imperfections in the system. The design of the telescope proceeds with the following parametric equations:

$$F = (t_1 + t_2) \Big/ (1 - t_1/f_1)$$

$$f/\# = F/D_1 = \frac{1}{2 \sin \phi}$$

$$m = F/f_1 = (t_1 + t_2) \Big/ (f_1 - t_1)$$

$$f_2 = \left(\frac{f_1 + t_2}{m + 1}\right) \left(\frac{m}{m - 1}\right)$$

$$d = 2f_1 \, \alpha \tan \beta$$

$$D_2 = \frac{(D_1 - d)(f_1 + t_2)}{F + f_1} + d$$

$$L_s = 2\,\alpha\,F \tan\beta$$

$$k_2 = -\left(\frac{m+1}{m-1}\right)^2$$

$$\text{Obscuration (OBS)} = \left(\frac{D_2}{D_1}\right)^2$$

$$CR_{Cass} = \left(\frac{D_1}{L_s}\right)^2 = \left(\frac{1}{2\,f/\#\,\alpha \tan\beta}\right)^2$$

As an example, consider a 10-meter diameter f/2 primary to be used in an f/4 system having a blur factor $\alpha = 2$ and an image distance $t_2 = 4$m. Then,

$F = 40$m

$f_1 = 20$m

$m = 2$

$f_2 = 16$m

$t_1 = 12$m

$D_2 = 4.21$m

$L_s = 0.70$m

$k_1 = -1$

$k_2 = -9$

$$OBS = 0.18$$

$$CR_{Cass} = 206.43$$

For systems employing a number of dichroic beam splitters, sufficient clearance must be given behind the primary to adequately house the CPCs and assure that the beam splitters do not interfere with each other. Relationships were derived for the distance t_2 so that the size of the beam splitters and the system length are minimized while maintaining sufficient clearance for the CPCs. A typical schematic for a three-cell system is shown in Figure 3. The following equations describe the location and size of the beam splitters for various system f-numbers for two- and three-cell systems.

The semi-angular energy convergence cone is given by

$$\tan\theta = \frac{1}{2f/\#} - \alpha \tan\beta$$

The distance, ℓ, from the tip of the cone to the image, L_s, is given by

$$\frac{\ell}{D_1} = \frac{2(f/\#)^2 \alpha \tan\beta}{1 - 2(f/\#)\alpha \tan\beta}$$

The distances from the image to the center of the first beam splitter, ℓ_1, and the second beam splitter, ℓ_2, are

$$\frac{\ell_1}{D_1} = \frac{\ell}{D_1}\left[\frac{\tan\theta_{bs} + \tan\theta}{1 - \tan\theta \tan\theta_{bs}}\right] \tan\theta$$

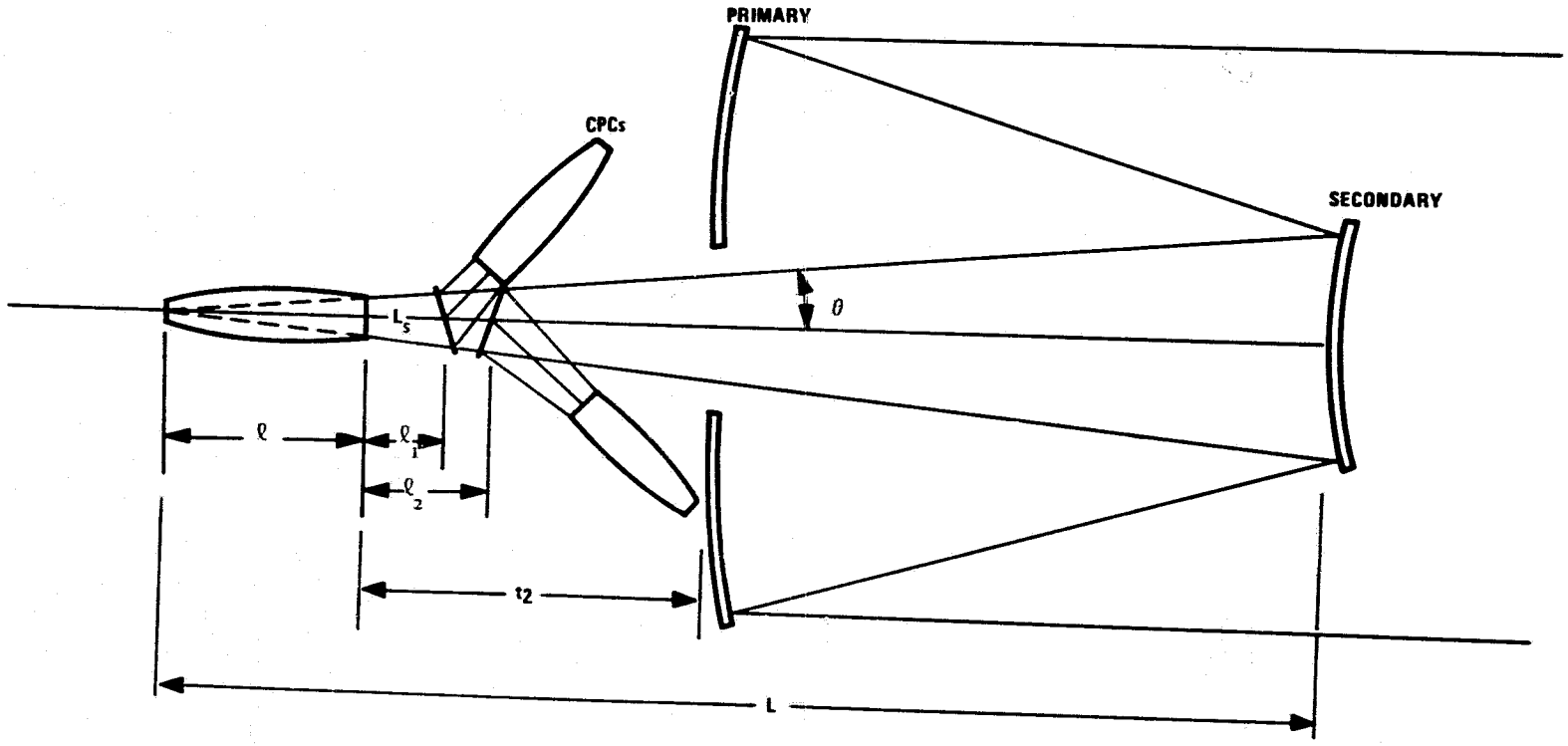

Figure 3. Typical Three-Cell System Schematic

$$\frac{\ell_2}{D_1} = \frac{\ell}{D_1}\left[\frac{2\tan\theta\,\sin\theta_{bs}}{\cos\theta_{bs} - \tan\theta\,\sin\theta_{bs}} - \frac{\tan\theta}{\tan\theta_{bs}}\right]$$

The projections of the light cone on the beam splitters are elliptical with the semi-major axes, a_i, and the semi-minor axes, b_i, given by

$$\frac{a_1}{D_1} = \left[\frac{\ell}{D_1} + \frac{\ell_1}{D_1}\right]\left[\frac{\tan\theta\,\tan\theta_{bs}}{(\tan^2\theta_{bs} - \tan^2\theta)\cos\theta_{bs}}\right]$$

$$\frac{a_2}{D_1} = \left[\frac{\ell}{D_1} + \frac{\ell_2}{D_1}\right]\left[\frac{\tan\theta}{(\tan^2\theta_{bs} - \tan^2\theta)\sin\theta_{bs}}\right]$$

$$b_1 = a_1\sqrt{1 - \cos^2\theta_{bs}/\cos^2\theta}$$

$$b_2 = a_2\sqrt{1 - \cos^2\theta_{bs}/\cos^2\theta}$$

The active area of the beam splitters is elliptical and is given by

$$A_{bs} = \pi ab$$

The configuration of the collector/concentration system is dependent on the number of cells as well as the system f-number, since these two parameters are dominant in determining the required space needed behind the primary for the beam splitters and CPCs. The length L of the system is

$$\frac{L}{D_1} = \left(\frac{f_1 + t_2}{D_1}\right)\left(\frac{f/\#}{f/\# + f_1/D_1}\right)$$

As an example of how the length of the system and the size and positioning of the beam splitters change with the system f-number, Figure 4 shows the beam splitter layout for three different f-numbers in a three-cell system. Note that the shallow cone angle of systems with higher f-numbers requires much more room behind the primary for the beam splitters and CPCs.

2.2 DESIGN PARAMETERS FOR THE CPC

For any angular acceptance, the CPC has been shown by Winston[1] to generate the highest possible concentration. (This angular acceptance also determines to a certain degree the tracking requirements of the system.) All light that enters the CPC at angles less than θ_{max} is accepted and goes to the absorber (solar cell). Radiation outside this acceptance angle is rejected and bounces back and forth between the reflector walls until it emerges again through the top of the CPC. If the incident radiation is uniformly spread over all angles between 0 deg and θ_{max}, then the radiation at the solar cell is totally diffuse. Radiation which is incident at the acceptance angle will be brought to a focus at the edge of the solar cell array. The exit aperture of the CPC can house either the solar cell array or perhaps a medium of index $n > 1$, which increases the concentration by a factor of n^2. The use of such a medium is justified only if radiative heat losses are not important or the cost of the solar cells is high, since the medium does not help to reduce the radiative heat losses. Figure 5 shows the design parameters of a CPC.

---

[1] R. Winston, "Solar Concentrations of a Novel Design," Solar Energy, Vol. 16, 1974, p. 89.

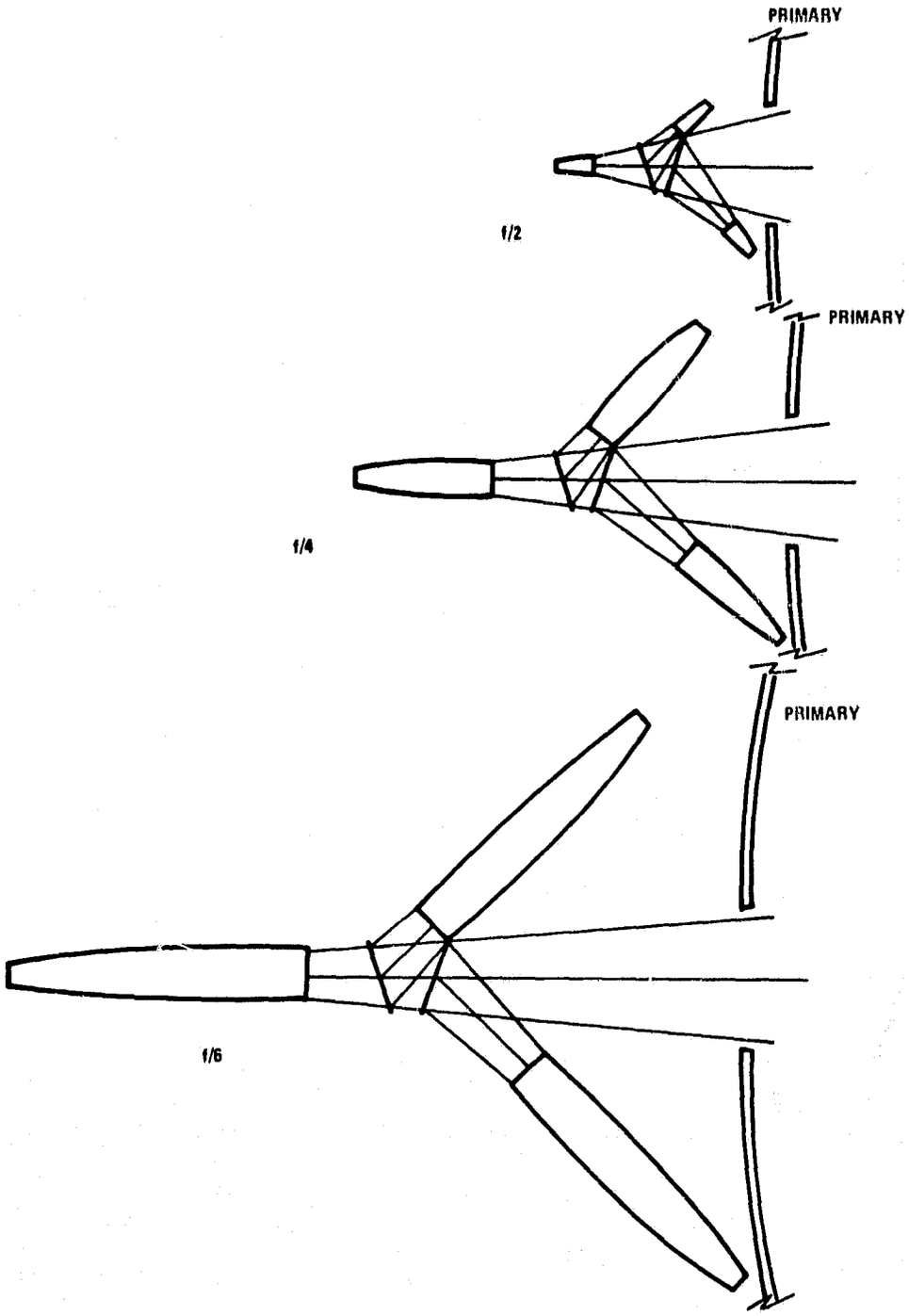

Figure 4. Beam Splitter and CPC Layouts for Different f-Numbers in a Three-Cell System

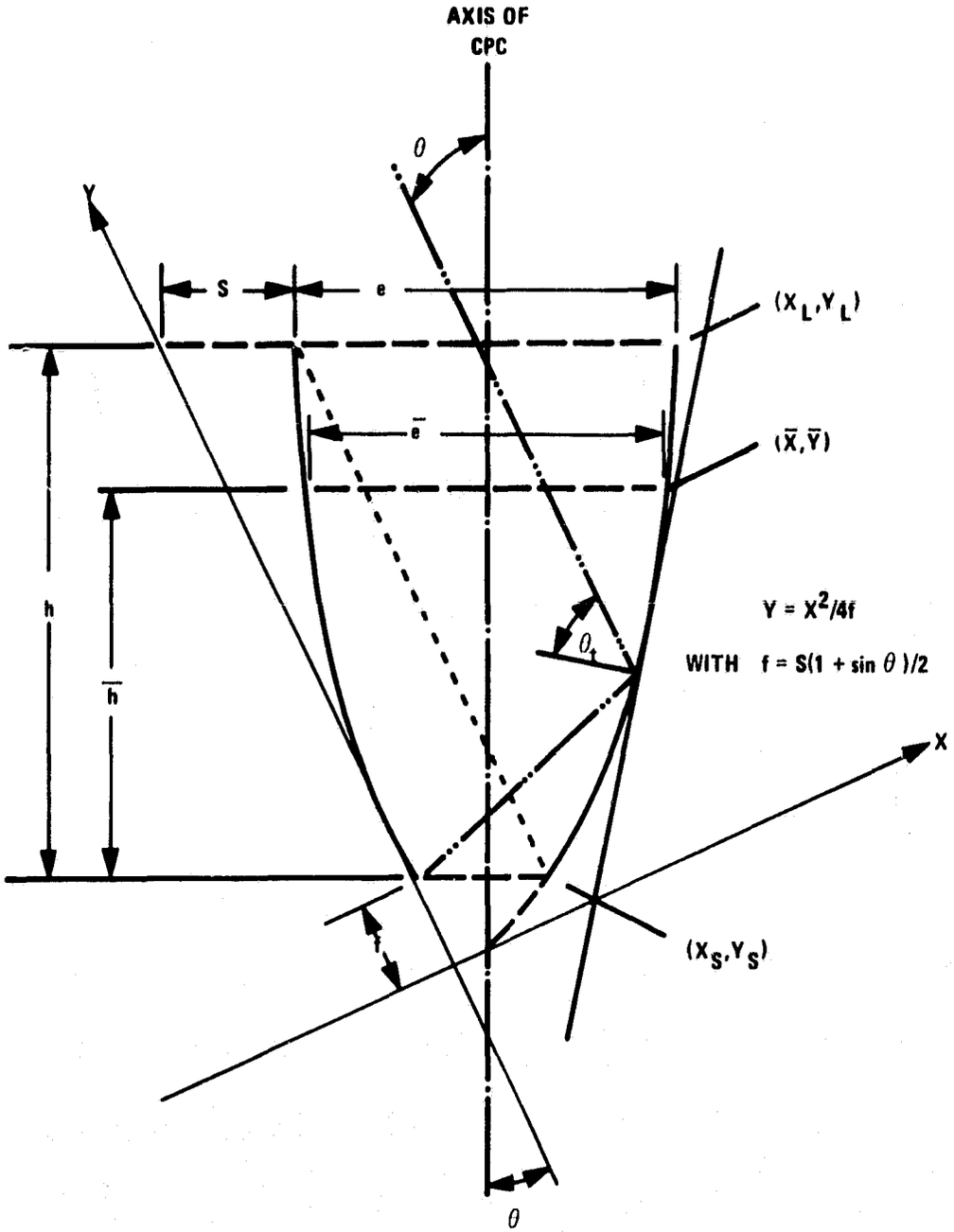

Figure 5. CPC and the Coordinate System for Describing a CPC Concentrator (Barred quantities refer to a truncated CPC.)

Let

d_1 = diameter of the entrance aperture

d_2 = diameter of the absorber (solar cell)

h, e, A_{CPC} = height, width, and area of the reflector

$\langle \eta_i \rangle$ = average number of reflections for a beam reaching the absorber within the acceptance angle θ

Then, we have the following relations:[2]

$$CR_{CPC} = \frac{n^2}{\sin^2\theta}, \quad (n = 1 \text{ for air})$$

$$A_{CPC} = \pi(d_2/2)^2(1 + \sin\theta)\left(\frac{\cos\theta}{\sin^2\theta} + \ln\left\{\frac{(1+\sin\theta)(1+\cos\theta)}{\sin\theta\cos\theta + 2(1+\sin\theta)}\right\} - \frac{\sqrt{2}\cos\theta}{(1+\sin\theta)^{3/2}}\right)$$

$$\langle \eta_i \rangle = \tfrac{1}{2}(1+\sin\theta)\left(\frac{\cos\theta}{\sin^2\theta} + \ln\left\{\frac{(1+\sin\theta)(1+\cos\theta)}{\sin\theta\left[\cos\theta + \sqrt{2(1+\sin\theta)}\right]}\right\} - \frac{\sqrt{2}\cos\theta}{(1+\sin\theta)^{3/2}}\right) - \frac{(1-\sin\theta)(1+2\sin\theta)}{2\sin^2\theta}$$

These equations can be used to determine the parameters for the CPC.

---

[2] A. Rabl, "Optical and Thermal Properties of Compound Parabolic Concentrators," Solar Energy, Vol. 18, 1976, p. 497.

A disadvantage of the CPC is that the reflector area can get very large relative to its entrance aperture. In such cases, a truncated CPC would most likely be used to reduce the reflector area. Generally, a considerable reduction can be achieved with only a minimal amount of energy being lost from the truncated portion. In order to determine an optimum truncation level, a trade-off analysis must be made between the length of the CPC, its reflector area, and its cost.

2.3 COLLECTOR/CONCENTRATOR OPTICAL DESIGN

In order to raytrace any system to verify the collection capabilities, the system surfaces must be recognizable to the computer as standard surface profile representations. The Cassegrain surfaces present no problem but the CPC profile requires special attention. While the CPC has a rotationally symmetric profile, shown in Figure 5, it is generated by the revolution of a tilted and decentered parabolic section about the optical axis. When raytracing in two dimensions, representing this surface profile is slightly complicated but it can be adequately represented and raytraced. This method, however, cannot be used with established raytracing programs for completely general three-dimensional raytracing. Hence one must resort to a different approach, which is described below.

Canning[3] has derived relationships whereby the CPC can be represented by an elliptical profile. This ellipse can be revolved about the optical axis to produce an ellipsoid of revolution, thus allowing raytracing in three dimensions. Given a concentration ratio in two dimensions for the CPC

[3] John S. Canning, "The Winston Solar Concentrator Described as an Ellipse," Solar Energy, Vol. 18, 1976, p. 155.

(which is defined as the ratio of the entrance opening diameter, d_1, to the exit opening diameter, d_2), the maximum acceptance angle of the CPC can be computed from

$$\frac{1}{\sin\theta_{max}} = \frac{d_1}{d_2}$$

The concentration ratio in three dimensions is given by

$$CR = (d_1/d_2)^2$$

The Cassegrain image size, including any blurring due to imperfect optical surface profiles, must be equal to d_1, the diameter of the entrance aperture of the CPC. The diameter of the exit opening of the CPC must be equal to the diameter of the solar cell array. The ellipse's semi-minor axis, b, and semi-major axis, a, are given by

$$b = d_1/2$$

$$a = \frac{b\left(1 + d_2/d_1\right)}{\left(1 - (d_2/d_1)^2\right)^{\frac{1}{2}} \tan\theta_{max}}$$

Since the vertex is unused, the actual length, L, of the ellipse is slightly less than the semi-major axis. It is given by

$$L = (\tfrac{1}{2})\left(d_1 + d_2\right) \cot\theta_{max} = a\left(1 - (d_2/d_1)^2\right)^{\frac{1}{2}}$$

The curvature of the ellipse is

$$C = \frac{a}{b^2}$$

and the conic constant of the ellipse is

$$k = \left(\frac{b}{a}\right)^2 - 1 = -e^2$$

where e is the eccentricity of the ellipse. The vertex radius and conic constant completely define the surface profile of the CPC.

A general surface equation for any conic section, where the z-axis is taken to be the optical axis, is

$$z = \frac{C\rho^2}{1 + \sqrt{1 - (k+1)\, C^2 \rho^2}}$$

where z is the surface sagitta along the optical axis for a surface point given by $\rho^2 = x^2 + y^2$.

The value of the conic constant determines the type of surface:

$k < -1$	Hyperboloid
$k = -1$	Paraboloid
$-1 < k < 0$	Ellipsoid of revolution about major axis
$k = 0$	Sphere
$k > 0$	Ellipsoid of revolution about minor axis

Thus, the ellipse of the CPC will have a conic constant between zero and minus one.

The axial separation of the CPC exit aperture from the image produced by the Cassegrain is given by the length, L, of the ellipse. This representation thus allows the CPC to be raytraced in three dimensions in a relatively straightforward fashion. In practice, this surface profile must be redefined several times within the raytrace because a number of skew rays will undergo more than one reflection from the CPC walls before reaching the solar cells. This is a simple matter, though, and is easily implemented to insure all entering rays exit the CPC correctly.

For an overall ideal system concentration ratio of 1000, which assumes no optical inefficiencies, the pertinent constructional parameters of the CPC for various Cassegrain f-numbers are given in Table 1. In the next subsection the design concentration ratio is increased to compensate for optical inefficiencies such as obscuration by the secondary mirror.

TABLE 1. CASSEGRAIN AND CPC PARAMETERS BASED ON IDEAL SYSTEM CONCENTRATION OF 1000 SUNS

Cassegrain		CPC					
f/#	Concentration	Concentration Required	Semi-Minor Axis (m)	Semi-Major Axis (m)	Length (m)	Vertex Radius (m)	Conic Constant
1	3303	(0.356)	--	--	--	--	--
2	826	1.425	0.310	0.679	0.371	0.141	-0.792
3	367	3.206	0.464	1.295	1.074	0.166	-0.872
4	206	5.699	0.619	2.096	1.903	0.183	-0.913
5	132	8.905	0.774	3.082	2.904	0.194	-0.937
6	92	12.823	0.928	4.253	4.084	0.203	-0.952
7	67	17.454	1.083	5.609	5.446	0.209	-0.963

2.3.1 Cassegrain Surface Tolerance Analysis

In an ordinary Cassegrain telescope used for optical imaging, the secondary is much more sensitive to surface errors than the primary. However, the actual surface tolerances of both surfaces must be analyzed in a somewhat different manner for non-imaging concentrators. In a solar concentrator, the objective is to collect the energy within a certain sized blur rather than to obtain a well-focused image. To determine the relative sensitivities of the primary and secondary surfaces, two cases are analyzed for slope errors resulting at the primary and secondary, respectively.

First, consider a slope error Δm_1° at the primary mirror and a perfect secondary mirror. This slope error gives rise to an angular error of the reflected ray given by

$$\Delta\theta = 2\Delta m_1^\circ$$

At the secondary, located a distance t_1 from the primary, this angular error causes the ray to intersect the secondary at a ray height which is displaced from the nominal intersection point by a distance Δy, where

$$\Delta y \simeq t_1 \Delta\theta = 2\Delta m_1^\circ \; t_1$$

This displacement in ray height at the secondary results in an additional slope error Δm_2 being seen by the ray, in addition to the original slope error Δm_1°. This slope error is simply the change in slope of the surface

of the secondary due to a change in ray height at the surface. Since the secondary is a hyperbolic conic section, its surface profile is given by:

$$z = \frac{Cy^2}{1 + \sqrt{1 - (k+1)\,C^2y^2}}$$

as described previously. (For simplicity we have assumed $x = 0$.)

The slope of this surface profile is:

$$m_2 = \frac{-dz}{dy} = \frac{-Cy}{\sqrt{1 - (k+1)\,C^2y^2}}$$

Now, the change of slope with respect to a change in ray height y is:

$$\frac{dm_2}{dy} = \frac{-d^2z}{dy^2} = \frac{-C}{\left[1 - (k+1)\,C^2y^2\right]^{3/2}}$$

Thus the slope error, Δm_2, is given by:

$$\Delta m_2 = \frac{-C}{\left[1 - (k+1)\,C^2y^2\right]^{3/2}}\,\Delta y = \frac{-C}{\left[1 - (k+1)\,C^2y^2\right]^{3/2}}\,(2t_1\Delta m_1^{\circ})$$

The final ray error resulting from both the primary and secondary is given by:

$$\theta_A = \Delta\theta - 2\Delta m_2 = 2(\Delta m_1^{\circ} - \Delta m_2)$$

and the resulting image plane ray height error is given by:

$$y_e \simeq (t_1 + t_2)\,\theta_A = 2(t_1 + t_2)\,\Delta m_1^\circ \left[1 + \frac{2Ct_1}{\left[1 - (k+1)\,C^2y^2\right]^{3/2}}\right]$$

In the second case the primary is assumed to be perfect, while the secondary has a slope error Δm_2° associated with its surface profile. Here, the final ray error resulting from this slope error is given by:

$$\theta_B = 2\,\Delta m_2^\circ$$

and the resulting image plane ray height error is given by:

$$y_e \simeq (t_1 + t_2)\,\theta_B = (t_1 + t_2)\,2\,\Delta m_2^\circ$$

To determine the relative sensitivities of the surface profiles of the primary and the secondary, the image plane ray height errors are equated:

$$2(t_1 + t_2)\,\Delta m_1^\circ \left(1 + \frac{2Ct_1}{1 - (k+1)\,C^2y^2}^{3/2}\right) = (t_1 + t_2)\,2\Delta m_2^\circ$$

which reduces to:

$$\Delta m_2^\circ = \left(1 + \frac{2Ct_1}{1 - (k+1)\,C^2y^2}^{3/2}\right)\,\Delta m_1^\circ$$

Thus, the allowable slope error of the secondary is greater than that of the primary, which results in the secondary being a less sensitive surface to fabricate compared to the primary. Since the cost of the surface is inversely

proportional to the allowable slope error of the surface, the cost of the secondary per unit area is less than the cost of the primary per unit area by the factor:

$$\frac{\text{Cost Secondary}}{\text{Unit Area}} = \frac{\text{Cost Primary}}{\text{Unit Area}} \left[\frac{1}{1 + \dfrac{2Ct_1}{\left[1 - (k+1)\, C^2 y^2\right]^{3/2}}} \right]$$

2.4 SYSTEM COMPARISONS

Using the relationships derived for designing the Cassegrain telescope, the CPCs, and the beam splitters, the entire system configuration can be analyzed by the defining parameters. By varying these parameters, several system configurations were generated for comparison. All length dimensions of the system were normalized to the diameter of the primary mirror; all areas were normalized to the square of the primary diameter. Each of these normalized parameters, as well as other parameters requiring no normalization, were then plotted as a function of the f-number of the system for various values of the primary mirror focal length, f_1. The minimum primary f-number considered was f/0.7. This decision was based on the degree of difficulty associated with deploying such "deep-dish" surfaces while maintaining the required surface accuracy. Additionally, the primary area begins to grow significantly with f-numbers below f/0.7. A beam splitter angle of 22 degrees was assumed. The rationale for this assumption is discussed in Section 3. Four-cell systems were not analyzed because their solar-cell/beam-splitter efficiencies were found to be lower than three-cell systems, as discussed in Section 4.

The Cassegrain concentration ratio is given by

$$CR_{Cass} = \left(\frac{1}{2(f/\#)\,\alpha \tan \beta} \right)^2$$

For a particular blur factor of $\alpha = 2$, Figure 6 shows the expected result that as the system f-number increases, thus increasing the size of the image blur, the concentration ratio of the Cassegrain drops in an inverse quadratic fashion. Thus for larger system f-numbers more concentration is required by the CPCs in order to maintain a constant system concentration at the solar cells.

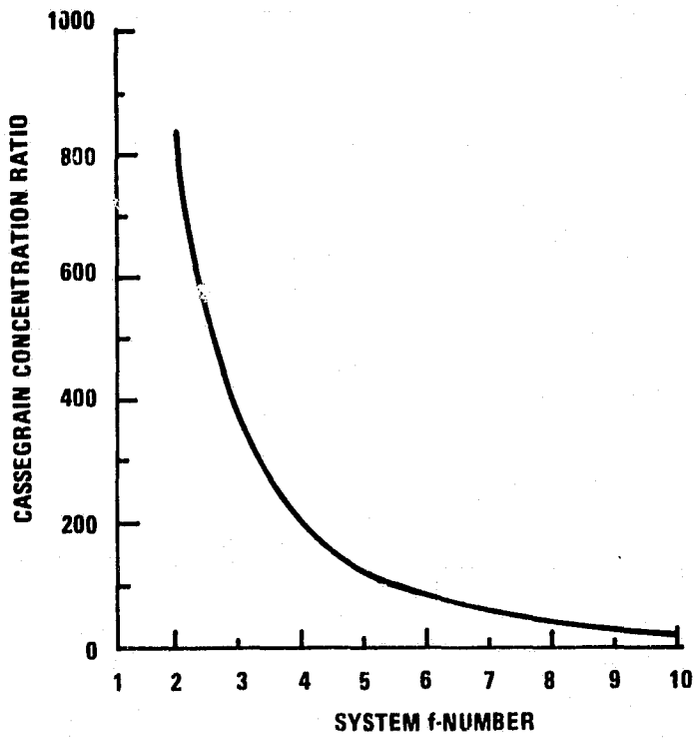

Figure 6. Cassegrain Concentration Ratio Dependence on System f-Number

The distance between the image plane and the primary mirror is

$$t_2 = \begin{cases} 0\text{--one-cell system} \\ (\ell/D_1 + \ell_1/D_1)\,(1 - \cos(2\theta_{bs})) - \ell/D_1\text{--two-cell system} \\ (\ell/D_1 + \ell_2/D_1)\,(1 - \cos(2\theta_{bs})) - \ell/D_1\text{--three-cell system} \end{cases}$$

where ℓ, ℓ_1, and ℓ_2 were defined in subsection 2.1. The distances are plotted in Figure 7 as a function of system f-number. One of the consequences of using large system f-numbers is the correspondingly large distance required between the image and the primary, as can be seen in Figure 4. This is the result of requiring that the CPCs not interfere with either the primary mirror or the converging output from the Cassegrain telescope. For large system f-numbers the convergence angle becomes smaller and requires a larger distance to prevent energy blockage by the CPCs. The distance for three-cell systems is larger because two beam splitters are required. Note that a single-cell system requires no beam splitters and thus the single CPC can be placed at any convenient axial separation, perhaps even ahead of the primary if other trade-offs so necessitate.

The dependence of the beam-splitter areas on system f-number is shown graphically in Figure 8 and pictorially in Figure 4. The large image-to-primary distance and the increase in image blur size with increasing system f-numbers results in an increase in the area of the beam splitters. The difference in the two beam-splitter areas for a three-cell system is simply the result of the last beam splitter being closer to the image plane and hence smaller. The smallest beam-splitter areas are for f-numbers in the range from f/3 to f/4.

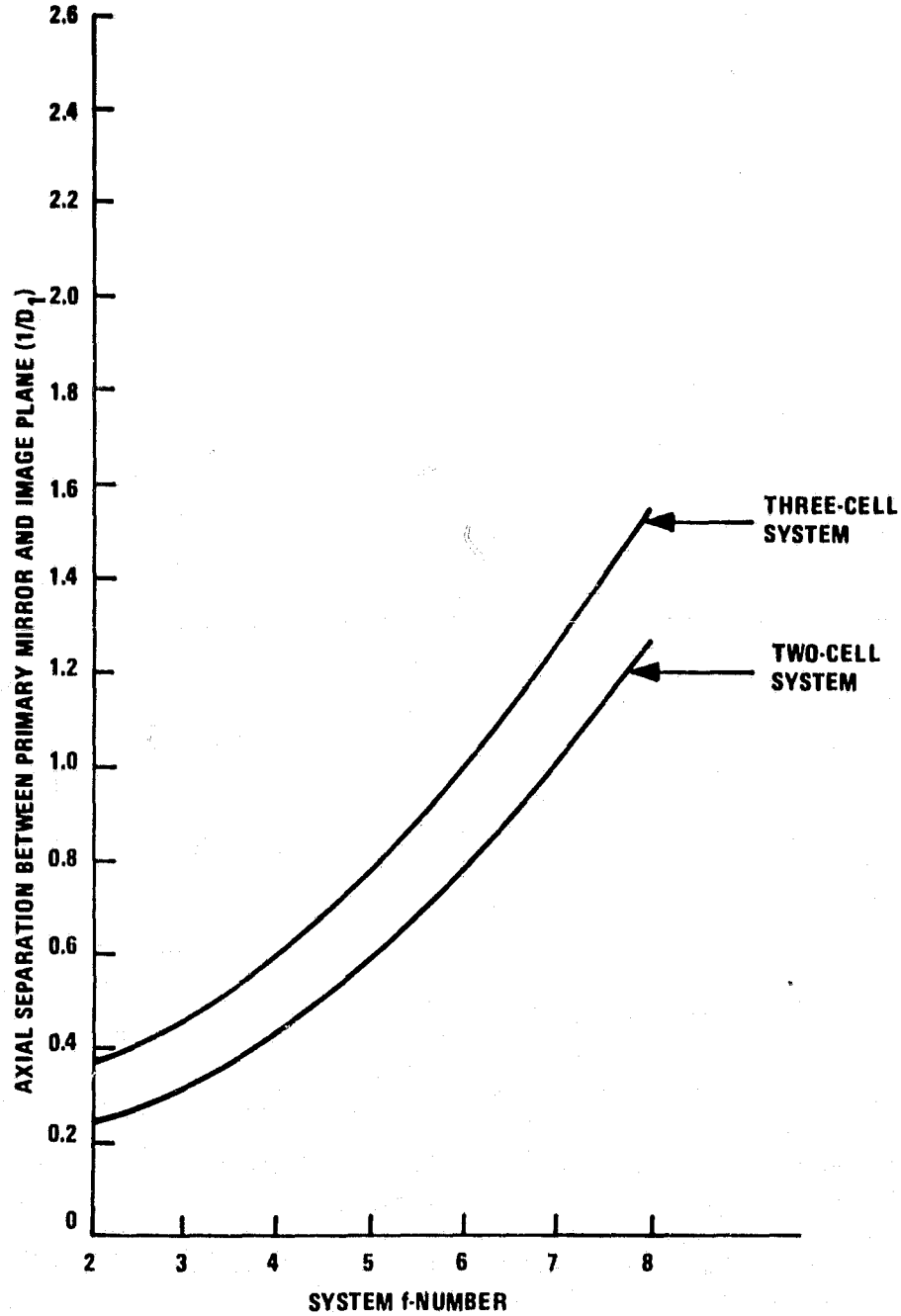

Figure 7. Axial Separation Between the Image Plane and the Primary Mirror as a Function of System f-Number

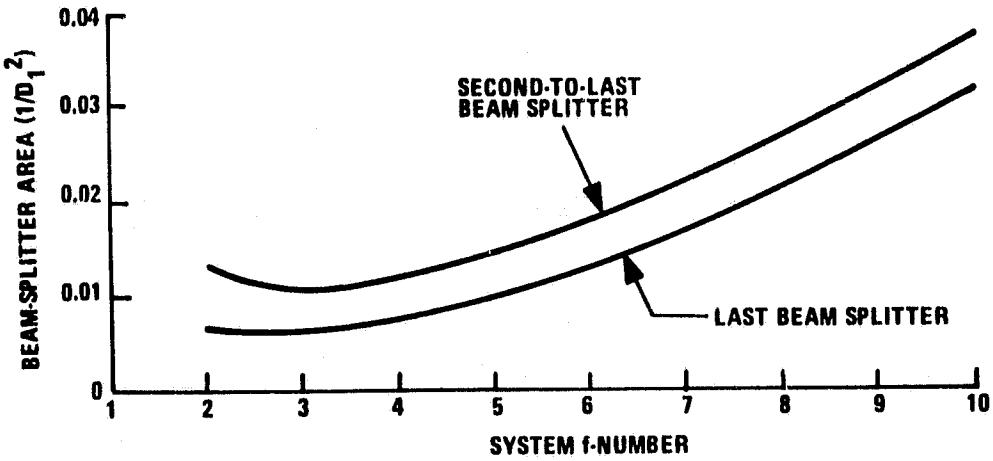

Figure 8. Beam-Splitter Area as a Function of System f-Number

The system length is plotted in Figure 9. For the multi-cell systems the large increase with f-number is due mainly to the large axial separations, t_2, for large f-numbers. The influence of f_1/D_1 is a result of the fact that $L \propto (f_1 + t_2)$. For the one-cell systems $L \approx f_1$ for large f-numbers.

The secondary magnification is proportional to the system f-number and inversely proportional to f_1/D_1. A larger secondary magnification requires a smaller f_1/D_1 ratio for a constant system f-number, resulting in a much stronger curved primary. The ability to accurately fabricate such strong surfaces along with the eventual increase of surface area relative to the primary diameter limits the primary f-number in a practical sense; we have chosen to limit the primary to an f-number no lower than f/0.7. This dependence is shown in Figure 10.

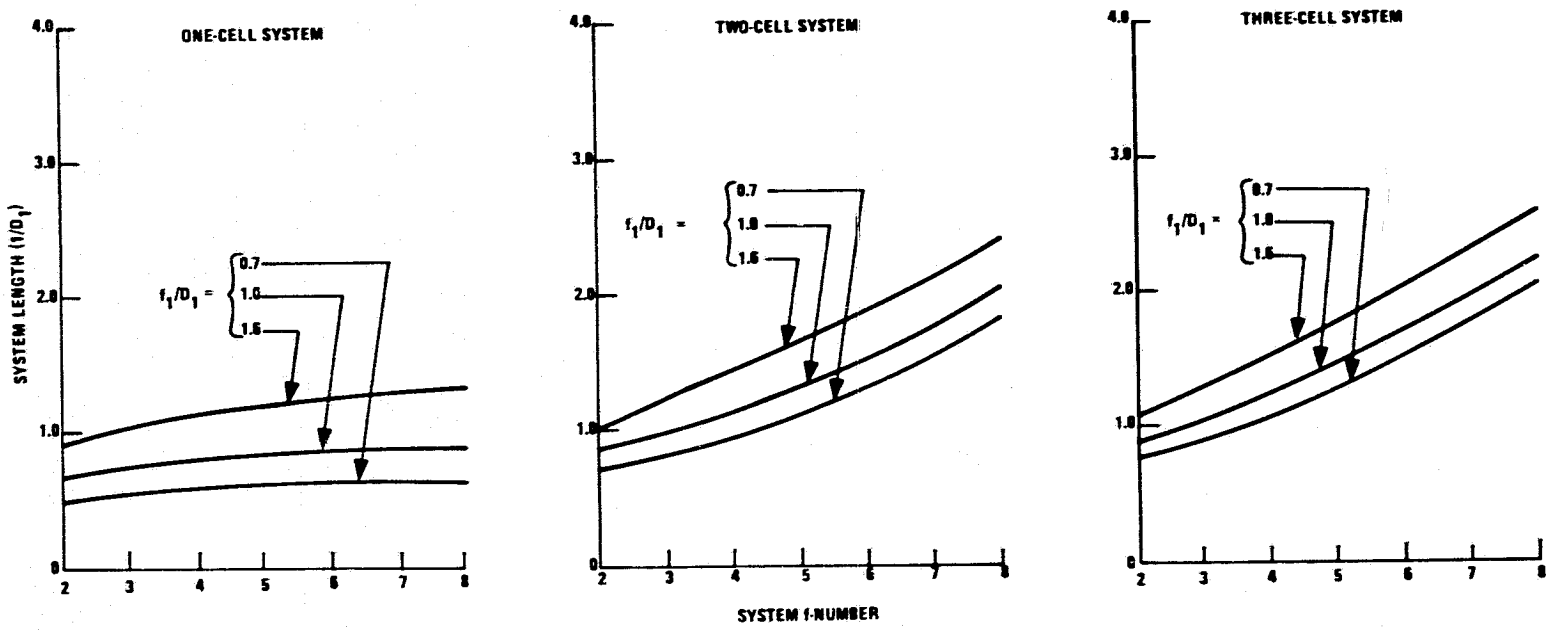

Figure 9. System Length Dependence on f-Number and f_1/D_1

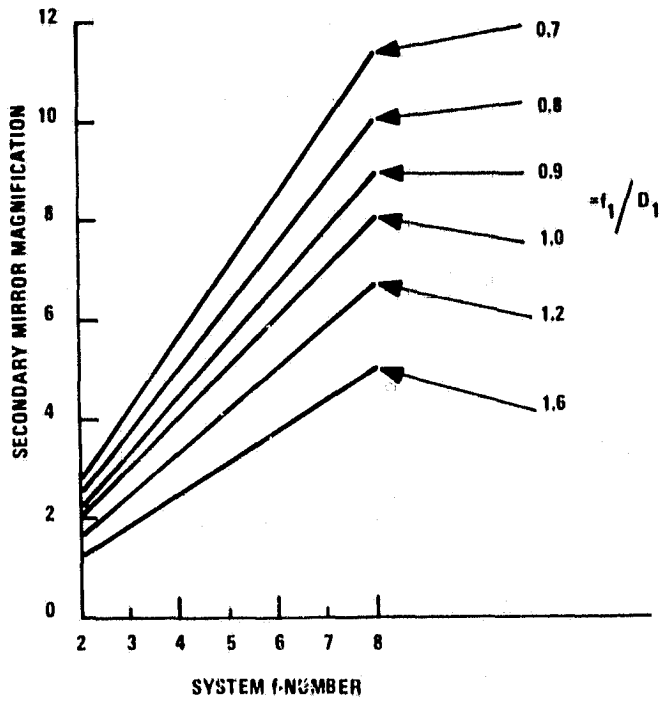

Figure 10. Secondary Mirror Magnification Dependence on System f-Number and f_1/D_1

The dependence of secondary mirror diameter D_2 on system f-number and f_1/D_1 is given by

$$\frac{D_2}{D_1} = \frac{f_1/D_1 + t_2/D_1 + 2\alpha \tan \beta \, (f_1/D_1)\,(f/\# - t_2/D_1)}{f/\# + f_1/D_1}$$

Figure 11 shows the dependence of D_2 on these parameters. Its increase with number of cells reflects its dependence on the axial separation, t_2, required between the primary mirror and the image plane for multi-cell systems. The flattening out of the curves for large f-numbers for the multi-cell systems reflects the dependence of D_2 on (f_1/D_1) / (f/#) for small f-numbers and on (t_2/D_2) / (f/#)

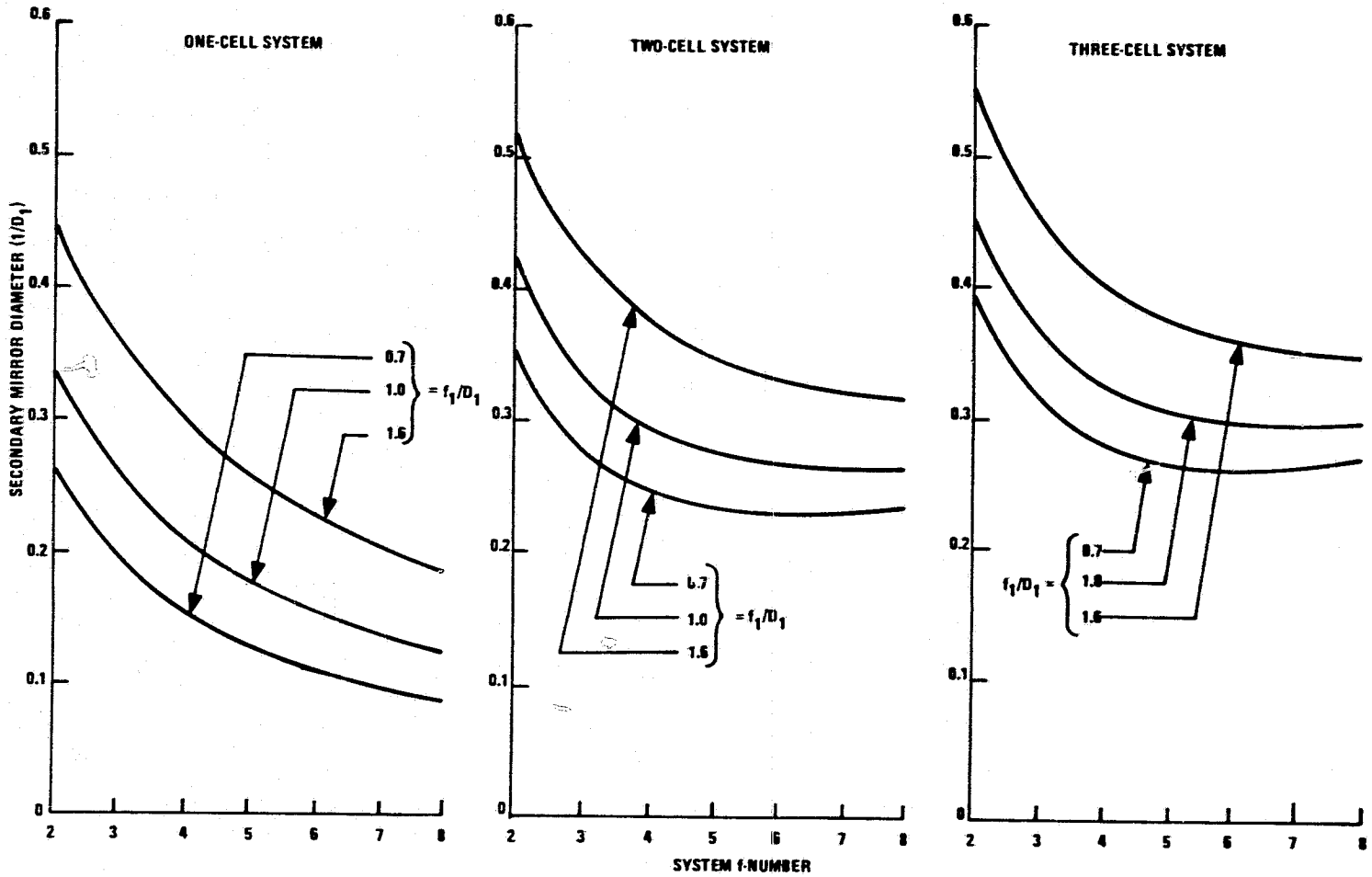

Figure 11. Secondary Mirror Diameter Dependence on System f-Number and Primary Mirror Focal Length f_1/D_1 for Multi-Cell Systems

for large f-numbers. The family of curves within each cell system shows a mild decrease with f_1/D_1. For small values of D_2 the secondary mirror experiences more heating.

The obscuration efficiency $\left(1 - (D_2/D_1)^2\right)$, which is the fraction of collector area unobscured by the secondary mirror, is plotted in Figure 12. For the multi-cell systems, the least obscuration occurs for large f-numbers at the minimum values of D_2. Low values of f_1 produce the highest obscuration efficiency.

In order to maintain a concentration ratio of 1000 on the solar cells, less any losses due to the beam splitters, the CPC concentration ratio is taken to be

$$CR_{CPC} = \frac{1000}{CR_{Cass}\,\epsilon_{Cass}\,\epsilon_{CPC}\,\epsilon_{OBS}}$$

where

ϵ_{Cass} = collector efficiency = 0.90

ϵ_{CPC} = concentrator efficiency = 0.95

The collector efficiency assumes an average spectral reflectivity for the primary and secondary of 0.95, which is within today's technology for producing high-efficiency reflection coatings. The product of the primary and secondary reflectivities gives the collector an efficiency of 0.90 for the Cassegrain. The same surface efficiency of 0.95 applies to the CPC as well. Two advantages the CPC has in this regard are that the average number of reflections per ray entering the CPC is close to one, and the angle of incidence of an average ray on the CPC surface is very high, which increases the effective reflectivity of the surface.

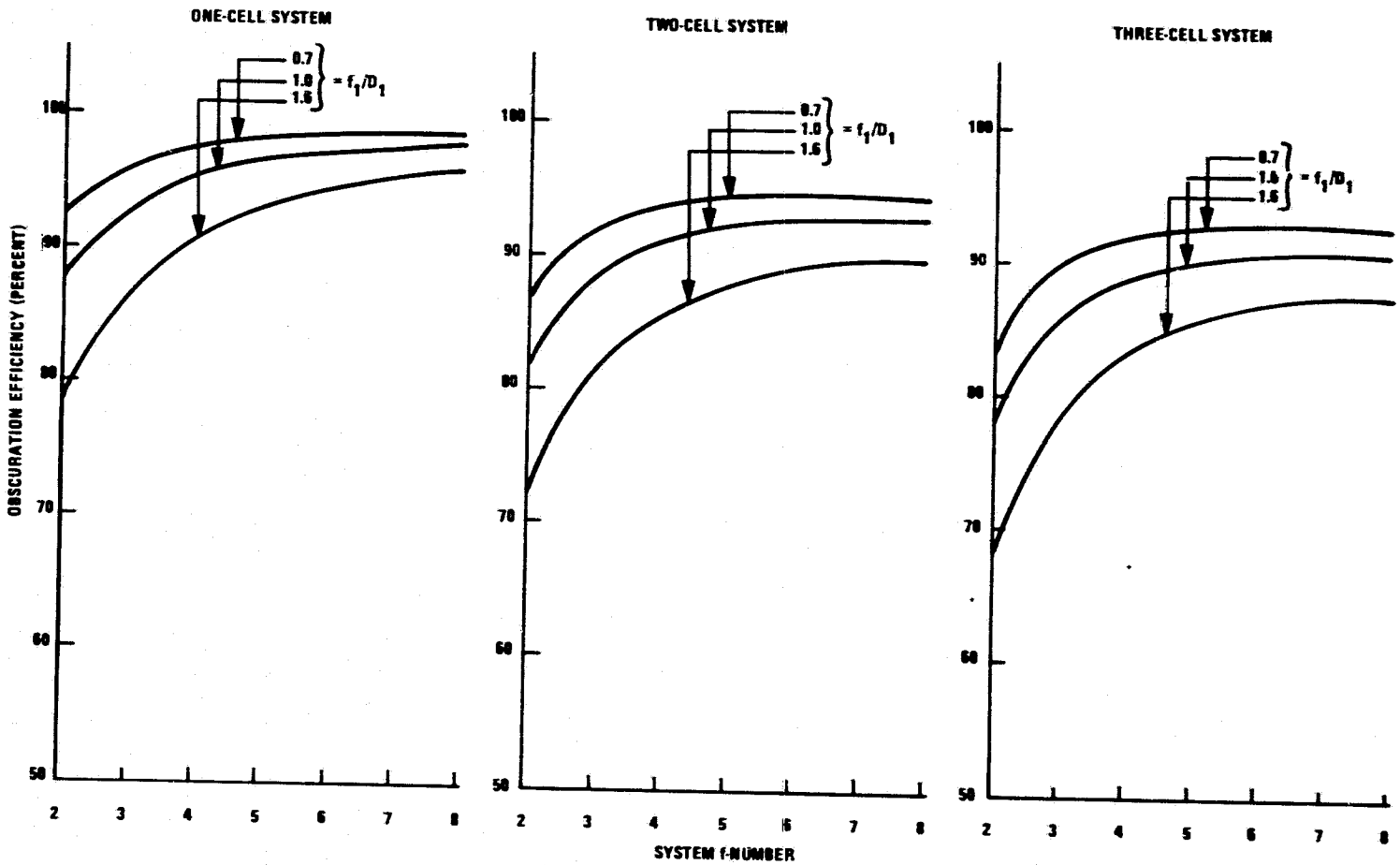

Figure 12. Obscuration Efficiency Dependence on System f-Number and f_1/D_1

Figure 13 illustrates the CPC concentration ratio as a function of system f-number for values of f_1/D_1. Its dramatic increase with f-number is due mainly to the quadratic decrease with f-number of the Cassegrain concentration ratio. The increase of the CPC concentration ratio with f_1/D_1 and with number of cells in the system is due to the increase in D_2/D_1, which decreases the obscuration efficiency.

The solar cell area is equal to the primary mirror area divided by the product of the concentration ratios of the Cassegrain and the CPC. It can also be written as

$$A_{sc} = \pi (D_1/2)^2 \quad \frac{\epsilon_{Cass}\, \epsilon_{CPC}\, \epsilon_{OBS}}{1000}$$

Hence, this area is directly proportional to the obscuration efficiency. Its dependence on system f-number and f_1 is shown in Figure 14.

The area of the CPC, defined in subsection 2.2, is proportional to the solar cell area and also has a complicated dependence on the CPC concentration ratio. It is plotted in Figure 15 as a function of system f-number. Both the area and the concentration ratio of the CPC increase dramatically with system f-number. As described earlier, truncated CPCs could be used to reduce the area requirements but the optimum situation is to use as small a system f-number as possible. The dependence of the CPC area on f_1 and the number of cells is negligible. This is because the solar cell areas are smaller for the larger values of f_1 and larger numbers of cells, and the CPC concentration ratios are larger for the larger values of f_1 and larger numbers of cells.

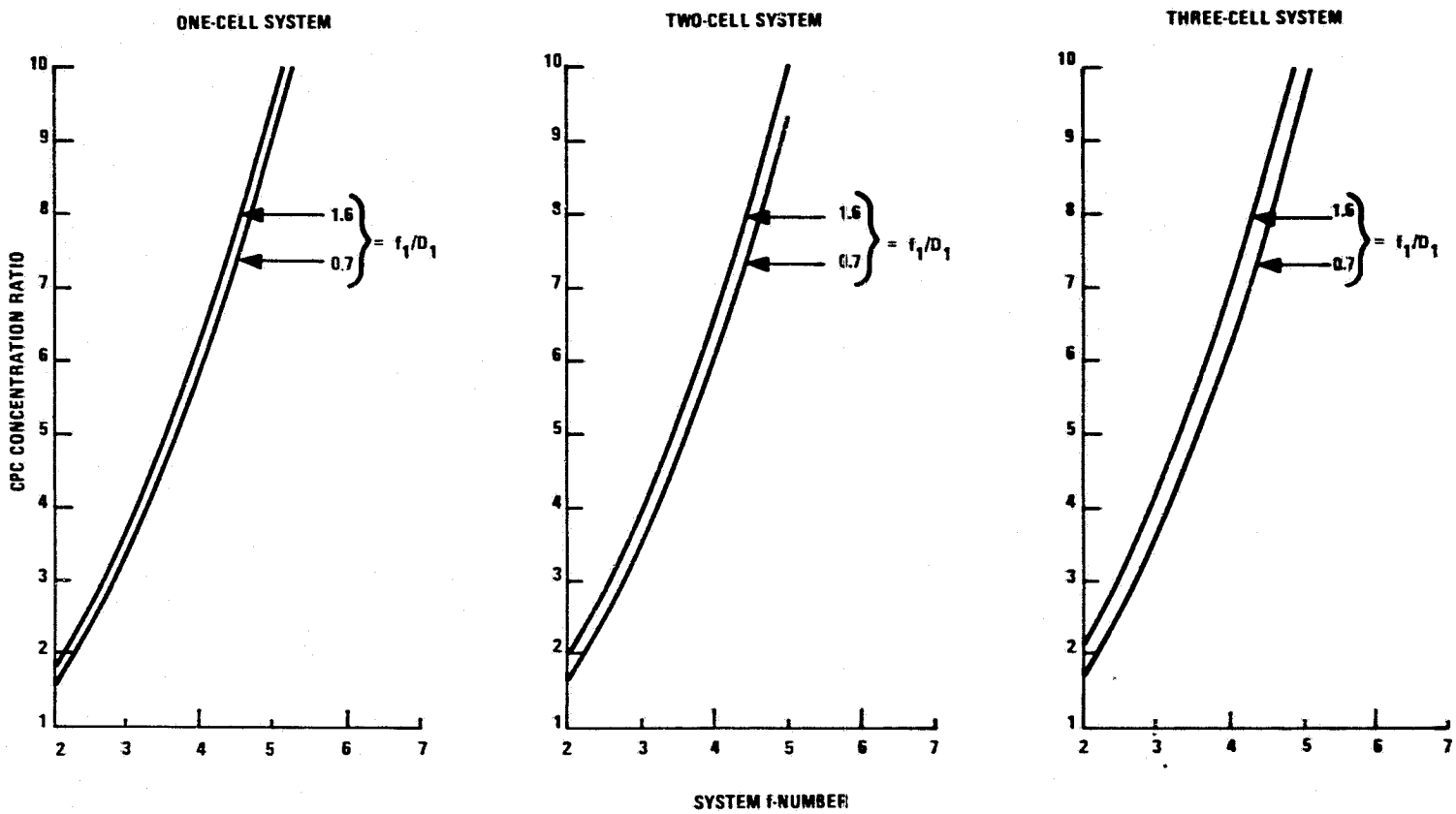

Figure 13. CPC Concentration Ratio Dependence on System f-Number and Primary Mirror Local Length f_1 for Multi-Cell Systems

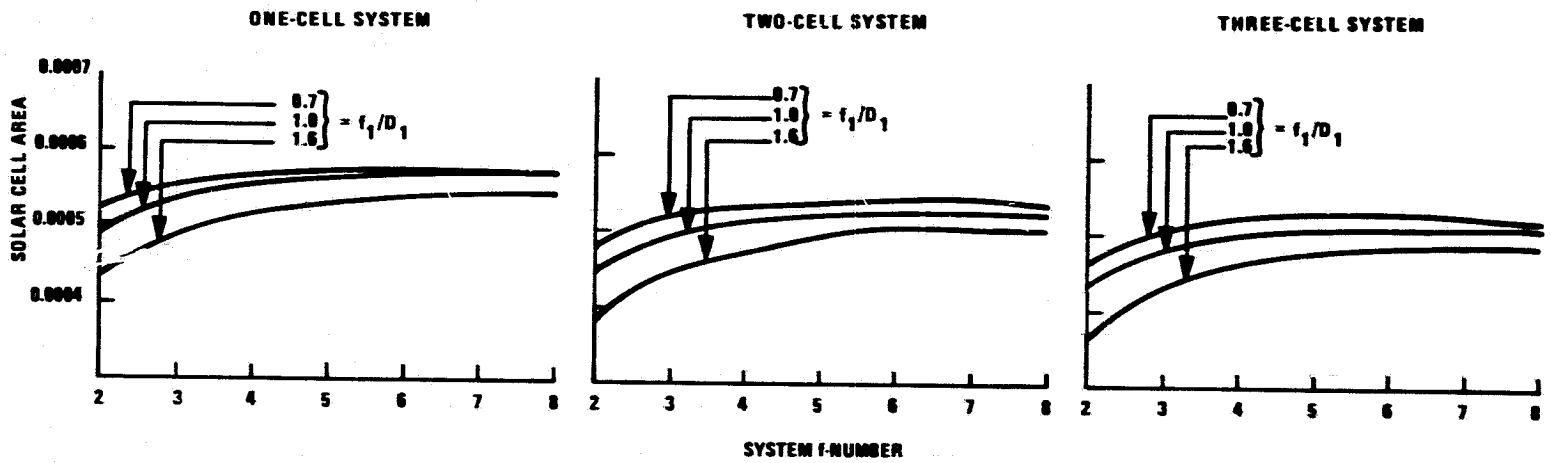

Figure 14. Solar Cell Area Dependence on System f-Number and f_1

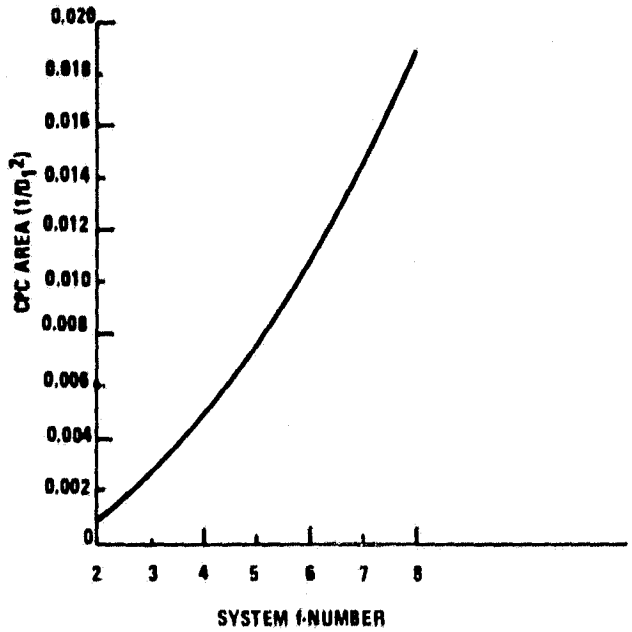

Figure 15. CPC Area Dependence on f-Number

The dependence of the various system parameters on system f-number, primary focal length, and number of cells is summarized in Table 2.

TABLE 2. DEPENDENCE OF SYSTEM PARAMETERS ON SYSTEM f-NUMBER, f_1/D_1, AND NUMBER OF CELLS

System Parameter	Increasing System f-Number	Increasing f_1/D_1	Increasing Number of Cells
Cassegrain concentration ratio	Decreases dramatically	--	--
Axial separation between primary and image plane	Increases dramatically	--	Increases mildly
Beam-splitter area	Increases on both sides of minimum at f/3	--	Higher for second beam splitter for three-cell systems
System length	Increases (more for multi-cell systems)	Increases	Increases
Secondary mirror magnification	Increases	Decreases	--
Secondary mirror diameter	Decreases	Increases	Increases
Obscuration efficiency	Increases and then flattens out	Decreases	Decreases
CPC concentration ratio	Increases dramatically	Increases mildly	Increases mildly
Solar cell area	Increases and then flattens out	Decreases	Decreases
CPC area	Increases dramatically	Increases very slightly	Increases very slightly

SECTION 3

DICHROIC MIRROR BEAM SPLITTERS

The dichroic mirror beam splitters are designed to separate incident solar radiation into matching spectral bands, which are to be collected by solar cells of selected materials.

The basic requirements of a beam splitter to be used in a high-concentration solar cell system include a transparent substrate, beam-splitting coatings applied to the front side of the substrate, and wide-band antireflection (AR) coatings applied to the back side of the substrate. Fused silica is a good candidate material for the substrate because of its transmitting properties and its high thermal stability.

The beam-splitter coatings consist of multilayer stacks of transparent dielectric materials. By depositing alternating high- and low-refractive-index layers onto silica substrates, very high reflectivities can be achieved over a well-defined spectral region. The spectral width of the reflection band is determined by the ratio of refractive indexes used in the stack.

A beam-splitter system was designed for a three-cell GaP/Si/GaAs configuration. The first beam splitter reflects 0.3- to 0.5-μm radiation to the GaP solar cell while transmitting the longer wavelengths. The second beam splitter reflects 0.9- to 1.1-μm radiation to the Si solar cell

and transmits both the shorter wavelengths from 0.5 to 0.9 μm and the longer wavelengths beyond 1.1 μm. This transmitted radiation falls on the GaAs solar cell.

Possible coating materials for the dichroic beam splitters were considered. The beam splitter that must reflect the short-wavelength photons and transmit the rest is the most critical because of its greater environmental exposure and the limited selection of acceptable materials that have a high index of refraction and are transparent to the high ultraviolet (UV). The coating materials must be transparent down to at least 0.3 μm. A literature search was made for materials with transmission cut-offs below 0.35 μm. There are very few high-index materials with this property.

The first beam-splitter coating system designed was a 43-layer double stack of ThO_2/MgF_2. A 22-deg incident angle was required to keep the reflection-band edge sharp. With this cell in the front, only the first beam splitter must be resistant to UV radiation. The second beam-splitter coating was a 24-layer stack of MgF_2/TiO_2. An alternative to this second beam-splitter design was also studied. It consisted of a 24-layer stack of SiO_2/ThO_2. Although the stack reflection band was slightly narrower, the durability of SiO_2/ThO_2 is not as well-proven as that of the TiO_2/MgF_2 combination.

3.1 DESIGN CONCEPT

In order to demonstrate the feasibility of using dichroic mirrors to split the incident solar radiation into spectral bands, a candidate system consisting of GaP, GaAs, and Si cells was chosen for design. The concept is illustrated in Figure 16.

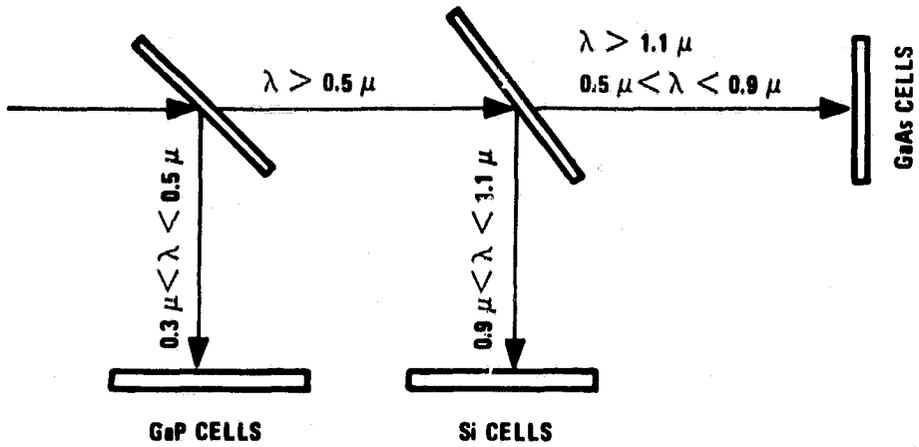

Figure 16. Spectrum-Splitting Concept for Three-Cell Configuration

The first beam splitter reflects the short-wavelength components (from 0.3 to 0.5 μm) to the GaP cells while transmitting the longer wavelengths. The second beam splitter reflects the waveband from 0.9 to 1.1 μm to the Si cells and transmits both the shorter wavelengths from 0.5 to 0.9 μm and the longer wavelengths beyond 1.1 μm to the GaAs cells.

This concept was selected for the following reasons:

1. It is easier to obtain nearly 100% reflectivity over the desired reflection band than it is to obtain zero reflectivity over a desired passband. If a beam splitter is designed to reflect long wavelengths, then the shorter wavelength reflection in the passband can still be used to produce photocurrent by

the low-bandgap (or long-wavelength) cut-off cell. With the alternate design, this reflected light in the passband is wasted. The second beam splitter was designed to reflect long wavelengths (0.9 to 1.1 μm) to make more efficient use of the leaked shorter-wavelength reflection in the passband with the Si cell.

2. By designing the first beam splitter to reflect the shortest wavelengths (0.3 to 0.5 μm), only this mirror is subjected to the severe UV radiation. A requirement for low UV absorption severely limits the selection of coating materials to only the highly UV-transparent materials, which are scarce--especially for high-index materials.

3. The long-wavelength radiation beyond 1.1 μm, which may produce heating, is incident on the more thermally stable GaAs cell.

3.2 SELECTION OF COATING MATERIALS

The first beam-splitter coating, which reflects the short-wavelength region, is more critical than the second beam-splitter coating. This is because of its greater environmental exposure and the limited selection of acceptable coating material candidates for the UV spectral region. Among the requirements for the first beam-splitter coating materials, high UV transparency and good UV and thermal stability are most important.

Most common optical coating materials begin to absorb strongly in the 0.3- to 0.5-μm region. With the concentration ratio proposed for this program, even a one-percent absorption can cause a significant temperature increase in the beam splitter. Because of this, UV transparency is used as the primary criterion for the selection of the first beam-splitter coating materials. In addition, the transmission range and the ratio of high/low refractive indexes are important in selecting the combination of materials for a specific beam splitter.

Numerous low-index, UV-transparent materials are available but high-index candidates are limited. A literature search was made for materials with transmission cut-offs below ~ 0.35 μm (350 nm); the results are shown in Figure 17. Each material is opaque at wavelengths below the value shown. The key properties of some candidate coating materials are listed in Table 3. For the beam-splitter application the transparency should extend to at least 0.3 μm. The lack of high-index candidates is apparent in Figure 17. The least UV-absorbing, high-index materials are ThO_2 and T_2O_3. The most UV-stable coating combinations are Al_2O_3/NaF and ThO_2/SiO_2 but the Al_2O_3/NaF coating may not meet the reflection bandwidth requirement and other environmental durability requirements.

The combination ThO_2 / MgF_2 was selected for the first beam splitter. Among the low-index materials, BaF_2 was rejected because of its poor humidity resistance. In addition, CaF_2 was a possible candidate although it has a slightly higher refractive index than MgF_2. However, it was rejected because it has not been as widely used as MgF_2 for a thin film coating material.

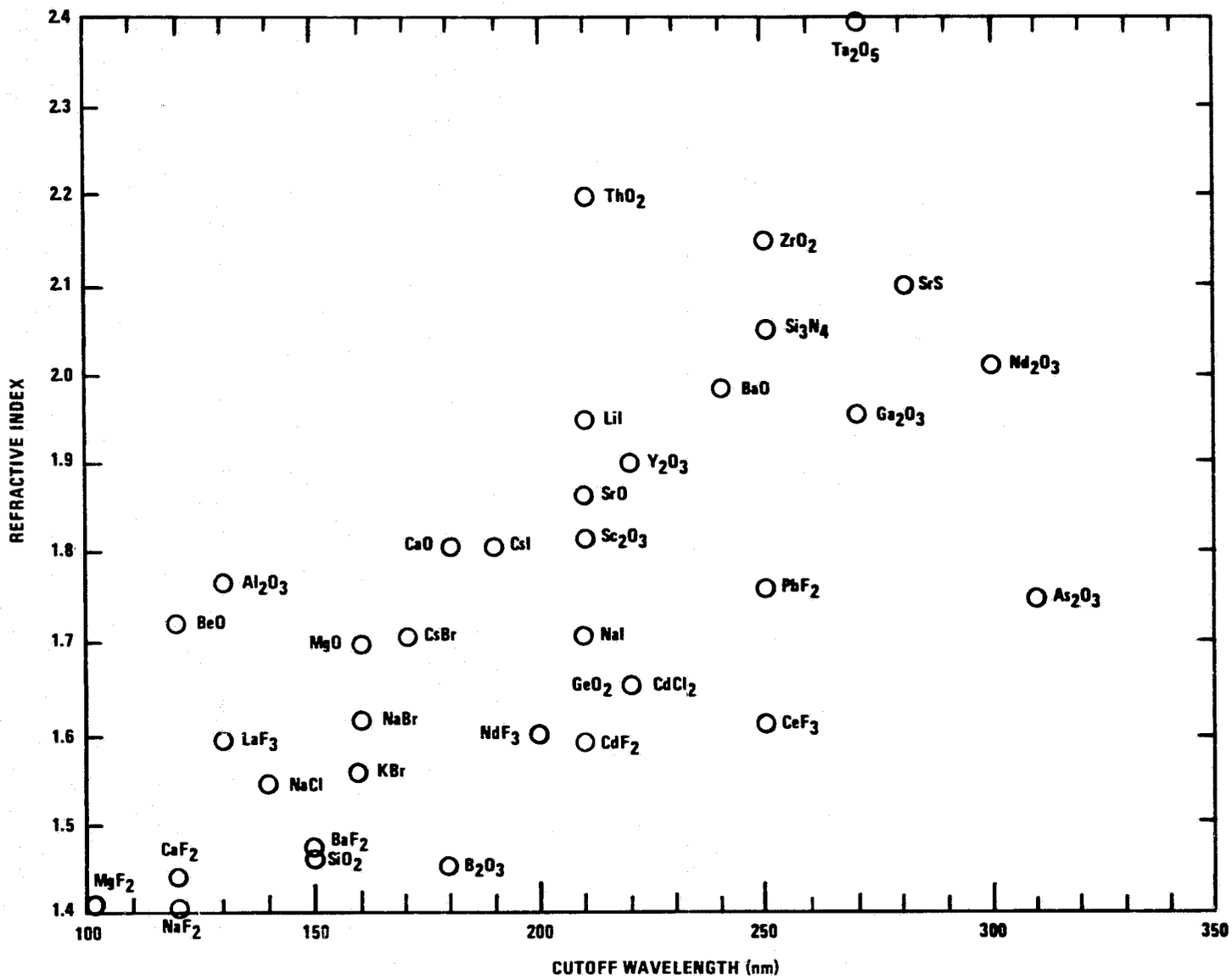

Figure 17. Refractive Index vs Transmission Cut-Off Wavelength for Several UV-Transparent Materials

TABLE 3. KEY PROPERTIES OF CANDIDATE COATING MATERIALS

	MATERIAL	TRANSMISSION RANGE (μm)	REFRACTIVE INDEX		STRESS ** (Kg/cm^2)	THERMAL EXPANSION COEFFICIENT (10^{-6}/°C)	MELTING POINT (°C)	SOLUBILITY * IN WATER (g/100 mℓ)	
			λ (μm)	n				COLD	HOT
HIGH REFRACTIVE INDEXES	ThO_2	0.21–(>5.0)	<1	2.20	950 (T)	9.5	3050	i	i
	Y_2O_3	0.22–(>5.0)	0.4 1.0	1.92 1.83	TBD	6.7 (20°C)	2410	0.00018	–
	Ta_2O_5	0.27–(>5.0)	< 1	2.42	TBD	–	1800	i	i
	ZrO_2	0.3 –7.0	0.55	2.1	TBD	7.5 (80–800°F)	2700	i	i
	TiO_2	0.43–6.0	0.6 0.8	2.29 2.21	200(T), 1000(C)	9.2 (40°C)	1830	i	i
	ZnSe	0.5 –2.0	0.6328 1.1	2.60 2.45	1200 (C)	7.7	>1100	i	–
	ZnS	0.35–14.5	0.578 1.529	2.38 2.28	2000 (C)	6.3 (0°C)	1020	0.000065	–
LOW REFRACTIVE INDEXES	MgF_2	0.11–7.5	0.40 1.00	1.38 1.38	2000 (T)	11.0	1266	0.0076	i
	BaF_2	0.25–15	0.546 1.129	1.48 1.47	1200 (T)	18.4	1280	0.1225	sl.s
	SiO_2	0.35–4.5	0.6328 1.13	1.42 1.45	2900 (C)	0.5	1610	i	i
	CaF_2	0.13–12	0.5 1.0	1.44 1.43	100 (T)	22.0	1360	0.0016	0.0017

* i — insoluble
sl.s — slightly soluble

** T — tensile stress
C — compressive stress

In addition to those high-index materials shown in Figure 17, TiO_2, ZnSe, and ZnS are also good high-index candidates for the second beam splitter. These three materials have transmission cut-offs at 0.35 to 0.5 μm; they also have higher refractive indexes, which are needed for the second beam splitter because of its wider reflection bandwidth.

TiO_2/MgF_2 and SiO_2/ThO_2 combinations were selected as design candidates for the second beam splitter. The TiO_2/MgF_2 combination was chosen primarily because these materials have been widely used and their durability is well-proven. The reflection bandwidth of the TiO_2/MgF_2 coating is greater than the 0.9- to 1.1-μm range but the selection for the second beam splitter is restricted by the materials available having the appropriate ratio of refractive indexes. However, since the wavelengths longer than 1.1 μm are not to be used in the GaP/Si/GaAs cell system, a bandwidth wider than 0.9 to 1.1 μm is still acceptable. The ThO_2/SiO_2 coating has a slightly narrower reflection band than the TiO_2/MgF_2 coating although it is still wider than 0.9 to 1.1 μm. TiO_2 was not chosen for use with SiO_2 because SiO_2 is very compressive and needs the more tensile ThO_2 to balance the stress.

Other requirements for the coating materials are also important and must be considered. These include thermal shock stability; humidity, weather and pollution resistance; adhesion; and low stress. Some of this information can be found in the literature but most of it can be obtained only from tests in actual or simulated environments.

3.3 BEAM SPLITTER DESIGN AND PERFORMANCE PREDICTIONS

In order to determine the optimum reflection bandwidths for the beam splitters, the relative power spectral response was determined for three solar cell materials: Si, GaP, and GaAs. This power spectral response is a normalized product of solar-cell quantum efficiency and the photocurrent-to-power conversion factor and hence is a measure of photon-to-power conversion efficiency. The results are shown in Figure 18 (the units are arbitrary). The beam-splitter reflection band cut-offs were determined by the intersection of the power spectral response curves for two different solar-cell materials. The GaP solar cell is more efficient than the other two cells for wavelengths less than 0.5 μm. GaAs is more efficient than Si for wavelengths less than 0.9 μm. A reflection band of 0.3 to 0.5 μm was selected for the first beam splitter and a band of 0.9 to 1.1 μm was selected for the second beam splitter.

The first beam-splitter coating was a combination of ThO_2 (n_H = 2.20) and MgF_2(n_L = 1.38) on a quartz substrate (n = 1.46 at 0.5 μm). One single stack of ThO_2/MgF_2 coatings did not have a sufficiently wide reflection band to cover the 0.3- to 0.5-μm range. A broad reflection band was achieved by a double stack of ThO_2/MgF_2 coatings on a single quartz substrate. Each single stack has a similar long-wavelength-pass coating design consisting of quarter-wave alternating layers of high- and low-index films with one-eighth-wave high-index (ThO_2) outermost layers as AR layers. The two single stacks were put together with a quarter-wave low-index (MgF_2) separation layer between to avoid a dip in the compounded reflection band that would otherwise occur. The details of the design are shown in Figure 19.

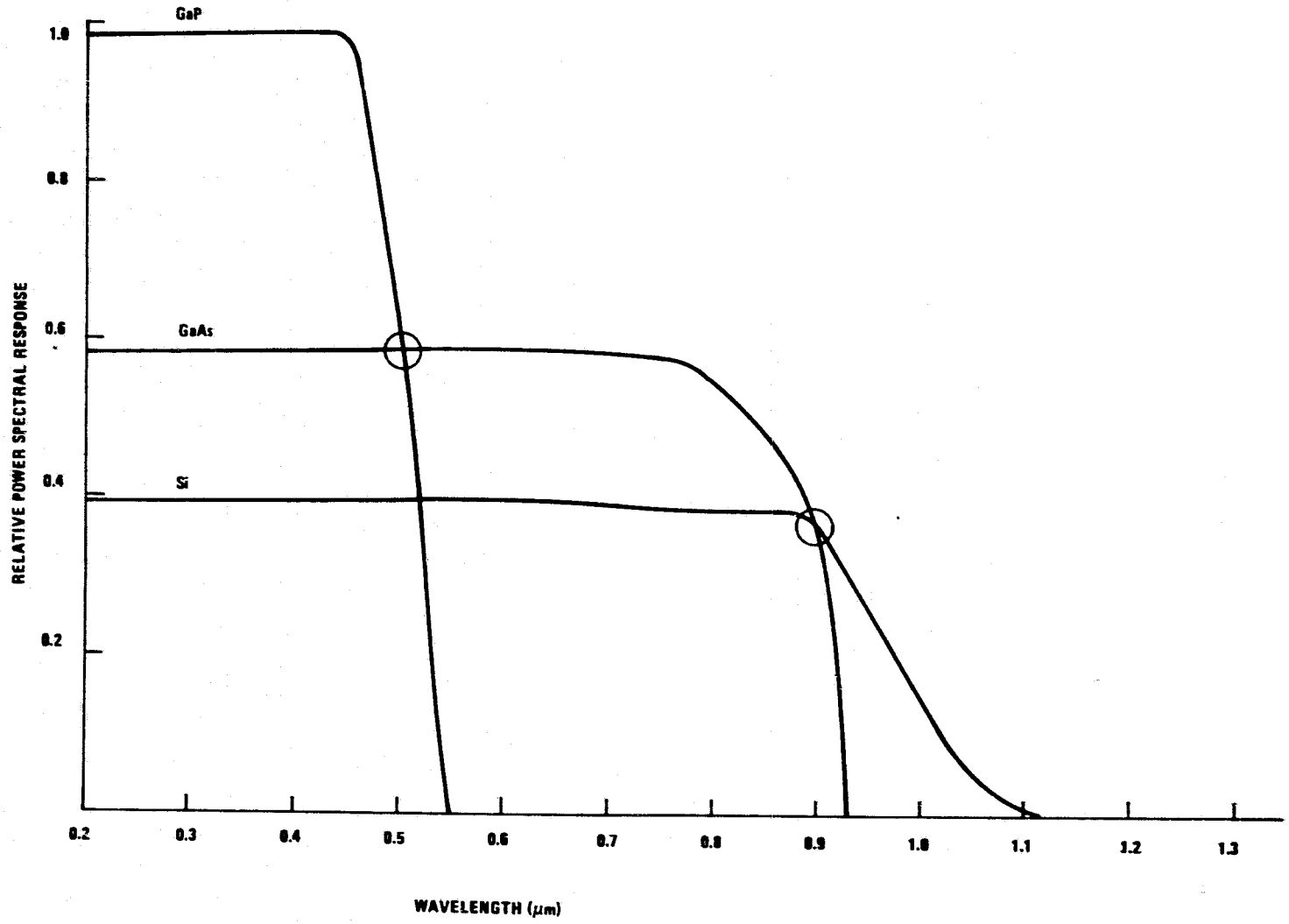

Figure 18. Relative Power Spectral Response of GaP, GaAs, and Si Solar Cells

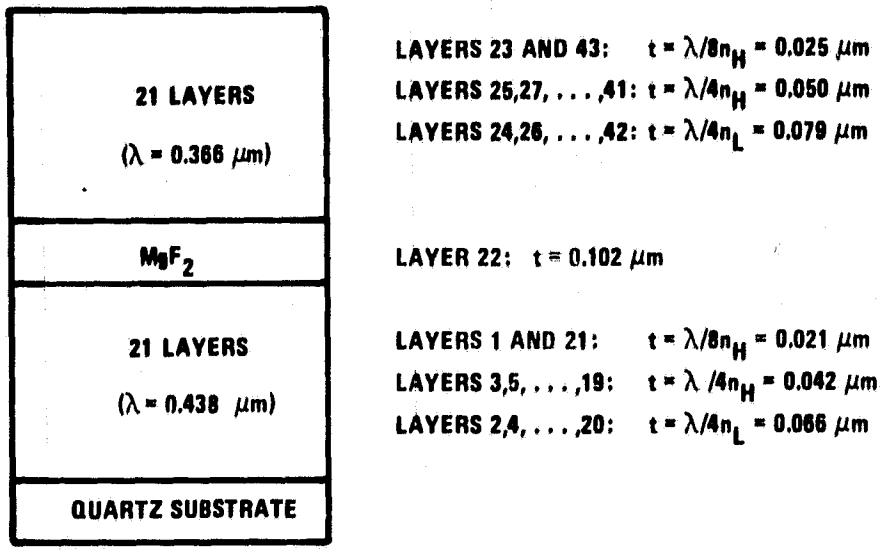

Figure 19. Details of the 43-Layer ThO_2/MgF_2 Beam-Splitter Coating Design (t = physical thickness)

The spectral reflectance of the 43-layer double stack at incident angles of 0 deg, 22 deg, and 45 deg are shown in Figures 20, 21, and 22, respectively. The reflection band edges at a 22-deg incident angle are still sharp but at 45 deg they are not sharp enough. For this reason the tilt angle of the beam splitters relative to the optical axis is chosen to be 22 deg rather than 45 deg. The off-band reflection from 0.5 to 0.8 μm is less than five percent and that from 0.8 to 1.1 μm is about six to seven percent. Further reduction of the off-band reflection ripples is necessary.

The second beam-splitter coating was a combination of TiO_2 (n_H = 2.21) and MgF_2 (n_L = 1.38) on a quartz substrate (n = 1.451 at 1.0 μm). For this beam splitter a short-wavelength-pass design is needed. The basic short-

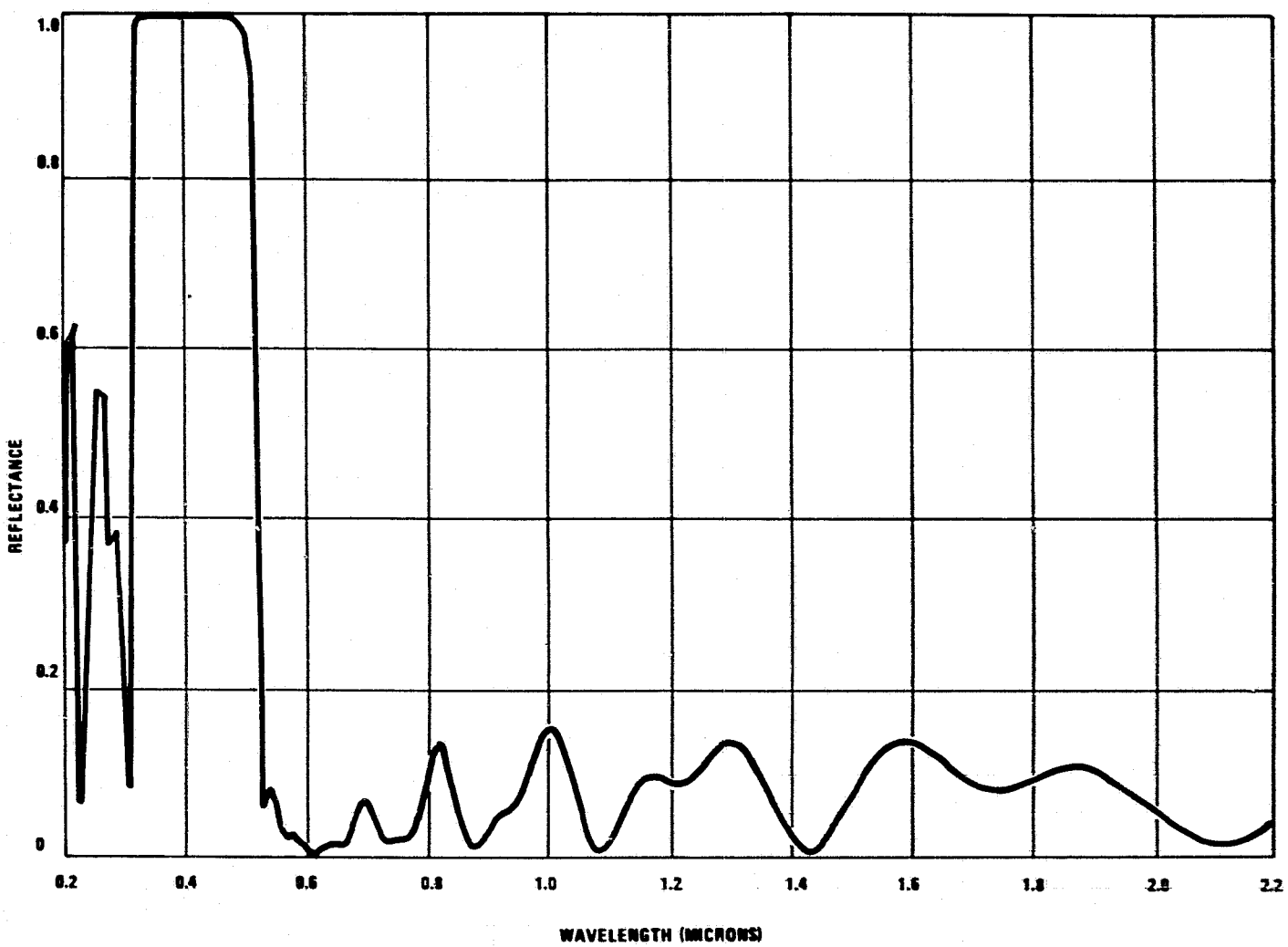

Figure 20. Computed Spectral Reflectance of a 0.3 to 0.5 μm Reflective ThO_2/MgF_2 Beam Splitter (43-layer double stack, $\theta = 0$ deg)

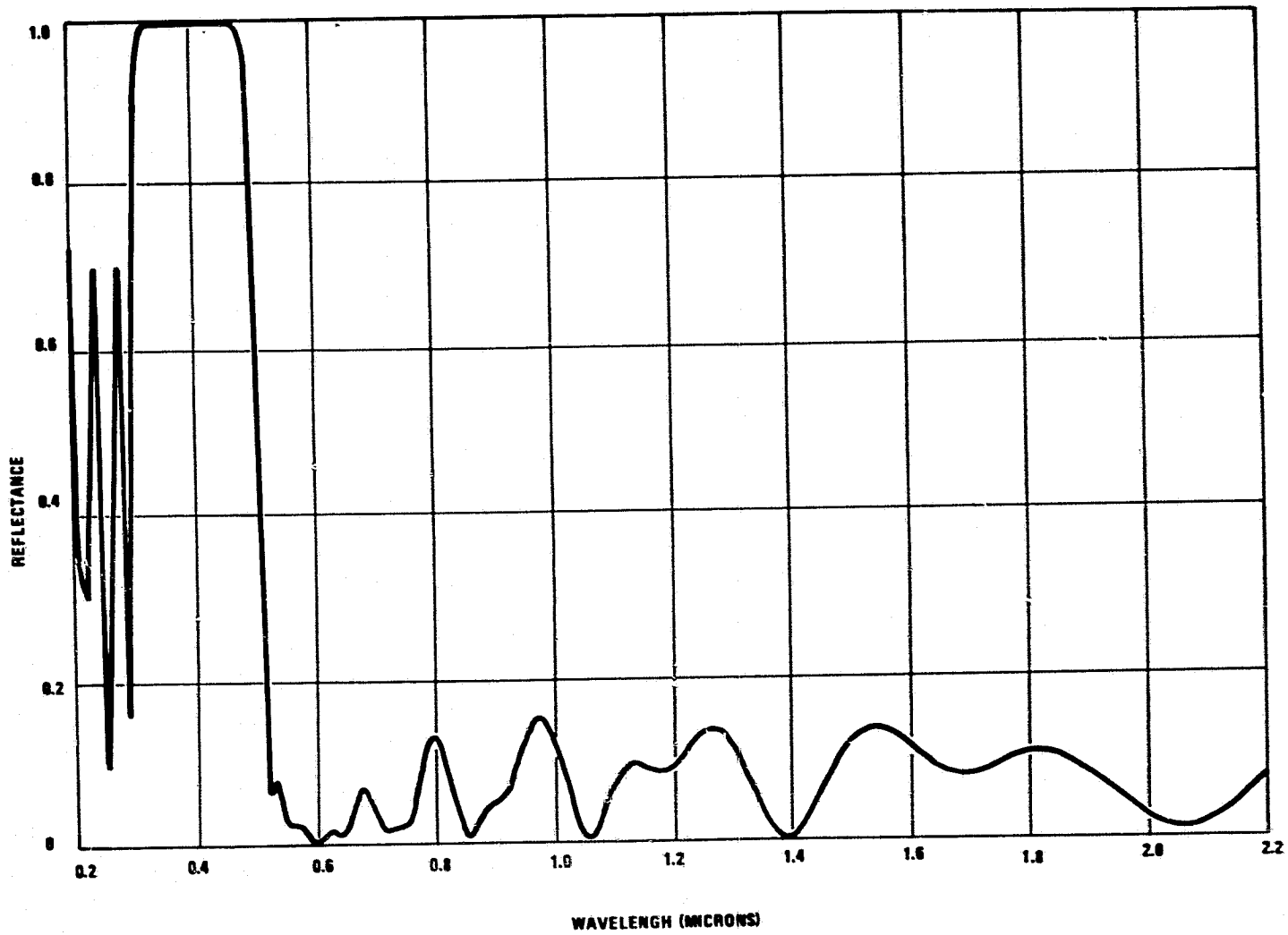

Figure 21. Computed Spectral Reflectance of a 0.3 to 0.5 μm Reflective ThO_2/MgF_2 Beam Splitter (43-layer double stack, θ = 22 deg)

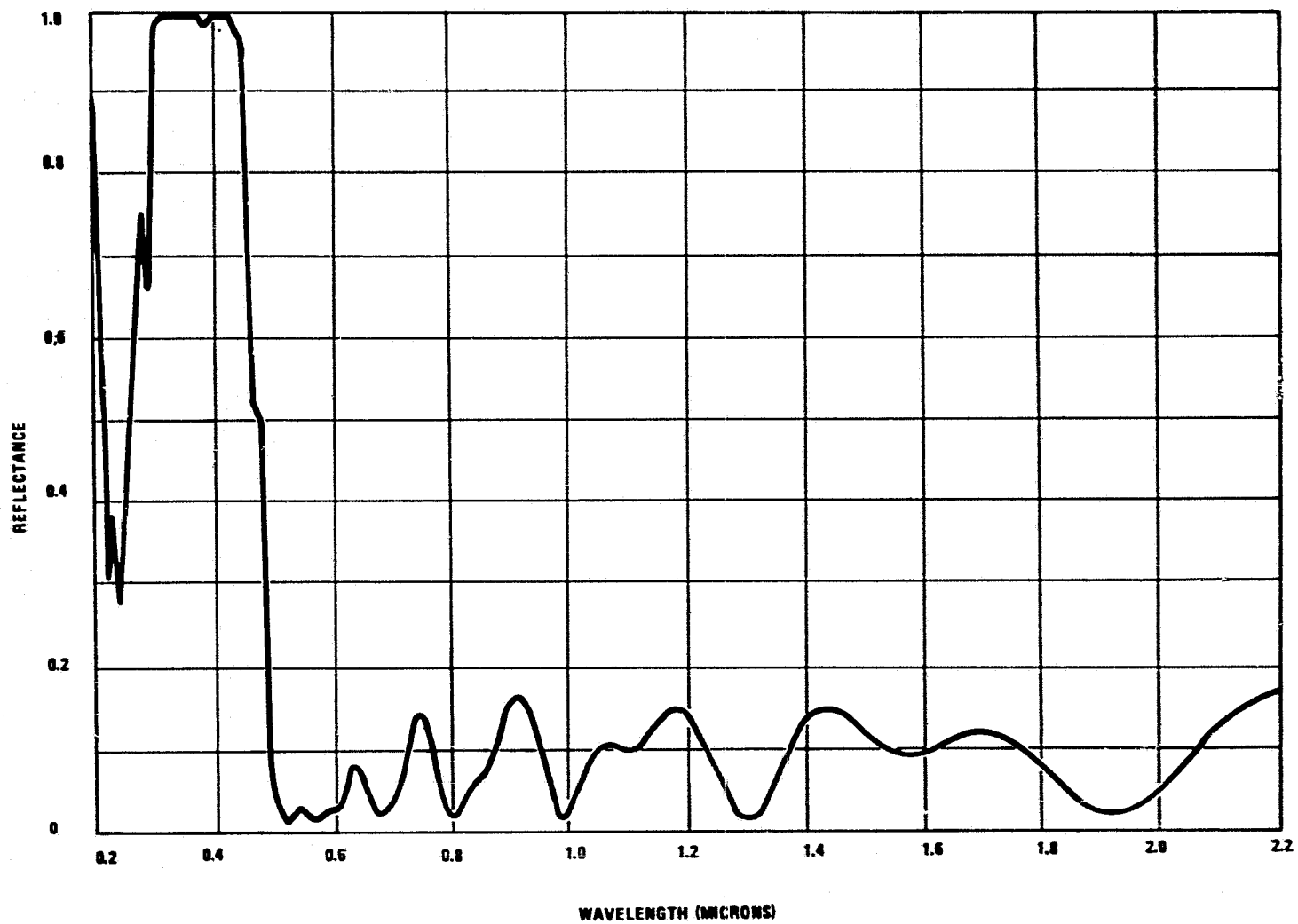

Figure 22. Computed Spectral Reflectance of a 0.3 to 0.5 μm Reflective ThO_2/MgF_2 Beam Splitter (43-layer double stack, θ = 45 deg)

wavelength-pass design requires the odd-number layers and the outermost layers to be the low-index films. The off-band short-wave reflection ripples can be reduced by changing the quarter-wave outermost layers into one-eighth-wave layers. The spectral reflectance of a 21-layer MgF_2/TiO_2 coating system is shown in Figure 23. The details of the design are shown in Figure 24.

The off-band short-wave ripples can be further reduced by introducing an AR layer or layers between the coating stack and the substrate and on top of the stack. A three-layer AR coating consisting of $MgF_2/TiO_2/MgF_2$ was added between the stack and the quartz substrate. The details of the design are shown in Figure 25. Figure 26 shows the spectral reflectance of a 24-layer MgF_2/TiO_2 coating design at a 0-deg incident angle. It has a further reduced off-band short-wavelength reflection. The optimal reflection cut-off at 0.9 μm is designed for the 22-deg incident angle. The spectral reflectances of the 24-layer MgF_2/TiO_2 coating system at 22- and 45-deg incident angles are shown in Figures 27 and 28. Again, the reflection band at a 45-deg incident angle does not have well-defined cut-off edges.

The other coating, designed for the second beam splitter, was a combination of SiO_2 (n_L = 1.45) and ThO_2(n_H = 2.20) on a quartz substrate. The details of the design are shown in Figure 29. The spectral reflectance of a 24-layer SiO_2/ThO_2 coating system at a 22-deg incident angle is shown in Figure 30. This design has a slightly narrower reflection band but the material durability is not as well-proven as that of the TiO_2/MgF_2 combination.

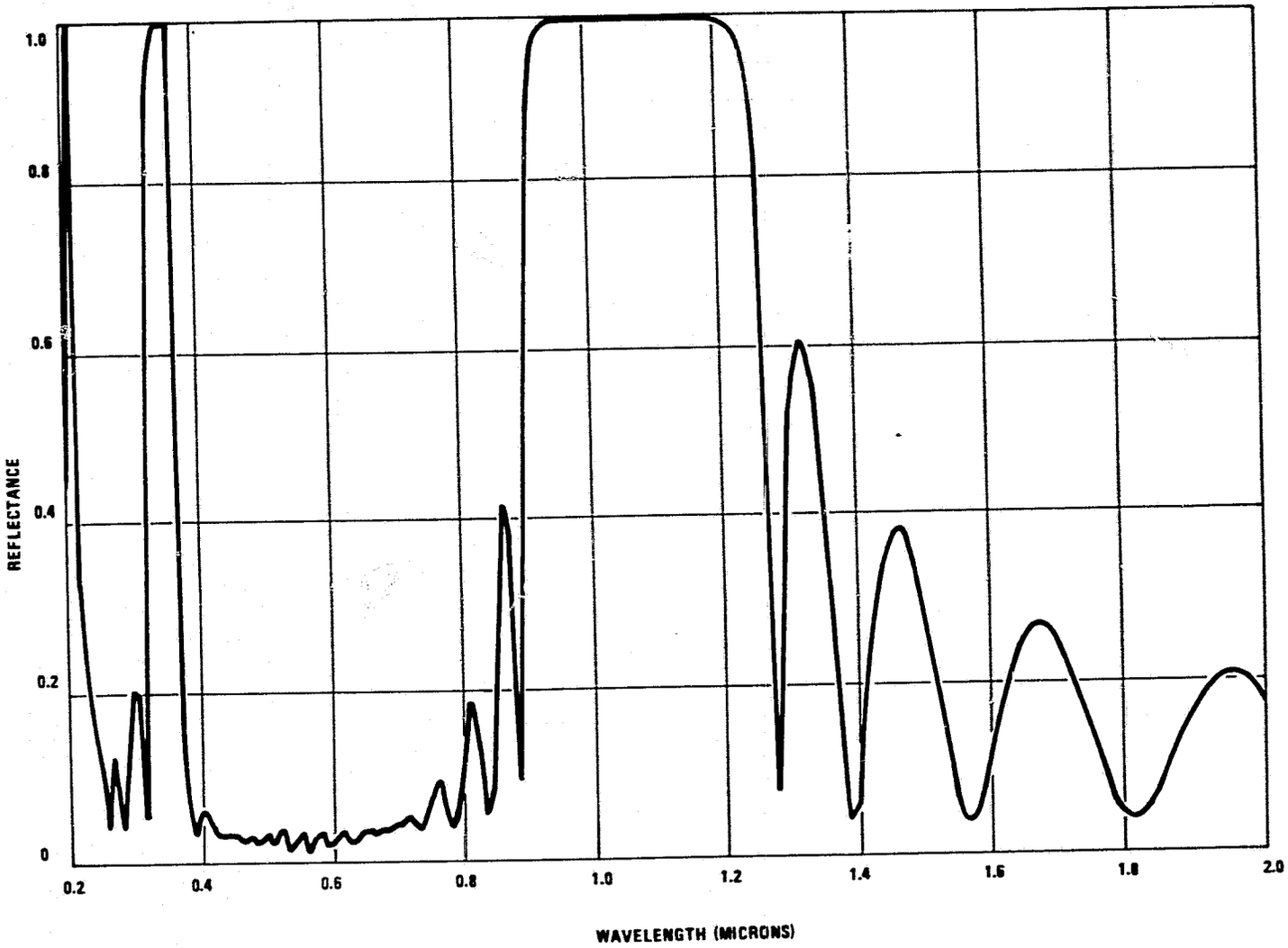

Figure 23. Computed Spectral Reflectance of a 0.9 to 1.1 μm Reflective MgF_2/TiO_2 Beam Splitter (21 layers, θ = 0 deg)

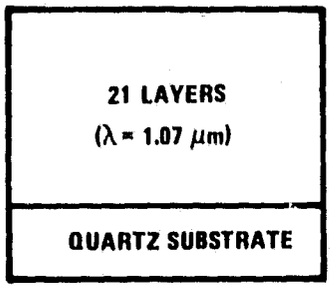

LAYERS 1 AND 21: : $t = \lambda/8n_L = 0.097\ \mu m$

LAYERS 3,5, . . . ,19: $t = \lambda/4n_L = 0.194\ \mu m$

LAYERS 2,4, . . . ,20: $t = \lambda/4n_H = 0.121\ \mu m$

Figure 24. Details of the 21-Layer MgF_2/TiO_2 Beam-Splitter Coating Design (t = physical thickness)

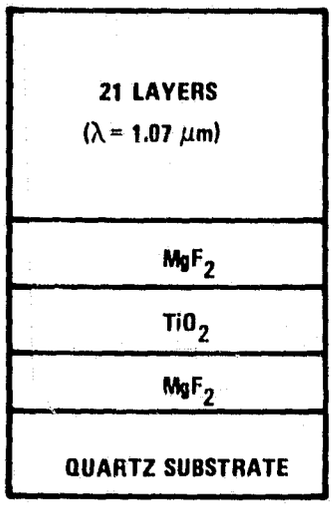

LAYERS 4 AND 24: $t = \lambda/8n_L = 0.097\ \mu m$

LAYERS 6,8, . . . ,22: $t = \lambda/4n_L = 0.194\ \mu m$

LAYERS 5,7, . . . ,23: $t = \lambda/4n_H = 0.121\ \mu m$

LAYER 3: $t = 0.116\ \mu m$

LAYER 2: $t = 0.145\ \mu m$

LAYER 1: $t = 0.116\ \mu m$

Figure 25. Details of the 24-Layer MgF_2/TiO_2 Beam-Splitter Coating Design (t = physical thickness)

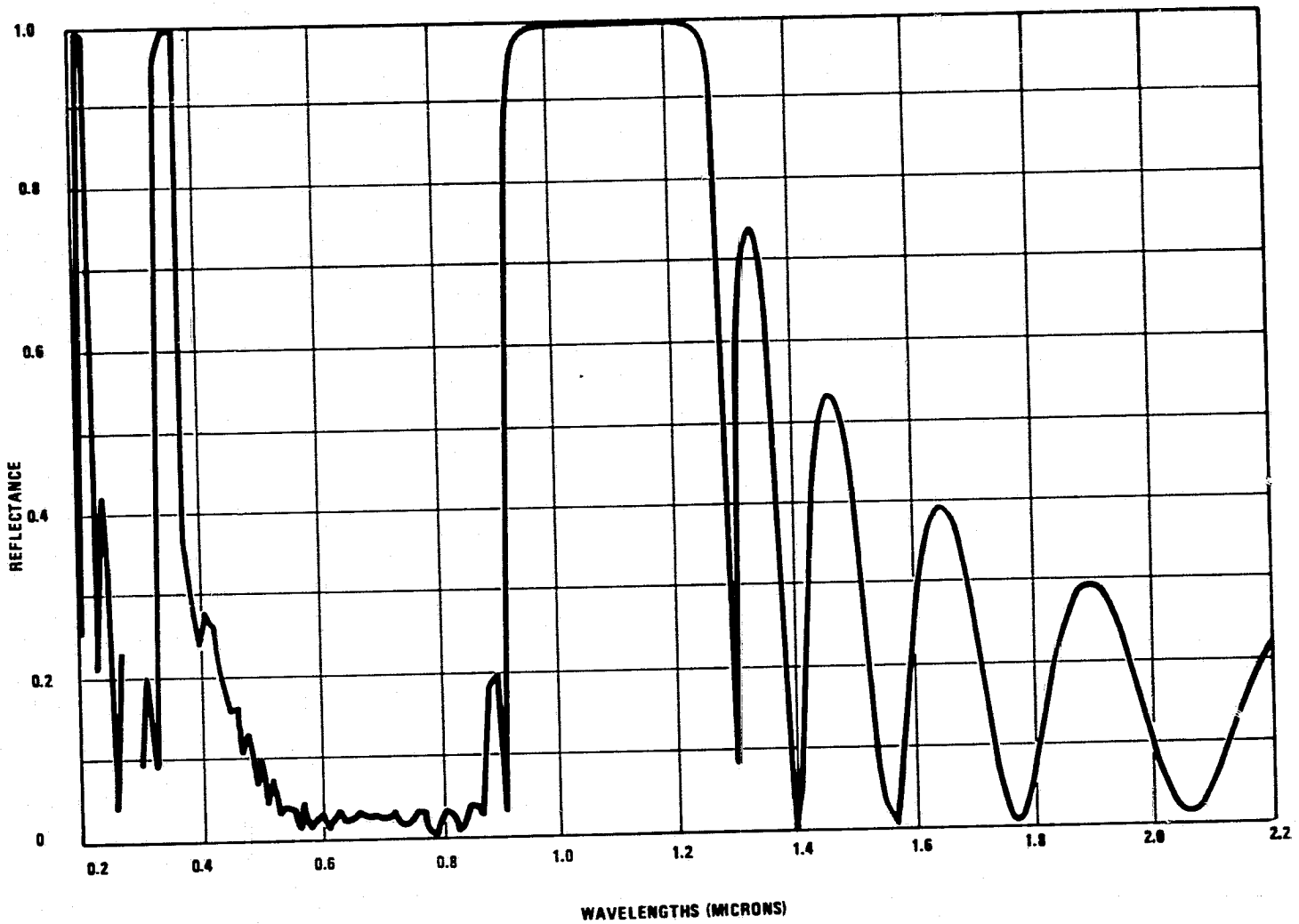

Figure 26. Computed Spectral Reflectance of a 0.9 to 1.1 μm Reflective MgF_2/TiO_2 Beam Splitter (24 layers, $\theta = 0$ deg)

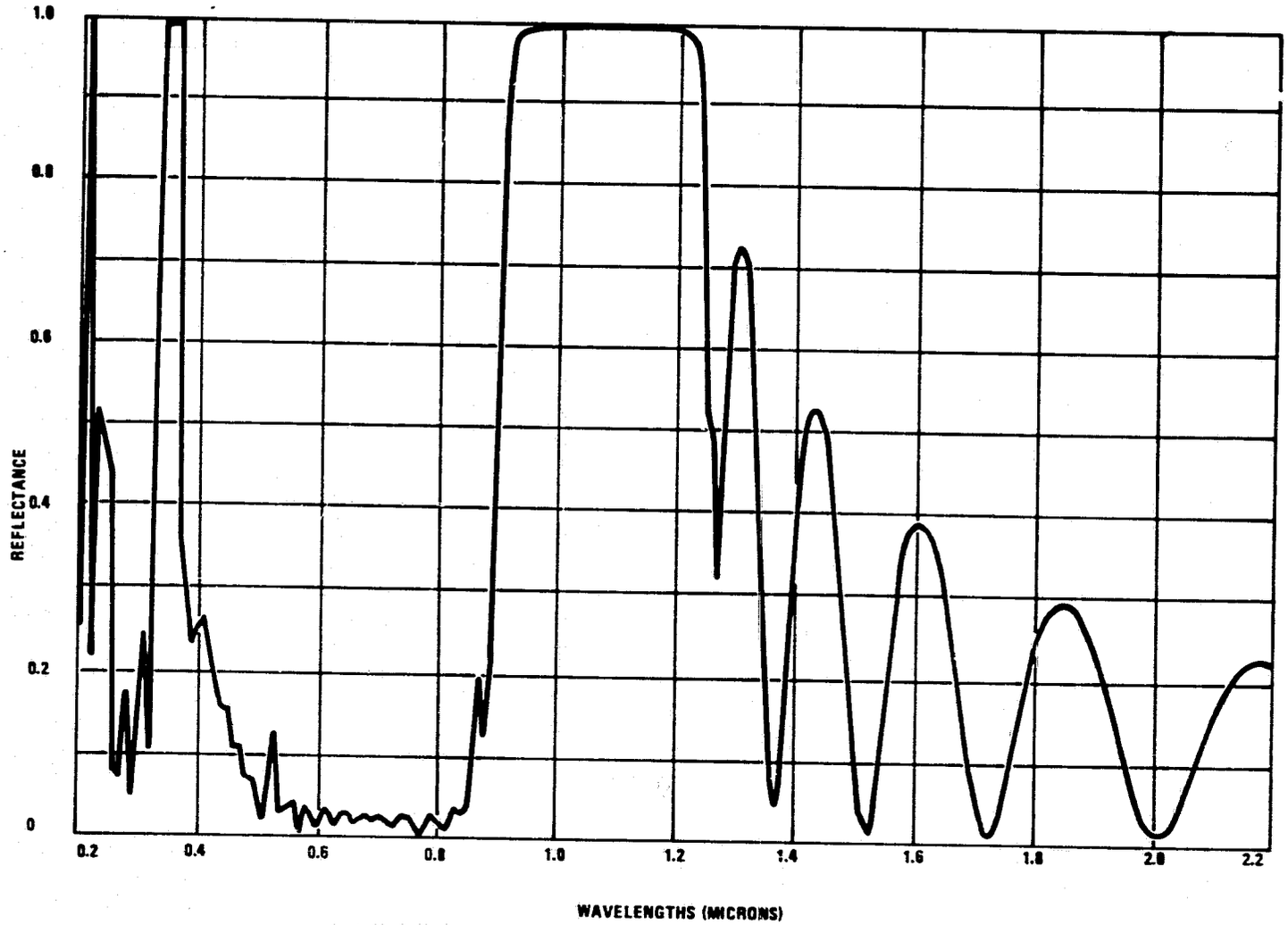

Figure 27. Computed Spectral Reflectance of a 0.9 to 1.1 μm Reflective MgF_2/TiO_2 Beam Splitter (24 layers, θ = 22 deg)

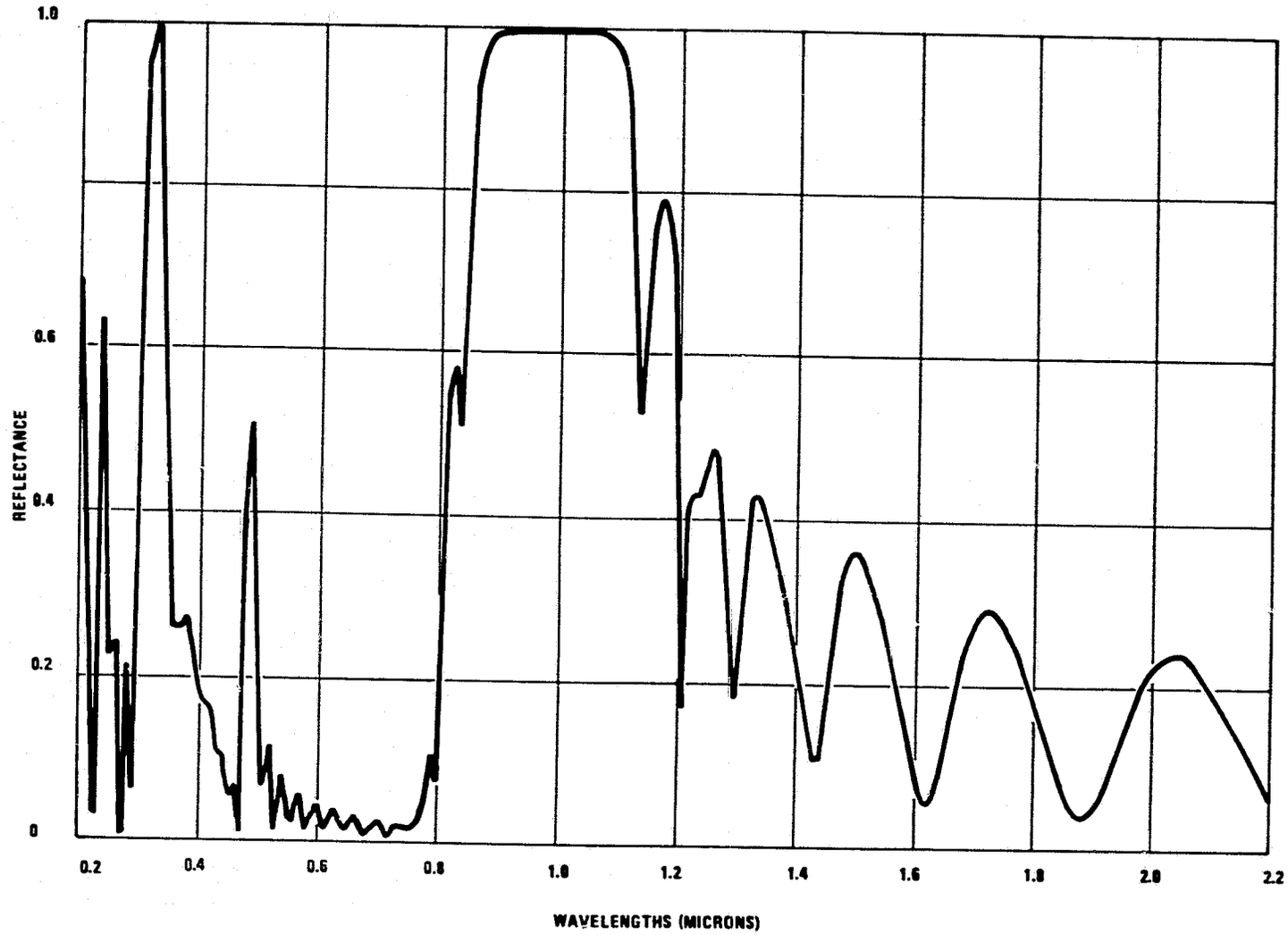

Figure 28. Computed Spectral Reflectance of a 0.9 to 1.1 μm Reflective MgF_2/TiO_2 Beam Splitter (24 layers, θ = 45 deg)

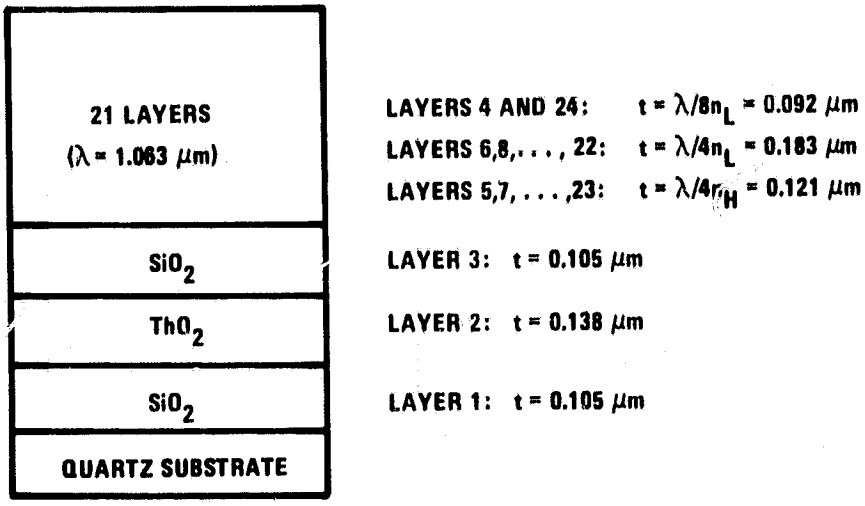

Figure 29. Details of the 24-Layer SiO_2/ThO_2 Beam-Splitter Coating Design (t = physical thickness)

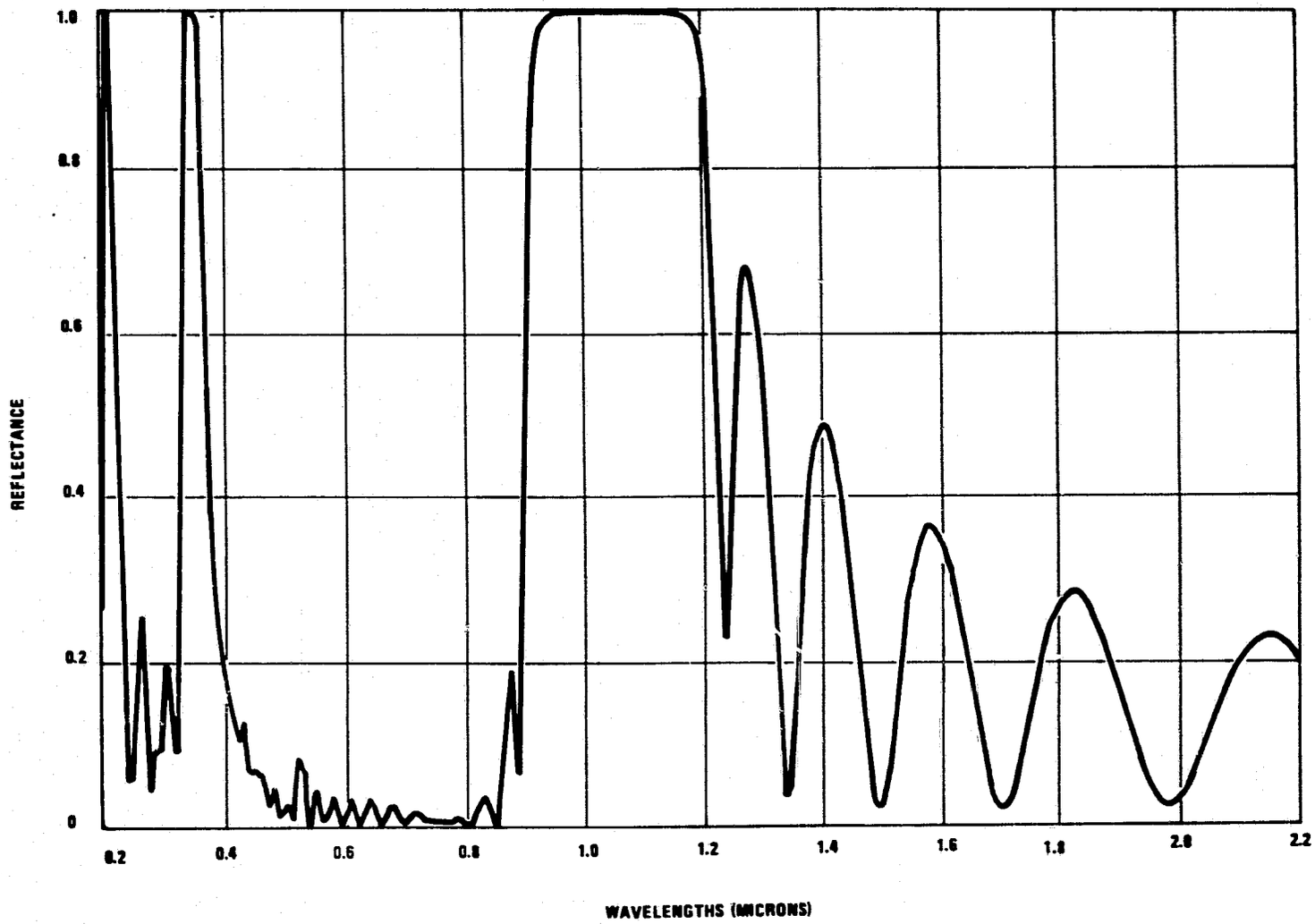

Figure 30. Computed Spectral Reflectance of a 0.9 to 1.1 μm Reflective SiO_2/ThO_2 Beam Splitter (24 layers, θ = 22 deg)

SECTION 4

SOLAR CELLS

A methodology is presented for predicting multi-solar-cell system efficiency. A realistic model is used for the diode dark current and the output power is maximized for a given photocurrent.

The ideal efficiencies for one-, two-, three-, and four-solar-cell systems were calculated under 1000 sun, AM0 conditions; optimum energy bands were determined. The ideal maximum efficiencies for one-, two-, three-, and four-cell systems are 32%, 42%, 50%, and 53%, respectively. A comparison of these optimum bandgaps and those that would be required if the cells were connected in series was made. The disadvantage of the latter approach is that materials with specific bandgaps must be used in order to meet the equal-current requirement.

The validity of using the low-injection approximation for 1000-sun intensity calculations was analyzed. It was found that for more than one-cell systems the Si and GaAs cells should not exhibit high injection effects.

Although it is possible to fabricate semiconductors with nearly any bandgap, it may be more cost effective to use materials that have already been developed for solar cell applications. Efficiencies close to the maximum ones can be obtained with some of these well-developed materials.

Calculations were made for solar cell systems using Ge, Si, GaAs, and GaP. Although Ge and GaP are not well-developed solar cells, they were chosen because both materials have been well studied. Ge transistors were used before Si electronics was developed; GaP is used in light-emitting diodes and visible radiation detectors. Realistic cell design parameters were used and account was taken of losses due to grid shadowing, cell reflection, dichroic mirrors, and nonunity spectral response. The excess power that would have to be removed from the cells in order to maintain their 300K operating temperature was calculated.

Trade-off factors such as efficiency, excess power removal requirements, number of UV-resistant dichroic mirrors, development of new solar cells, and number of cells in the system are discussed. A preliminary tradeoff analysis predicted that a GaAs/Ge system with an efficiency of about 32% may be the best choice. However, the feasibility of such a system depends on the future performance of Ge solar cells and the feasibility of removing $33 W/cm^2$ of excess power. Other choices are GaAs/Si with an efficiency of 28% and an excess power removal requirement of $23 W/cm^2$, and GaAs/GaP/Si with an efficiency of 30% and an excess power removal requirement of $12 W/cm^2$.

4.1 METHODOLOGY FOR PREDICTING SOLAR CELL PERFORMANCE

4.1.1 Multi-Solar-Cell System Efficiency

An important measure of the performance of a solar cell or a group of solar cells is the efficiency with which they convert solar energy into power. The efficiency is given by

$$\eta = \sum_{n=1}^{N} \frac{P_n}{P_{in}}$$

where

N = number of cells

P_n = output power of nth cell

P_{in} = incident solar power

For a one-cell system the maximum efficiency is that for which $P_E(J_E)$ is a maximum where

$P_E(J)$ = output power as a function of photocurrent J for a cell with energy bandgap E

J_E = total photocurrent which can be generated in a cell with energy bandgap E

$$= q \int_0^{hc/E} SR(\lambda)\, F(\lambda)\, d\lambda$$

where $F(\lambda)$ is the sunlight spectral distribution and $SR(\lambda)$ is the spectral response. Hence:

$$\eta_1 = \max\left\{P_E(J_E),\ 0 \le E \le 7\ \text{eV}\right\} / P_{in}$$

where the limits of E are chosen to cover the sun's spectrum.

For a two-cell system the sum of the output powers from two cells must be maximized with the restriction that the total current must be equal to J_{E_1}, where E_1 denotes the smaller of the two energy bandgaps. Hence:

$$\eta_2 = \max \left\{ P_{E_1}\left(J_{E_1} - J_{E_2}\right) + P_{E_2}\left(J_{E_2}\right),\ 0 \le E_1 < E_2 \le 7\text{eV} \right\} \Big/ P_{in}$$

For three- and four-cell systems the maximum efficiencies are defined in a similar way:

$$\eta_3 = \max \left\{ P_{E_1}\left(J_{E_1} - J_{E_2}\right) + P_{E_2}\left(J_{E_2} - J_{E_3}\right) + P_{E_3}\left(J_{E_3}\right) \right.$$
$$\left. 0 \le E_1 < E_2 < E_3 \le 7\text{eV} \right\} \Big/ P_{in}$$

$$\eta_4 = \max \left\{ P_{E_1}\left(J_{E_1} - J_{E_2}\right) + P_{E_2}\left(J_{E_2} - J_{E_3}\right) \right.$$
$$+ \left(P_{E_3}\left(J_{E_3} - J_{E_4}\right) + P_{E_4}\left(J_{E_4}\right)\right),$$
$$\left. 0 \le E_1 < E_2 < E_3 < E_4 \le 7\text{eV} \right\} \Big/ P_{in}$$

4.1.2 Power Maximization for a Given Photocurrent

For a single cell the output power can be expressed as a function of the photocurrent, I_p. This function, as well as I_p, depends on the properties of a given cell.

The equivalent circuit for a photovoltaic solar cell is shown in Figure 31. The photogenerated current is the sum of the currents generated in the surface, depletion, and base regions.

$$I_p = I_{surface} + I_{depletion\ region} + I_{base}$$

The diode dark current is I_d and the potential across the diode is V_j. R_s and R_{sh} are the intrinsic series and shunt resistances of the diode. The output power is

$$P_{out} = I_L V_L$$

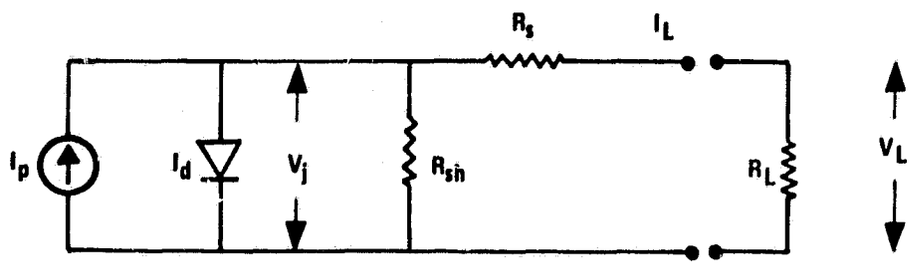

Figure 31. Equivalent Circuit of a Solar Cell

If we assume that the shunt resistance is infinite, we have

$$I_L = I_P - I_d$$

and the output power is

$$P_{out} = (I_p - I_d)\left(V_j - R_s (I_p - I_d)\right)$$

Differentiation of the output power with respect to V_j yields

$$\frac{P_{max}}{A_d} = \frac{V_j^{\,2} \dfrac{d J_d}{d V_j} \left(1 + R_s A_d \dfrac{d J_d}{d V_j}\right)}{\left(1 + 2 R_s A_d \dfrac{d J_d}{d V_j}\right)^2}$$

where

$$J_p = J_d + \frac{V_j \dfrac{d J_d}{d V_j}}{1 + 2 R_s A_d \dfrac{d J_d}{d V_j}}$$

A_d = diode cross-sectional area

The diode dark current J_d depends on V_j. Hence, given an expression for J_d one can determine P_{max} as a function of J_p.

4.1.3 Diode Dark Current

We assume that the dark current is due to injected current and space charge layer recombination current.[4] The injection current is due to electrons injected from the n-side over the potential barrier into the p-side where they diffuse away from the junction and recombine in the bulk or at the surface. (Holes are also injected from the p-side into the n-side.) The total injected current density for uniform doping levels (that is, no electric field except in the depletion region) is

$$J_{inj} = J_o(e^{qV_j/kT} - 1)$$

where, for an n/p cell,

$$J_o = q\frac{D_p}{L_p}\frac{n_i^2}{N_d}\frac{\left[\sinh\left(\frac{x_j}{L_p}\right) + \frac{S_pL_p}{D_p}\cosh\left(\frac{x_j}{L_p}\right)\right]}{\left[\cosh(x_j/L_p) + (S_pL_p/D_p)\sinh(x_j/L_p)\right]}$$

$$+ q\frac{D_n}{L_n}\frac{n_i^2}{N_a}\frac{\left[\sinh(H'/L_n) + (S_nL_n/D_n)\cosh(H'/L_n)\right]}{\left[\cosh(H'/L_n) + (S_nL_n/D_n)\sinh(H'/L_n)\right]}$$

$$H' = H - (x_j + W)$$

For a p/n cell the subscripts n and p should be reversed.

---

[4] H.J. Hovel, Semiconductors and Semimetals, Volume 11: Solar Cells. New York: Academic Press, 1975, Chapt. 3.

The space charge layer recombination current density is given by

$$J_{rg} = \frac{q\, n_i W}{\sqrt{\tau_{po}\, \tau_{no}}} \quad \frac{2 \sinh\, (q\, V_j/2\, kT)}{q\, (V_d - V_j)/kT} \quad f\,(b)$$

where f(b) is related to the energy traps. The maximum value of f(b) is $\pi/2$; we have assumed this worst case in our calculation.

High-injection effects are not taken into account in these expressions. The validity of using the low-injection approximation is discussed in subsection 4.3.

The variation of n_i^2 with E_g and T is given by[2]

$$n_i^2 = 4(2\pi\, kT/h^2)^3\, (m_e m_h)^{3/2}\, e^{-E_g(T)/kT}$$

where m_e and m_h are the density-of-state effective masses of the conduction band and valence band, respectively.

The variation of E_g with temperature is taken to be[5]

$$E_g(T) = E_g(0) - \frac{\alpha T^2}{T + \beta}$$

---

[5] S. M. Sze, Physics of Semiconductor Devices. New York: Wiley-Interscience, 1969, pp. 24, 27, 40, 57. (Mobilities are determined for the designated doping densities and at T = 300K.)

The other parameters are:

Diffusion Coefficients: $D = \frac{kT}{q} \mu(T)$

Built-In Voltage: $V_d = \frac{kT}{q} \ln (N_a N_d / n_i^2)$

Depletion Width: $W = \sqrt{\frac{2 \epsilon_s (N_a + N_d)}{q N_a N_d} V_d}$

Diffusion Lengths: $L = \sqrt{D\tau}$

4.2 IDENTIFICATION OF OPTIMUM BANDGAPS FOR ONE-, TWO-, THREE-, AND FOUR-SOLAR-CELL SYSTEMS

4.2.1 Calculation of Output Power as a Function of Photocurrent

Using the expressions given in subsection 4.1, the output power was calculated as a function of photocurrent density for photo voltaic cells with various energy bandgaps, E_g. A similar calculation was performed by Hovel[6] for AM1 conditions. Our work uses his device parameters and extends the results to AM0 conditions. For bandgaps of less than 1.3 eV, device parameters for a silicon n/p cell with a back surface field were used. For bandgaps of greater than 1.3 eV, device parameters for a GaAs p/n cell with a $Ga_{1-x}Al_xAs$ window layer were used. These device parameters are given in Table 4. A 300K operating temperature is assumed.

---

[6] H. J. Hovel, "Novel Materials and Devices for Sunlight Concentrating Systems," IBM Journal of Research and Development, Vol. 22, 1978, p. 112.

TABLE 4. DEVICE PARAMETERS[6]

Parameters	$E_g < 1.3$ eV (Si conditions, n-on-p, BSF)		$E_g > 1.3$ eV (GaAs conditions, p-on-n, GaA/As window)	
Junction depth (x_j)	0.2 μm		0.6 μm	
Surface recombination velocity, front	1×10^3 cm/s	(S_p)	1×10^4 cm/s	(S_n)
Surface recombination velocity, back	0	(S_n)	infinite	(S_p)
Doping, front	2×10^{19} cm^{-3}	(N_d)	2×10^{19} cm^{-3}	(N_a)
Doping, back	1×10^{17} cm^{-3}	(N_a)	2×10^{17} cm^{-3}	(N_d)
Lifetime, front	0.4×10^{-6} s	(τ_{po})	5×10^{-9} s	(τ_{no})
Lifetime, back	20×10^{-6} s	(τ_{no})	5×10^{-8} s	(τ_{po})
Thickness (H)	450 μm		100 μm	

The variation of n_i^2 with E_g is taken to be[6]

$$n_i^2 = \begin{cases} 4.81 \times 10^{31}\, T^3\, e^{-E_g(T)/kT} & (E_g < 1.3 \text{ eV, silicon conditions}) \\ 2.57 \times 10^{29}\, T^3\, e^{-E_g(T)/kT} & (E_g > 1.3 \text{ eV, GaAs conditions}) \end{cases}$$

The constants in the energy bandgap equations are given in Table 5, along with the relative dielectric constants (ϵ_s/ϵ_o) and the mobilities.

TABLE 5. ADDITIONAL DEVICE PARAMETERS[5]

Material	Energy Gap Parameters				Dielectric Constant	Mobilities	
	$E_g(0)$ (eV)	α (K^{-1})	β (K)	$E_g(300K)$ (eV)	$\varepsilon_s/\varepsilon_o$	μ_n ($cm^2/V\text{-}s$)	μ_p ($cm^2/V\text{-}s$)
Si	1.16	7.02×10^{-4}	1108	1.12	11.8	700	75
GaAs	1.522	5.8×10^{-4}	300	1.43	10.9	1400	230
Ge	0.741	4.56×10^{-4}	210	0.66	16	--	--

4.2.2 Calculation of the Photocurrent

The photocurrent density per unit bandwidth at a given wavelength is

$$J_p(\lambda) = qF(\lambda)\, SR(\lambda) S_n$$

where $F(\lambda)$ is the sunlight spectral distribution, $SR(\lambda)$ is the cell spectral response, and S_n is a structure factor which accounts for losses due to grid shadowing, cell reflection, and imperfect reflection and transmission by the dichroic mirrors.

In our preliminary calculations we assumed $SR(\lambda) = 1$ for λ less than the cutoff wavelength, $\lambda_{co} = hc/E_g$. Also, S_n was assumed to be unity. Hence the photocurrent is given by

$$J_p = q \int_0^{\lambda_{co}} F(\lambda)\, d\lambda$$

This photocurrent is plotted in Figure 32 as a function of E_g for AM0 conditions.

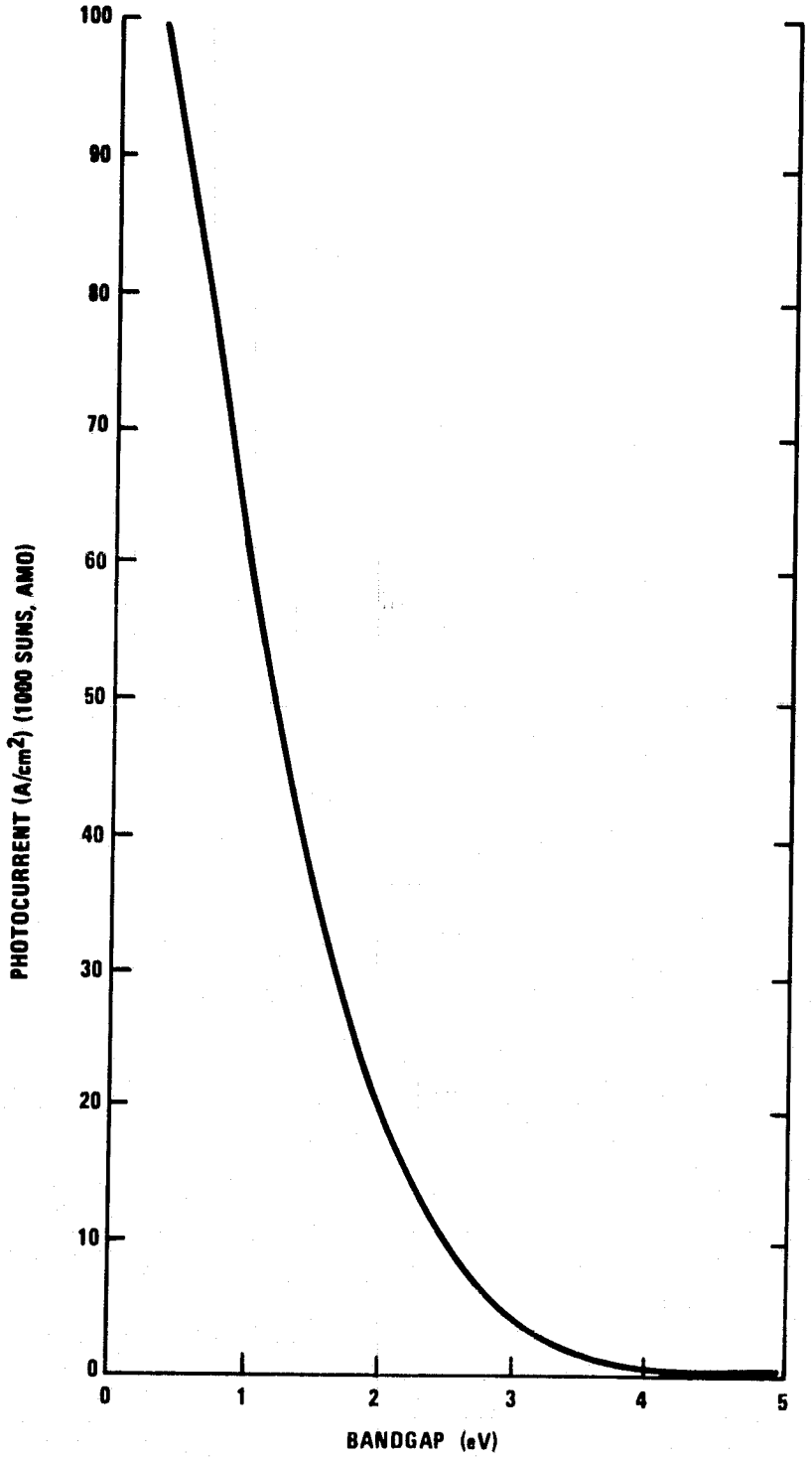

Figure 32. Maximum Photocurrent for a Given Energy Gap for AM0 Conditions

4.2.3 Calculation of the Ideal Efficiencies for Multi-Cell Systems

The ideal efficiencies for one-, two-, three-, and four-cell systems were calculated and optimum energy bands were determined. The input power is assumed to be $135.3 W/cm^2$, which is that of 1000 suns under AM0 conditions.

Most solar cells are not able to achieve their theoretical efficiencies because of series resistance, contact shadowing, and other effects. However, the identification of the optimum bandgaps can be achieved using ideal efficiency calculations. In addition, the sensitivity to variations in bandgap can be studied.

In calculating the efficiencies, three cases were considered:

- Case 1: Si Conditions--Si parameters were used to calculate the dark current.
- Case 2: GaAs Conditions--GaAs parameters were used to calculate the dark current.
- Case 3: Si/GaAs Conditions--Si parameters were used to calculate the dark current for cells with energy bandgaps less than 1.3 eV. GaAs parameters were used for the cells with larger bandgaps.

The dark current calculated using GaAs conditions is smaller so efficiencies calculated using these parameters tend to be higher than those calculated using silicon parameters. Also preliminary calculations showed that higher-bandgap materials are more efficient at converting photons to output power

than lower-bandgap materials, so it is assumed that the higher-bandgap materials absorb all photons with energy greater than their bandgap. The rest of the photons are passed on to the lower-bandgap material.

4.2.4 Results for One-Cell Systems

The output power as a function of photocurrent was calculated for various energy bandgaps. The results for Si (using Si conditions), GaAs (using GaAs conditions), and Ge (using Si conditions) are given in Figure 33 for $R_sA_d = 0$ and $0.01\Omega\text{-cm}^2$. Silicon, with a bandgap of 1.12 eV, has a theoretical efficiency of 28.4%. GaAs, with a bandgap of 1.43 eV, has a theoretical efficiency of 31%. Ge, with a bandgap of 0.66 eV, has a theoretical efficiency of 17.7%.

The higher-bandgap materials produce more power because of their smaller dark current and its dependence on the intrinsic carrier concentration n_i, which varies as $e^{-E_g/kT}$. The effect of loss of power at high current due to series resistance is greater for the lower-bandgap materials.

The efficiencies as a function of bandgap are shown in Figure 34. For a silicon-type cell the maximum efficiency of 29.2% occurs between 1.3 eV and 1.4 eV. For GaAs-type cells the maximum efficiency of 32% occurs between 1.1 eV and 1.3 eV. In the one-cell case the efficiencies of materials with bandgaps from 1.0 eV to 1.6 eV do not deviate significantly from their maximum values.

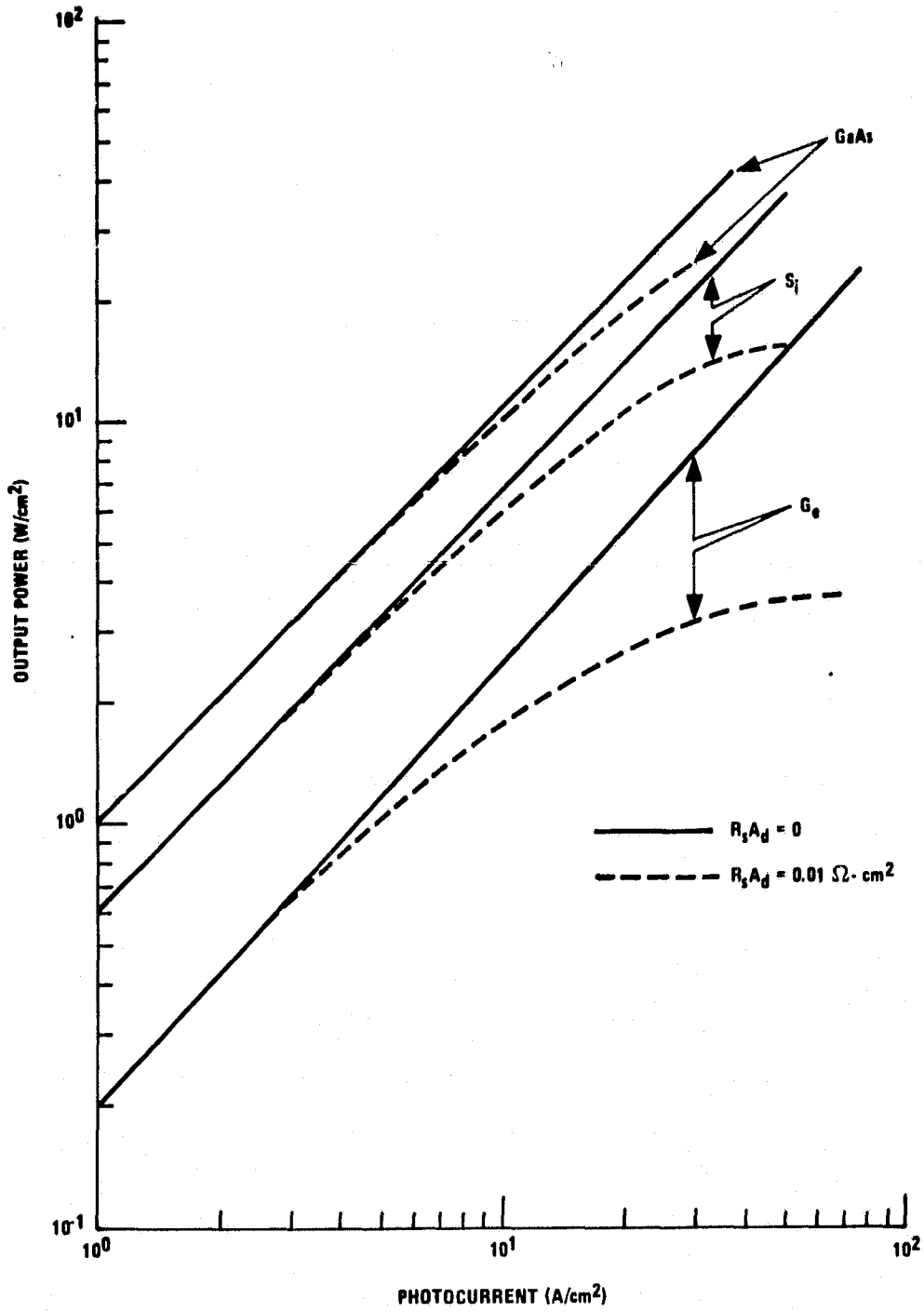

Figure 33. Output Power as a Function of Photocurrent for Si, Ge, and GaAs Solar Cells (T = 300K, R_sA_d = 0 and 0.01Ω-cm^2)

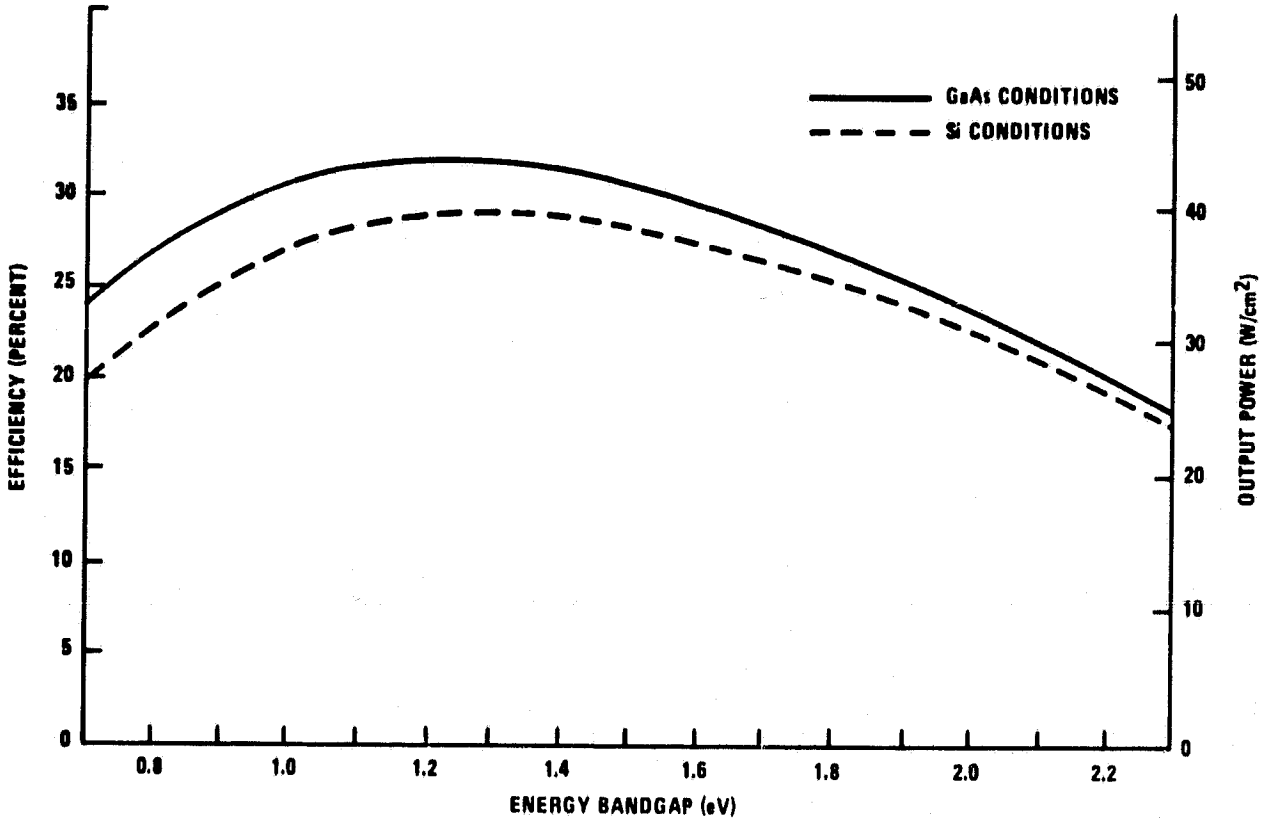

Figure 34. Ideal Efficiency for a One-Cell System as a Function of Energy Bandgap

4.2.5 Results for Two-Cell Systems

The output power for combinations of two solar cells with different energy bandgaps was calculated. The results for a combination of Si and GaAs solar cells as a function of the silicon photocurrent are shown in Figure 35. Zero series resistance was assumed. The conditions on the photocurrents for 1000 suns are

$$J_{Si} \leq 53.5 A/cm^2$$

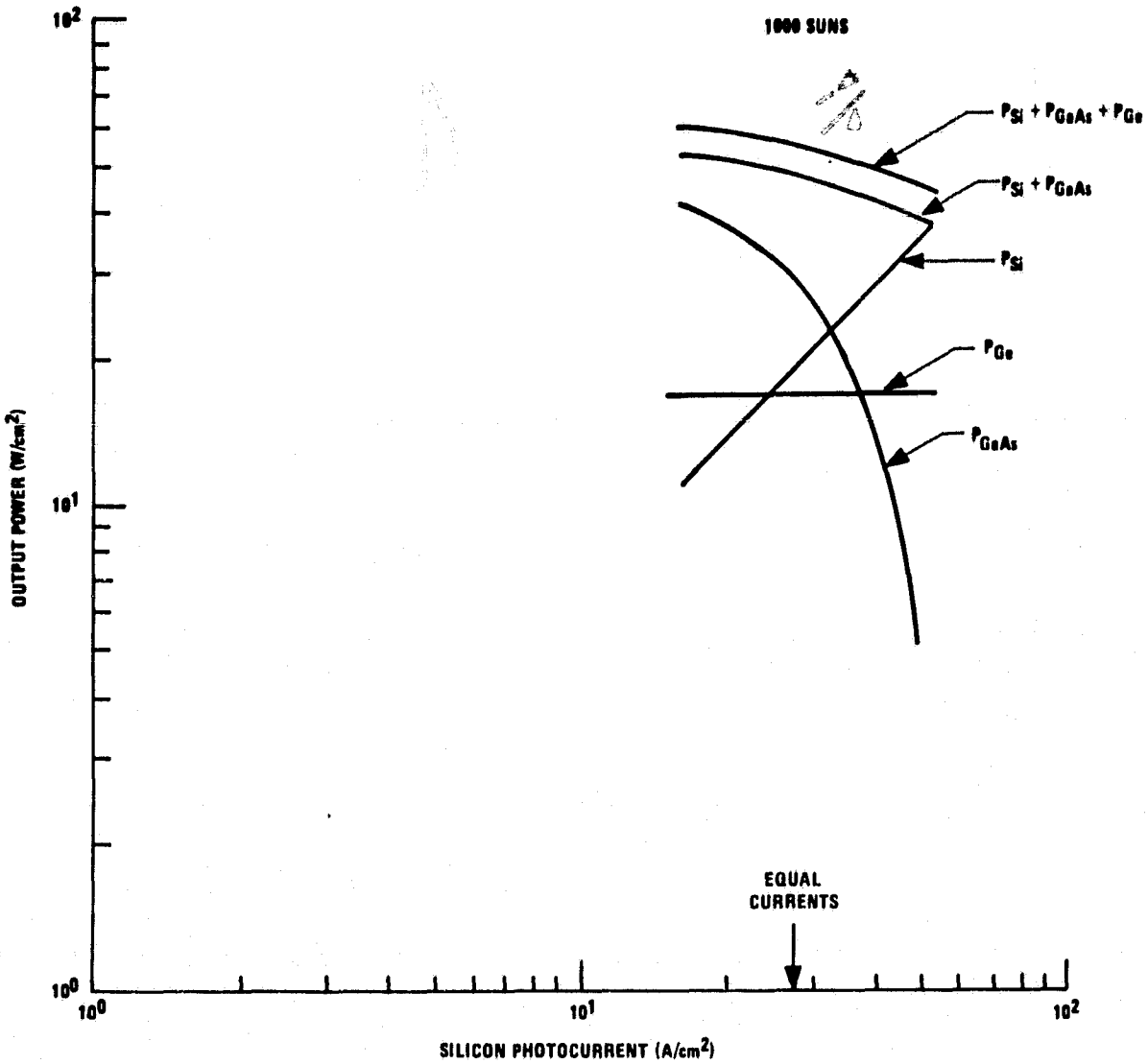

Figure 35. Output Power as a Function of Silicon Photocurrent for Two- and Three-Cell Configurations (T = 300K, R_sA_d = 0, AM0)

$$J_{GaAs} \leq 37.5 A/cm^2$$

$$J_{Si} + J_{GaAs} \leq 53.5 A/cm^2$$

From the figure it is seen that optimum power results when

$$J_{Si} = 16 A/cm^2$$

$$J_{GaAs} = 37.5 A/cm^2$$

This is because GaAs is more efficient than Si at creating power from a given number of incident photons for energies greater than its bandgap. The total power from the two solar cells is also shown. Its maximum is $53 W/cm^2$.

For the three sets of conditions, the efficiencies as a function of the highest bandgap energy, E_2, are shown in Figures 36, 37, and 38. The different curves shown in each figure correspond to values (in electron volts) of the lower bandgap energies, denoted by arrows.

For all three cases the peak efficiency is greater than 40%. In Figure 39 the range of bandgaps for which the efficiency is greater than 40% is denoted by the boundary of a closed curve for each case. The discontinuity in the curve for Si/GaAs conditions is due to the abrupt change in conditions at 1.3 eV.

For the three cases the maximum efficiencies and the ranges of the two bandgaps are given in Table 6.

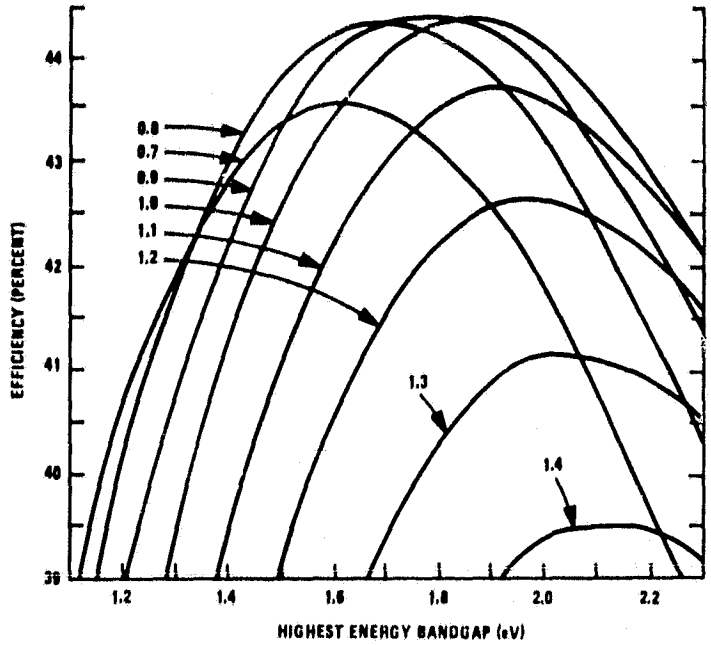

Figure 36. Efficiency of a Two-Cell System for GaAs Conditions as a Function of the Higher Energy Bandgap

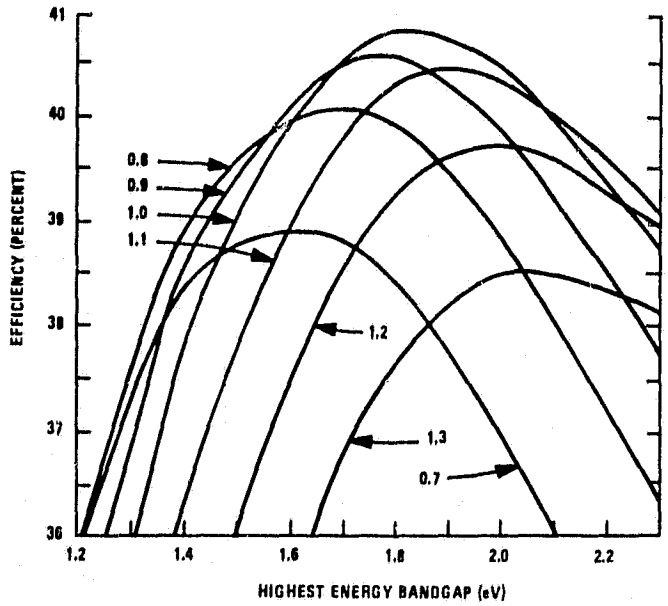

Figure 37. Efficiency of a Two-Cell System for Si Conditions as a Function of the Higher Energy Bandgap

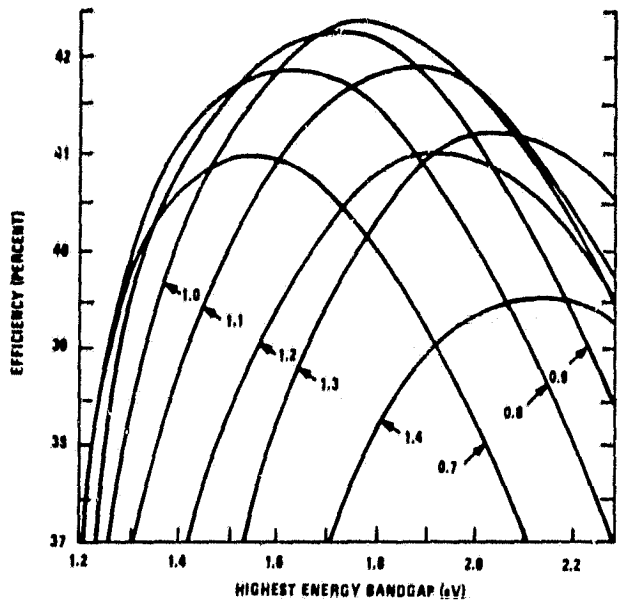

Figure 38. Efficiency of a Two-Cell System: 1) Si Conditions for $E_g < 1.3$ eV and 2) GaAs Conditions for $E_g \geq 1.3$ eV as a Function of the Higher Energy Bandgap

TABLE 6. OPTIMUM BANDGAPS AND MAXIMUM EFFICIENCIES FOR TWO-CELL SYSTEMS

Conditions	Range of E_1 (eV)	Range of E_2 (eV)	Maximum Efficiency (percent)
Si	0.9-1.1	1.7-2.0	40.8
GaAs	0.8-1.0	1.6-1.9	44.5
Si/GaAs	0.9-1.0	1.7-1.9	42.4

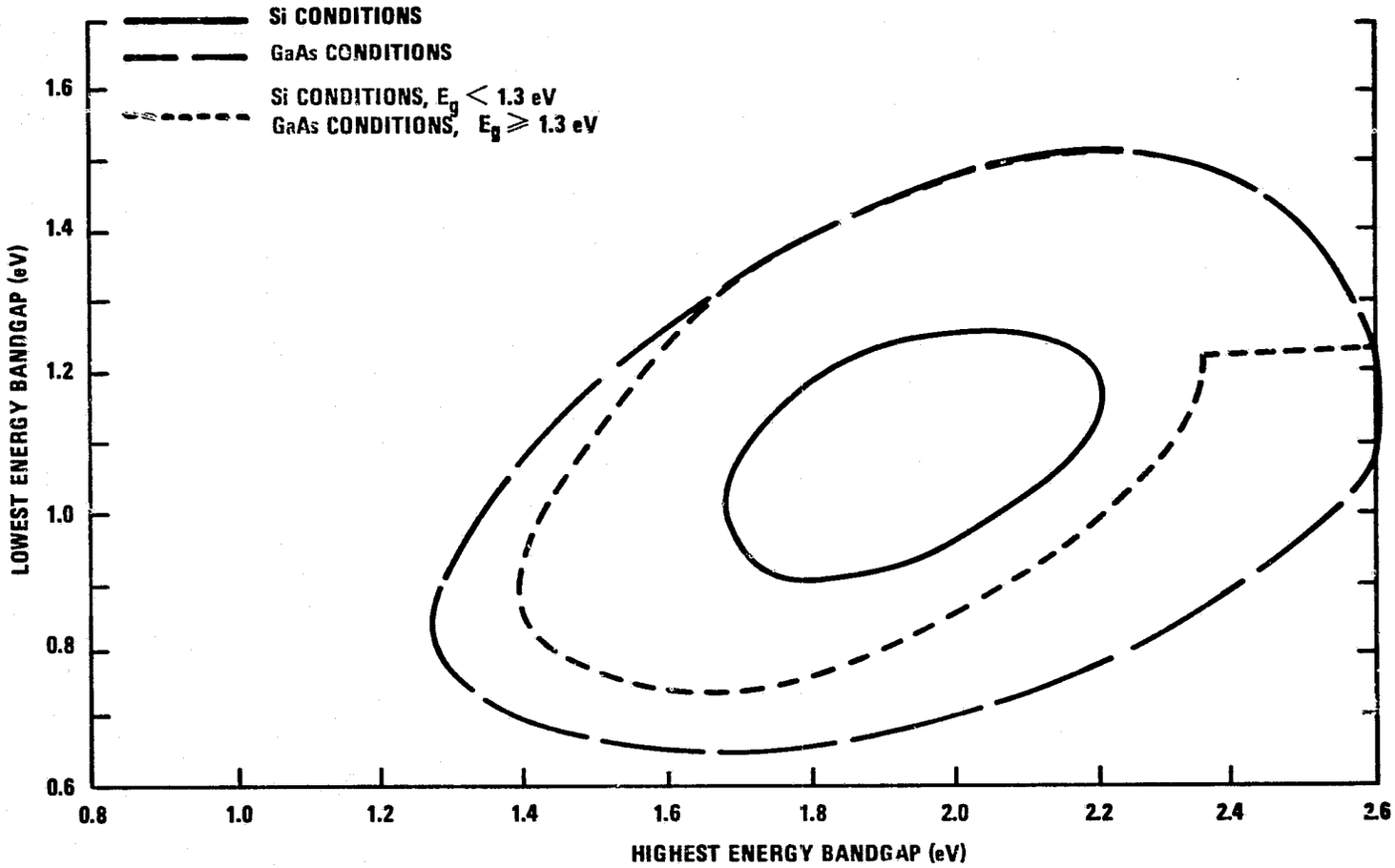

Figure 39. Range of Energy Bandgaps for a Two-Cell System in Which the Efficiency is Greater than 40%

As in the one-cell case the optimum bandgaps do not depend much on the conditions. For the two-cell system the Si/GaAs conditions are the most realistic. The predicted maximum efficiency of 42.4% is not much larger than that predicted for a Si(1.12 eV) and GaAs (1.43 eV) combination whose efficiency is 39%. Both are an improvement over the one-cell maximum of 31 to 32%.

4.2.6 Results for Three-Cell Systems

The efficiencies for the three cases as a function of highest energy bandgap, E_3, are shown in Figure 40. The middle energy bandgaps, in electron volts, are denoted by arrows. The peak efficiencies occur for $0.7 \leq E_1 \leq 0.8$, as can be seen in the figure.

For the three cases the maximum efficiencies and the ranges of the three optimum bandgaps are given in Table 7.

TABLE 7. OPTIMUM BANDGAPS AND MAXIMUM EFFICIENCIES FOR THREE-CELL SYSTEMS

Conditions	Range of E_1 (eV)	Range of E_2 (eV)	Range of E_3 (eV)	Maximum Efficiency (percent)
Si	0.7-0.8	1.2-1.4	2.0-2.2	46.85
GaAs	0.7-0.8	1.2-1.4	1.9-2.2	51.25
Si/GaAs	0.7-0.8	1.3-1.4	2.0-2.2	49.45

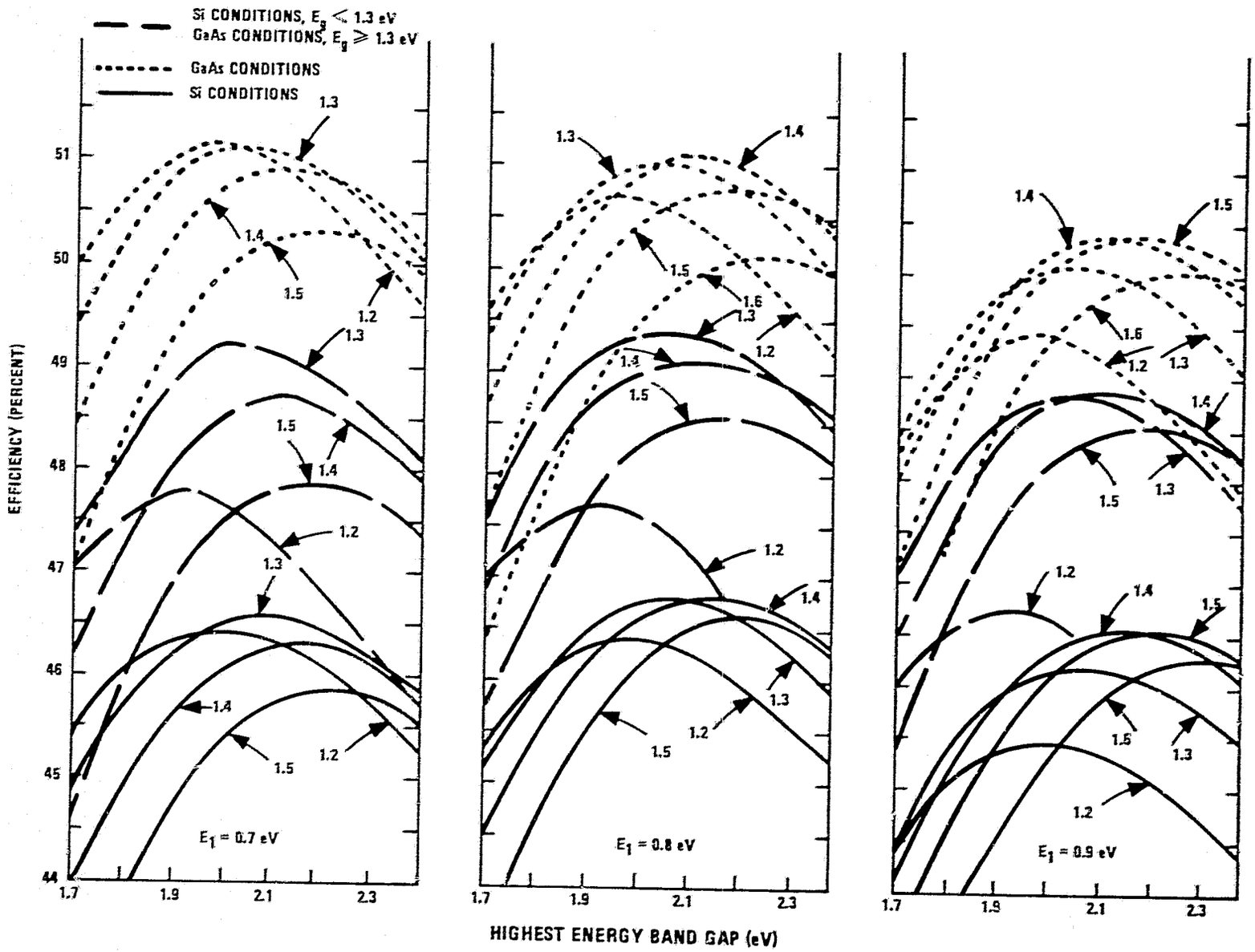

Figure 40. Efficiency for a Three-Cell System as a Function of Highest Energy Gap

As in the one- and two-cell cases the optimum bandgaps do not depend much on conditions. For the three cases the efficiencies as a function of lowest energy bandgap are shown in Figure 41. They all peak at about 0.8 eV. For the three-cell system the Si/GaAs conditions are the most realistic.

The predicted efficiency of 49.45% is not much larger than that predicted for combinations of Ge (0.66 eV), Si (1.12 eV), GaAs (1.43 eV), and GaP (2.25 eV). The possible efficiencies using these materials are:

Si-GaAs-GaP:	46.6%
Ge-Si-GaAs:	44.1%
Ge-Si-GaP:	46.0%
Ge-GaAs-GaP:	48.6%

Although the Ge-GaAs-GaP combination has the highest efficiency, both Ge and GaP must be developed as solar cells whereas Si and GaAs have been well studied. Hence, the Si-GaAs-GaP combination appears to be the most cost-effective combination.

All of these combinations are a significant improvement over the two-cell system efficiencies of 39% to 42% for the Si/GaAs conditions. However, this improvement must be weighed against the cost of developing a new solar cell, namely Ge or GaP.

4.2.7 Results for Four-Cell Systems

The efficiencies for the Si/GaAs conditions as a function of highest bandgap, E_4, are shown in Figure 42. The next highest energy bandgaps, E_3, are

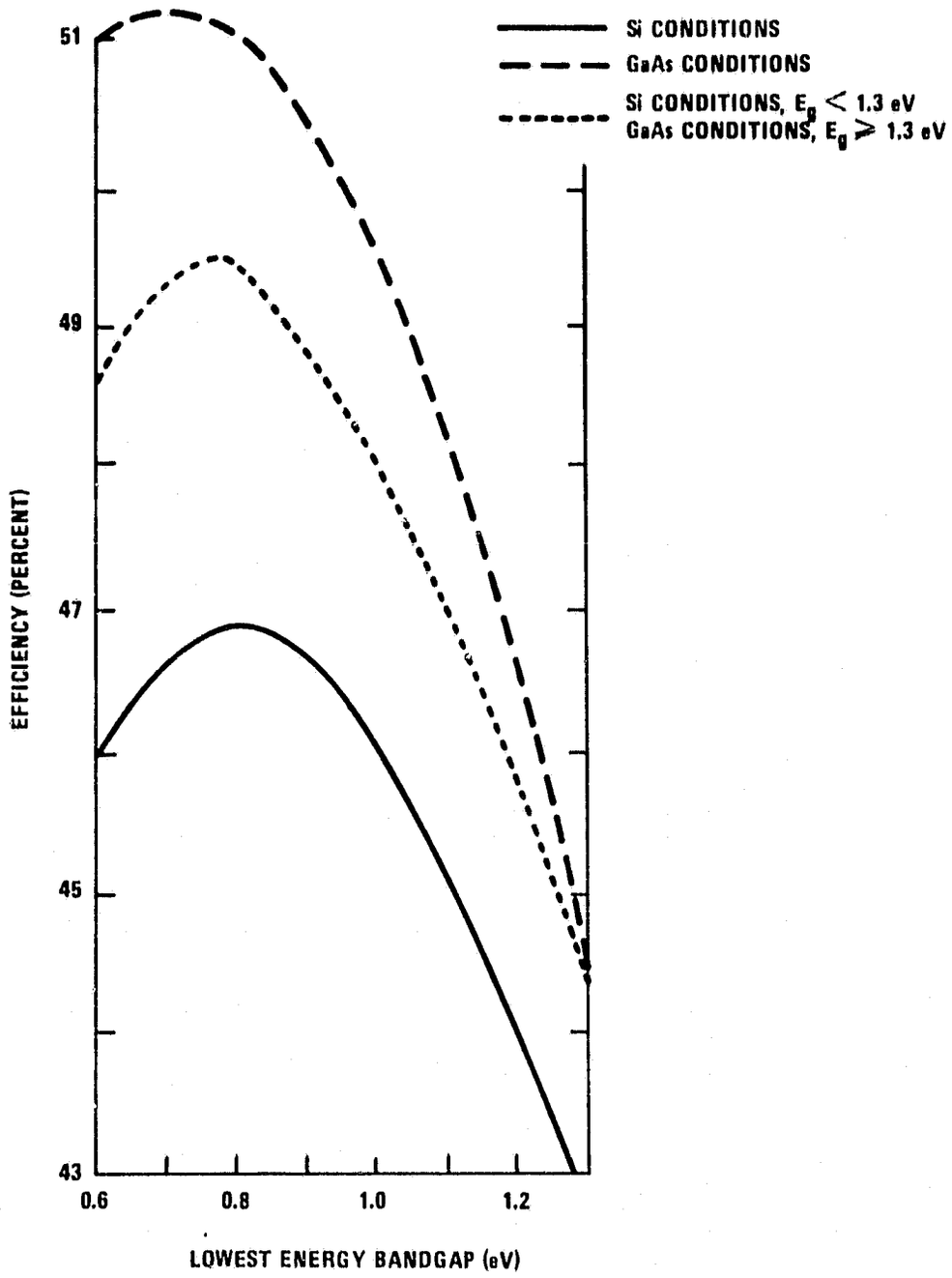

Figure 41. Efficiency of a Three-Cell System as a Function of Lowest Energy Bandgap

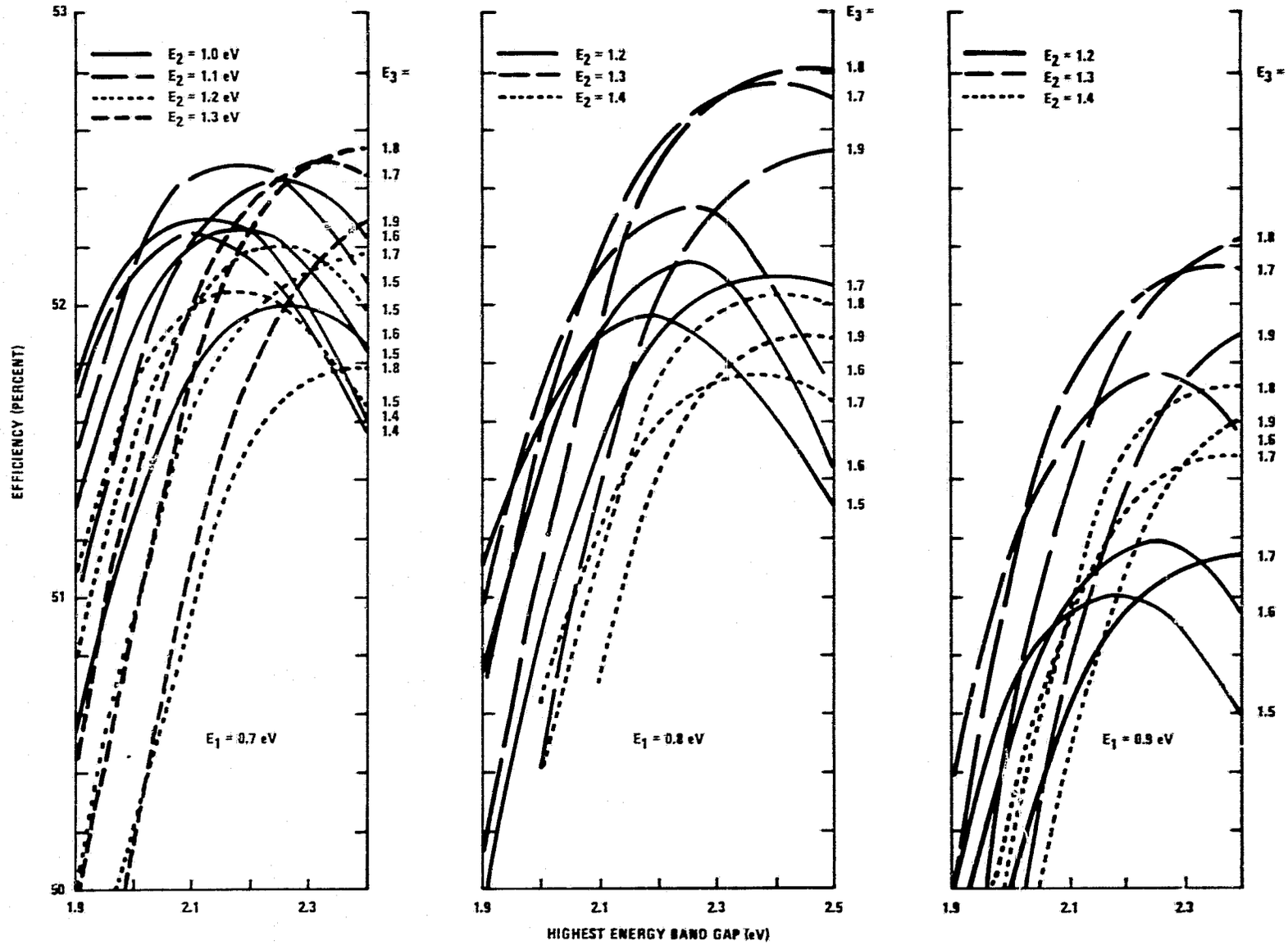

Figure 42. Efficiency of a Four-Cell System for Si/GaAs Conditions as a Function of Highest Energy Bandgap

denoted by arrows. Curves for various values of E_2 are shown. The peak efficiencies occur for E_1 = 0.8 eV, as can be seen in the figure.

For the Si/GaAs case the maximum efficiencies and the ranges of the four optimum bandgaps are given in Table 8.

As in the other cases the optimum bandgaps do not depend much on conditions. For the three cases the efficiencies as a function of lowest energy bandgap are shown in Figure 43. They all peak between 0.6 eV and 0.8 eV.

For the four-cell system the Si/GaAs conditions are the most realistic. The predicted efficiency of 52.8% is not much larger than that predicted for Ge-Si-GaAs-GaP (which is 52.2%), or even that predicted for Si-GaAs-GaP (which is 46.6%). The additional cost required to develop a Ge cell must be weighed against the potential 5.6% increase in efficiency.

TABLE 8. OPTIMUM BANDGAPS AND MAXIMUM EFFICIENCIES FOR FOUR-CELL SYSTEMS

Conditions	Range of E_1 (eV)	Range of E_2 (eV)	Range of E_3 (eV)	Range of E_4 (eV)	Maximum Efficiency (percent)
Si	0.7-0.8	1.1-1.3	1.6-1.7	2.2-2.4	50.75
GaAs	0.7	1.1-1.3	1.6-1.8	2.2-2.4	55.15
Si/GaAs	0.7-0.8	1.1-1.3	1.5-1.8	2.2-2.5	52.8

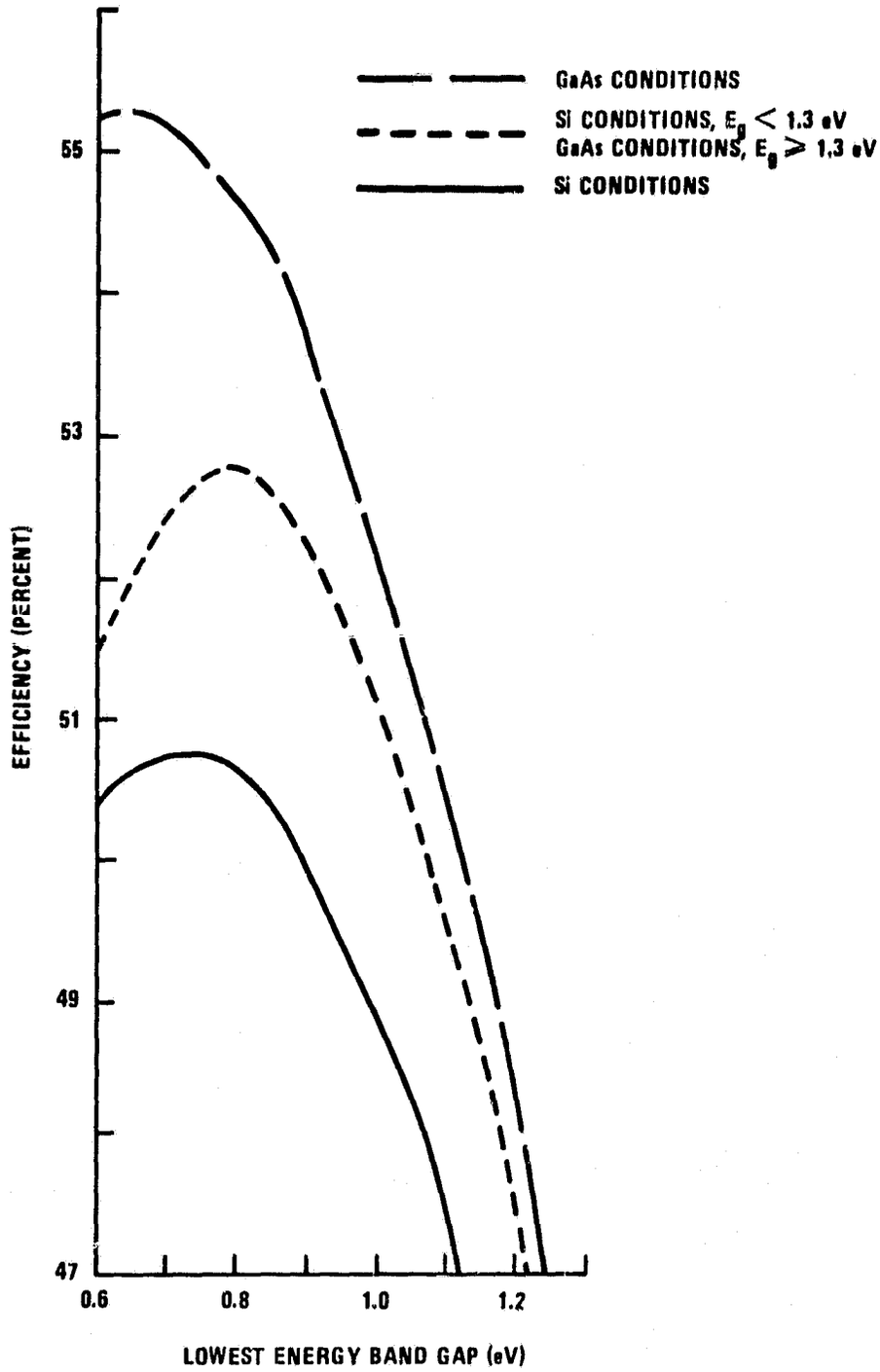

Figure 43. Efficiency of a Four-Cell System as a Function of Lowest Energy Bandgap

4.2.8 Comparison of One-, Two-, Three-, and Four-Cell Systems

One-, two-, three-, and four-cell systems were analyzed. The maximum ideal efficiencies as a function of number of cells are shown in Figure 44 for the three cases, which differ only in their dark current characteristics. It is apparent that the dependence on the number of cells is essentially independent of the dark current conditions. For the most realistic case--Si conditions for low-bandgap materials and GaAs conditions for high-bandgap materials--the maximum efficiencies and optimum energy bands are given in Table 9.

Although it is possible to fabricate semiconductors with nearly any energy bandgap, it may be more cost effective to use materials that have already been developed for solar cell applications. Efficiencies close to the maximum

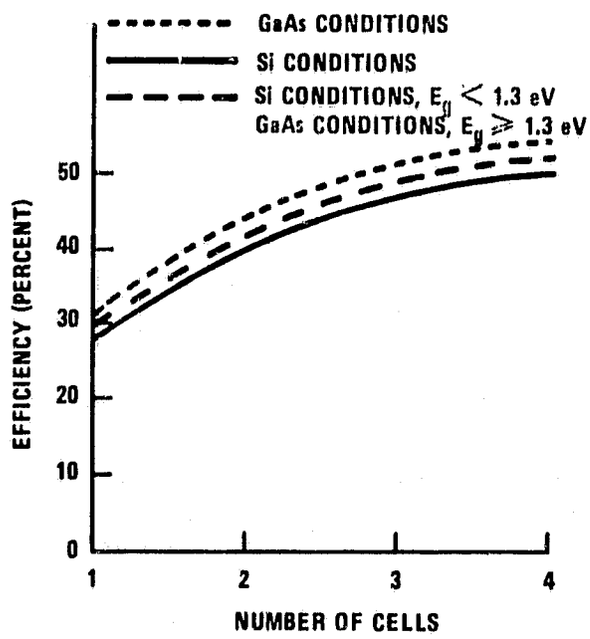

Figure 44. Ideal Efficiency of a Multi-Solar-Cell System Composed of One, Two, Three, and Four Solar Cells

TABLE 9. OPTIMUM ENERGY BANDS AND MAXIMUM EFFICIENCIES FOR 1000 SUNS, AM0 CONDITIONS

Number of cells	E_1 (eV)	E_2 (eV)	E_3 (eV)	E_4 (eV)	Maximum Efficiency (percent)
1	1.1-1.3				32.2
2	0.9-1.0	1.7-1.9			42.4
3	0.7-0.8	1.3-1.4	2.0-2.2		49.5
4	0.7-0.8	1.1-1.3	1.5-1.8	2.2-2.5	52.8

ones can be obtained with some of these well-developed materials. Some candidate materials for the multi-cell systems are given in Table 10. They are analyzed in more detail in subsection 4.4.

4.2.9 Comparison of Optimum Bandgaps and Those Determined by an Equal-Current Requirement

Two options exist for combining the outputs of the individual arrays: One is to operate them in series, thus requiring their output currents to be equal. The other, which is more complicated, is to let the cells have different currents and to use separate inversion, conversion, and combination operations. In order to study the effect of requiring equal currents from each cell, calculations (using Si/GaAs conditions) were made using this assumption. The results are shown in Figure 45, where the maximum

TABLE 10. CANDIDATE MATERIALS AND PREDICTED EFFICIENCIES FOR 1000 SUNS, AM0 CONDITIONS

Number of cells	Combination	Efficiency (percent)
1	GaAs	31
2	Si-GaAs	39
3	Si-GaAs-GaP	46.6
4	Ge-GaAs-Si-GaP	52.2

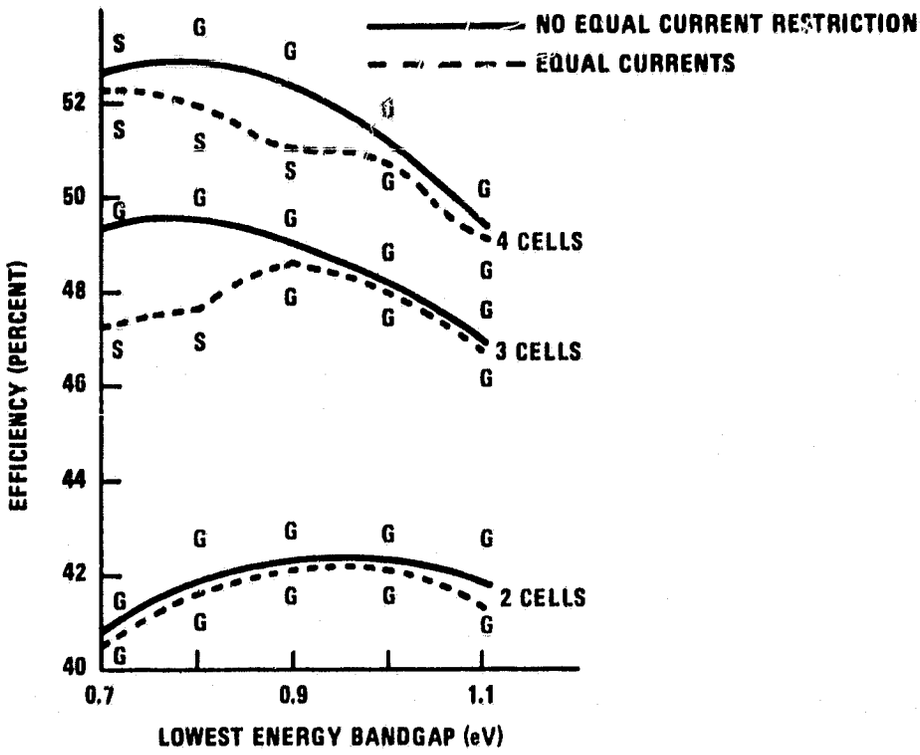

Figure 45. Efficiency Comparison of Si/GaAs Conditions for Two-, Three-, and Four-Cell Systems; for Which 1) the Currents from All Cells are Required to Be Equal and 2) there is No Restriction on Currents (The letters S and G designate whether the power from the materials with bandgap E_2 is determined using Si conditions--$E_2 < 1.3$ eV--or GaAs conditions--$E_2 \geq 1.3$ eV.)

efficiency is plotted as a function of the lowest energy bandgap. The results without the equal-current requirement are included for comparison. The differences between the two cases are most notable when the second bandgap is less than 1.3 eV for the equal current case and greater than 1.3 eV for the non-equal current case. Hence, these discrepancies are a result of our theoretical assumptions and may not be realistic.

Table 11 lists the results of the equal-current analysis for two-, three-, and four-cell systems. For five values of the lowest bandgap, the higher bandgaps are given, along with the system efficiency. The disadvantage of this approach is that materials with specific bandgaps must be used in order to meet the equal-current requirement. In addition, the current values must be predictable because the output current can be no larger than the smallest current from each of the cells. Consequently, this approach tends to require more new solar cell development.

TABLE 11. BANDGAPS AND EFFICIENCIES OF SOLAR CELLS CONNECTED IN SERIES

	Two Cells		Three Cells			Four Cells			
E_1 (eV)	E_2 (eV)	Efficiency (percent)	E_2 (eV)	E_3 (eV)	Efficiency (percent)	E_2 (eV)	E_3 (eV)	E_4 (eV)	Efficiency (percent)
0.7	1.4	40.6	1.15	1.75	47.3	1.0	1.4	2.0	52.2
0.8	1.5	41.7	1.2	1.85	47.6	1.1	1.5	2.1	52.0
0.9	1.6	42.1	1.3	1.9	48.6	1.2	1.6	2.15	51.0
1.0	1.65	42.1	1.4	2.0	48.1	1.3	1.65	2.2	50.8
1.1	1.7	41.5	1.5	2.1	46.9	1.4	1.7	2.3	49.2

4.3 VALIDITY OF USING THE LOW-INJECTION APPROXIMATION FOR 1000-SUN INTENSITIES

The equations which are valid for low-injection conditions were used to compute the changes in the minority carrier densities when concentrations of 1000 suns are incident on silicon and gallium arsenide solar cells. These numbers were found to be lower than the doping densities in all cases as long as the series resistance term is negligible. In both of the diffused regions and in the GaAs base, the low-injection approximation appears to be valid. However, a series resistance-area product of $R_s A_d = 0.01\Omega\text{-cm}^2$ brought the excess electron density in the silicon p-type base up to a value comparable to the doping density. If Si is used in conjunction with a GaAs cell, the photocurrent is lower and the low-injection approximation again appears to be valid.

4.3.1 Methodology

For low-injection conditions and uniform doping in a n/p diode, the excess minority carrier density in the p-type base is given by

$$\Delta n_p = (n_p - n_{p0}) = \frac{\alpha F(1 - R)\tau_n}{(\alpha^2 L_n^2 - 1)} \exp[-\alpha(x_j + W)] \left[\cosh \frac{x - x_j - W}{L_n} - \exp[-\alpha(x - x_j - W)] \right.$$

$$\left. - \frac{\left(\frac{S_n L_n}{D_n}\right)\left[\cosh \frac{H'}{L_n} - \exp(-\alpha H')\right] + \sinh \frac{H'}{L_n} + \alpha L_n \exp(-\alpha H')}{(S_n L_n / D_n) \sinh (H' / L_n) + \cosh (H' / L_n)} \sinh \frac{x - x_j - W}{L_n} \right]$$

$$+ n_{p0} \left(e^{qV_j/kT} - 1\right) \frac{\left[\cosh \frac{H - x}{L_n} + \frac{S_n L_n}{D_n} \sinh \frac{H - x}{L_n}\right]}{\left[\cosh \frac{H'}{L_n} + \frac{S_n L_n}{D_n} \sinh \frac{H'}{L_n}\right]}$$

where the last term, which depends on the bias voltage across the diode, V_j, is the diffusion dark current contribution. The parameters in the expression were defined in subsection 4.1. For these calculations we assume the absorption coefficient α is a constant and F is the total photon flux, for 1000 suns, for photons with energies greater than the bandgap of the solar cell.

The minority carrier density in an n-type top diffusion region is given by

$$\Delta p_n = (p_n - p_{n0}) = \left[\alpha F(1 - R)\tau_p/(\alpha^2 L_p^2 - 1)\right]$$

$$\left[\frac{\left(\frac{S_p L_p}{D_p} + \alpha L_p\right)\sinh\frac{x_j - x}{L_p} + \exp(-\alpha x_j)\left(\frac{S_p L_p}{D_p}\sinh\frac{x}{L_p} + \cosh\frac{x}{L_p}\right)}{\frac{S_p L_p}{D_p}\sinh\frac{x_j}{L_p} + \cosh\frac{x_j}{L_p}} - \exp(-\alpha x)\right]$$

$$+ p_{n0}\left(e^{qV_j/kT} - 1\right)\frac{\left[\cosh\frac{x}{L_p} + \frac{S_p L_p}{D_p}\sinh\frac{x}{L_p}\right]}{\left[\cosh\frac{x_j}{L_p} + \frac{S_p L_p}{D_p}\sinh\frac{x_j}{L_p}\right]}$$

The condition of quasi-neutrality requires that

$$\Delta n_p = \Delta p_p$$

$$\Delta p_n = \Delta n_n$$

Also, we have

$$n_{n0}p_{n0} = p_{p0}n_{p0} = n_i^2$$

$$n_{n0} \approx N_D$$

$$p_{p0} \approx N_A$$

These equations are used to determine the minority carrier densities in the Si n/p cell and the GaAs p/n cell described in the previous subsection. The diode potential V_j for maximum power output was determined by including both the diffusion and the generation-recombination parts of the dark current. For Si the diffusion current dominates. For GaAs the two parts are of the same order of magnitude.

4.3.2 Si n/p Cell

If Si is used as a single-cell system, the photocurrent is $52.5 A/cm^2$ and the photon flux is $F = 3.28 \times 10^{20}/cm^2$. We assumed an average absorption coefficient α of $1 \times 10^5/cm$. The bias potential is given by

$$\frac{qV_j}{kT} = \begin{cases} 29.35, & R_sA_d = 0 \\ 31.51, & R_sA_d = 0.01\Omega\text{-cm}^2 \end{cases}$$

If Si is used with GaAs in a two-cell system, its photocurrent is $15 A/cm^2$ and the photon flux is $F = 9.375 \times 10^{19}/cm^2$. The bias potential is given by

$$\frac{qV_j}{kT} = \begin{cases} 28.14, & R_s A_d = 0 \\ 28.59, & R_s A_d = 0.01\ \Omega\text{-cm}^2 \end{cases}$$

In all of the above cases, the value of the excess carrier densities in the base was dominated by the contribution from the dark current term, due to high V_j, rather than that from the photocurrent term. In the diffused region the photocurrent term dominates at the front and the dark current term dominates at the junction edge. The results of the calculations are presented in Table 12.

The maximum densities occur at the front of the diffused region and at the junction side of the base region. The only case where low-injection conditions are not valid is at the junction edge in the base for one-cell operation and $R_s A_d = 0.01 \Omega\text{-cm}^2$.

4.3.3 GaAs p/n Cell

If GaAs is used as a single-cell system, the photocurrent is $37.5 A/cm^2$ and the photon flux is $F = 2.34 \times 10^{20}/cm^2$. We assumed an average absorption coefficient of $5 \times 10^4/cm$. The bias potential is given by

$$\frac{qV_j}{kT} = \begin{cases} 43.96, & R_s A_d = 0 \\ 44.88, & R_s A_d = 0.01 \Omega\text{-cm}^2 \end{cases}$$

The results of the calculation are presented in Table 13.

TABLE 12. EXCESS CARRIER DENSITIES FOR SILICON n/p SOLAR CELLS

	R_sA_d (Ω-cm^2)	DIFFUSED REGION			BASE REGION		
		Doping Density (cm^{-3})	$\Delta n_n(0) = \Delta p_n(0)$	$\Delta n_n(x_j) = \Delta p_n(x_j)$	Doping Density (cm^{-3})	$\Delta p_p(x_j + W) = \Delta n_p(x_j + W)$ (cm^{-3})	$\Delta p_p(H) = \Delta n_p(H)$ (cm^{-3})
Si (used alone)	0	2×10^{19}	1.96×10^{15}	5.76×10^{13}	1×10^{17}	1.15×10^{16}	2.14×10^{15}
	0.01		2.39×10^{15}	5.00×10^{14}		9.98×10^{16}	1.85×10^{16}
Si (used with GaAs)	0		5.60×10^{14}	1.72×10^{13}		3.43×10^{15}	6.37×10^{14}
	0.01		5.69×10^{14}	2.70×10^{13}		5.38×10^{15}	9.99×10^{14}

TABLE 13. EXCESS CARRIER DENSITIES FOR GALLIUM ARSENIDE p/n SOLAR CELLS

DIFFUSED REGION				BASE REGION		
R_sA_d (Ω-cm^2)	Doping Density (cm^{-3})	$\Delta p_p(0) = \Delta n_p(0)$	$\Delta p_p(x_j) = \Delta n_p(x_j)$	Doping Density (cm^{-3})	$\Delta n_n(x_j + W) = \Delta p_n(x_j + W)$ (cm^{-3})	$\Delta n_n(H) = \Delta p_n(H)$ (cm^{-3})
0	2×10^{19}	2.62×10^{14}	4.27×10^{12}	2×10^{17}	4.27×10^{14}	0
0.01		2.68×10^{14}	1.07×10^{13}		1.07×10^{15}	0

Once again the maximum densities occur at the front of the diffused region and at the junction edge of the base region. (At the back of the base the excess carrier density is zero because we have assumed an infinite carrier recombination velocity.) In all cases, low-injection conditions appear to be valid.

4.4 EVALUATION OF MULTI-CELL SYSTEMS COMPOSED OF Ge, Si, GaAs, AND GaP SOLAR CELLS

The photocurrent density for Ge, Si, GaAs, and GaP cells was calculated for AM0 conditions, 1000 suns, and an operating temperature of 300K. Account was taken of losses due to grid shadowing, cell reflection, dichroic mirrors, and nonunity spectral response. One-, two-, three-, and four-cell configurations were evaluated. The output power of each of the cells was calculated and a total system efficiency was determined. In addition, the excess power which would have to be removed from the cells in order to maintain their 300K operating temperature was calculated.

The photocurrent density in the nth cell is given by

$$J_{ph} = S_n q \int_{E_1}^{E_2} SR(E)\, F(E)\, dE = S_n A_n q \int_{E_1}^{E_2} F(E)\, dE$$

where

$SR(E)$ = cell spectral response

S_n = structure factor which corrects for losses due to grid shadowing, cell reflection, and imperfect reflection and transmission by the dichroic mirrors

A_n = factor which corrects for losses due to nonunity spectral response over the band

q = electron charge

$F(E)$ = sunlight spectral distribution (1000 suns, AM0)

E_1 = cell energy bandgap

E_2 = upper limit of energy band falling on the nth cell

The structure factor can be written as

$$S_n = (1 - f_n)(1 - r_n)\, r_{m,n} \prod_{i=1}^{n-1} T_i$$

where

f_n = fraction of cell area covered by metal grid

r_n = cell front surface reflection coefficient

$r_{m,n}$ = average reflection coefficient of mirror which reflects energy to the nth cell

T_i = transmission of ith mirror

In order to eliminate series resistance effects, it was assumed that the metal grid would cover 10% of the cell so $f_n = 0.1$. With multiple layer antireflection coatings, cell reflectance can be reduced to 5% so $r_n = 0.05$. The dichroic mirrors can be designed to reflect all but about one percent of the band so $r_{m,n} = 0.99$. The percent of energy transmitted through the mirrors was taken to be 90%. (It was assumed that 5% of the out-of-band energy would be reflected instead of transmitted. Of the amount not

reflected, 2% would be absorbed and 3% would be scattered, resulting in a total loss of 10%.) The structure factors are listed in Table 14.

The spectral response factor can be written as

$$A_n = \int_{E_1}^{E_2} SR_n(E)\, F(E)\, dE \Big/ \int_{E_1}^{E_2} F(E)\, dE$$

The spectral response is given by

$$SR_n(E) = \frac{J_p + J_n + J_{dr}}{qF(1 - r_n)}$$

where J_p, J_n and J_{dr} are the photocurrents in the p-region, n-region, and depletion region respectively. For an n-on-p cell the photocurrents are given by[4]

TABLE 14. STRUCTURE FACTORS

	One-Cell System	Two-Cell System	Three-Cell System	Four-Cell System
First Cell	0.855	0.846	0.846	0.846
Second Cell		0.770	0.762	0.762
Third Cell			0.693	0.686
Fourth Cell				0.623

$$J_p = \left[\frac{qF(1-r)\alpha L_p}{(\alpha^2 L_p^{\,2} - 1)}\right]$$

$$\times \left[\frac{\left(\frac{S_p L_p}{D_p} + \alpha L_p\right) - \exp(-\alpha x_j)\left(\frac{S_p L_p}{D_p}\cosh\frac{x_j}{L_p} + \sinh\frac{x_j}{L_p}\right)}{\frac{S_p L_p}{D_p}\sinh\frac{x_j}{L_p} + \cosh\frac{x_j}{L_p}} - \alpha L_p \exp(-\alpha x_j)\right]$$

$$J_n = \frac{qF(1-r)\alpha L_n}{(\alpha^2 L_n^{\,2} - 1)} \exp\left[-\alpha(x_j + W)\right]$$

$$\times \left[\alpha L_n - \frac{\frac{S_n L_n}{D_n}\left(\cosh\frac{H'}{L_n} - \exp(-\alpha H')\right) + \sinh\frac{H'}{L_n} + \alpha L_n \exp(-\alpha H')}{\frac{S_n L_n}{D_n}\sinh\frac{H'}{L_n} + \cosh\frac{H'}{L_n}}\right]$$

$$J_{dr} = qF(1-r)\exp(-\alpha x_j)\left[1 - \exp(-\alpha W)\right].$$

For a p-on-n cell the subscripts are reversed. The device parameters are given in Table 15.

TABLE 15. DEVICE MODELING PARAMETERS

Parameters	Germanium (n on p, BSF)	Ref	Silicon (n on p, BSF)	Ref	Gallium Arsenide (p on n, GaAℓAs window)	Ref	Gallium Phosphide (n on p, BSF)	Ref
Junction depth (μm)	0.3	7	0.2	6	0.6	6	0.5	*
Surface recombination velocity, front (cm/s)	1×10^4	7	1×10^3	6	1×10^4	6	1×10^3	*
Surface recombination velocity, back (cm/s)	0		0	5	infinite	5	0	*
Doping, front (cm^{-3})	5×10^{18}	7	2×10^{19}	5	2×10^{19}	5	1×10^{19}	*
Doping, back (cm^{-3})	1×10^{17}	7	1×10^{17}	5	2×10^{17}	5	1×10^{17}	*
Lifetime, front (μs)	1	7	0.4	5	5×10^{-3}	5	1.5	8
Lifetime, back (μs)	10	7	20	5	5×10^{-2}	5	1.5	8
Cell Thickness (μm)	750	7	450	5	100	5	500	*
Energy Gap Parameters								
$E_g(0)$ (eV)	0.741	5	1.16	5	1.522	5	2.338	9
$E_g(300K)$ (eV)	0.66	5	1.12	5	1.43	5	2.24	5
α (10^{-4} K^{-1})	4.56	5	7.02	5	5.8	5	6.2	9
β (K)	210	5	1108	5	300	5	460	9
Relative Dielectric Constant	16	5	11.8	5	10.9	5	11	9
Mobility, front (cm^2/V-s)	164	7	75	5	1400	5	130	10
Mobility, back (cm^2/V-s)	2838	7	700	5	230	5	120	10

*Estimated from previous experience at Honeywell Corporate Technology Center.

[7] G.W. Masden and C.L. Backus, "Increased Photovoltaic Conversion Efficiency Through Use of Spectrum Splitting and Multiple Cells," Thirteenth IEEE Photovoltaic Specialists Conference, New York: IEEE Inc., 1978, p. 853.

[8] B. Hamilton and A.R. Peaker, "Deep-State-Controlled Minority-Carrier Lifetime in n-Type Gallium Phosphide," Journal of Applied Physics, Vol. 50, 1979, p. 6373.

[9] M. Neuberger, Handbook of Electronic Materials, Vol. 12, III-V Semiconducting Compounds, New York: IFI/Plenum, 1971, pp. 68, 70.

[10] R.J. Stirn, "Band Structure and Galvanomagnetic Effects in III-V Compounds with Indirect Band Gaps," Semiconductors and Semimetals, Vol. 8, Transport and Optical Phenomena, New York: Academic Press, Inc., 1972, pp. 47, 52.

There is little published data on either Ge or GaP as solar cell materials because by themselves they have rather low conversion efficiencies. Two papers discuss Ge as a solar cell.[7,11] GaP cell parameters were obtained from various sources.

The absorption coefficients α are plotted in Figure 46[†] and the calculated spectral responses are given in Figure 47. The absorption factors are

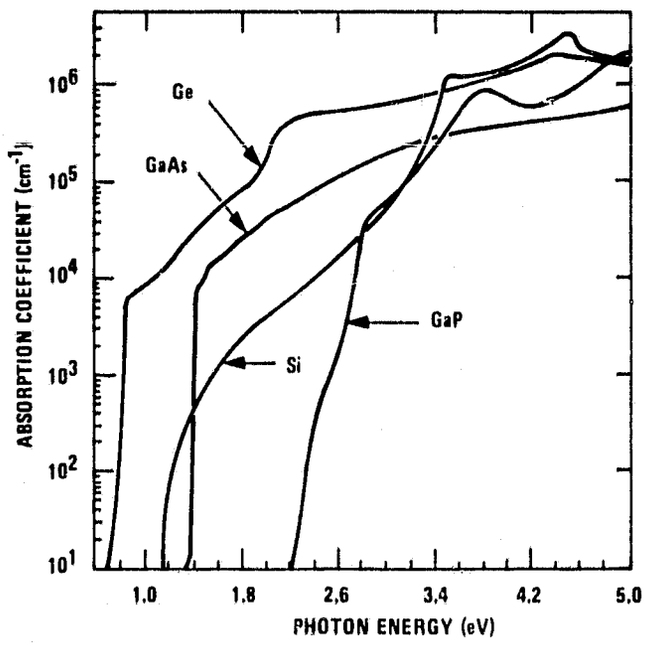

Figure 46. Intrinsic Absorption Coefficients of Ge, Si, GaAs, and GaP

[†]The curves for Ge, Si and GaAs are in Reference 4, page 10. For GaP the curve from 2.2 eV to 4.2 eV is based on data from S. Wemple, et al. From 4.2 eV to 6.4 eV it is based on data by H. Philipp and H. Ehrenreich.

[11]E.K. Kittl, M.D. Lammert, and R.J. Schwartz, "Performance of Ge P/N: Photovoltaic Cell at High Incident Radiation Intensity," 11th IEEE Photovoltaic Specialists Conference, Piscataway, New Jersey, 1975.

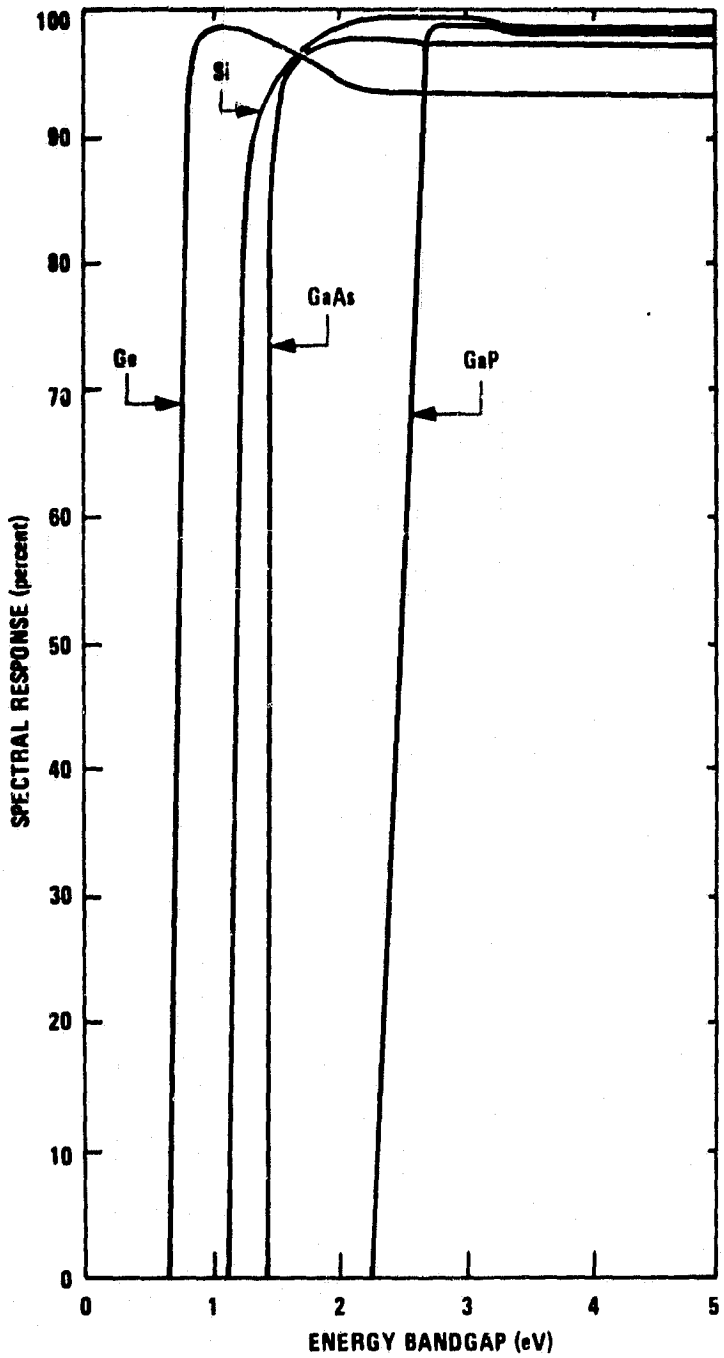

Figure 47. Calculated Spectral Responses of Ge, Si, GaAs, and GaP

given in matrix form in Table 16. The element at the top of the column denotes the cell, and the element in the left column denotes the other cell in the system which has the next highest energy bandgap. Hence, if Si and GaP are in the system and GaAs is not, the silicon cell will respond from 1.12 eV to 2.24 eV and its absorption factor will be 0.833.

Using the expressions given in subsection 4.1, the output power as a function of photocurrent was calculated for a p/n GaAs cell and n/p Ge, Si, and GaP cells. The intrinsic carrier concentrations were taken to be

$$n_i^2 = C\,T^3\,e^{-E_g/kT}$$

where

$$C = \begin{cases} 2.551 \times 10^{30}, & \text{Ge} \\ 4.81 \times 10^{31}, & \text{Si}^{9} \\ 2.57 \times 10^{29}, & \text{GaAs}^{9} \\ 3.844 \times 10^{31}, & \text{GaP} \end{cases}$$

TABLE 16. ABSORPTION FACTORS

Cell with Next Highest Energy Bandgap	Cell Material and Energy Bandgap			
	Ge (0.66 eV)	Si (1.12 eV)	GaAs (1.43 eV)	GaP (2.24 eV)
Si	0.942			
GaAs	0.918	0.614		
GaP	0.936	0.833	0.960	
No cell with higher energy bandgap	0.932	0.869	0.957	0.752

An operating temperature of 300K was assumed. The results are given in Figure 48.

The efficiency of the nth cell is

$$\eta_n = \text{Output Power/Input Power}$$

where the output power is determined by the photocurrent and the input power is $135.3 W/cm^2$. The system efficiency is

$$\eta = \sum_n \eta_n$$

Efficiencies of one-, two-, three-, and four-cell systems are given in Tables 17, 18, 19, and 20 respectively, for all possible combinations of Ge, Si, GaAs, and GaP. In determining the best configuration, several factors other than efficiency must be taken into account. They are:

- How many dichroic mirrors must be able to resist the high-energy (UV) photons; that is, how far down the stack is the highest energy bandgap material? The difficulty in fabricating a UV-resistant mirror was discussed in Section 3.
- On which cell are the long-wavelength photons (those not absorbed by the cells) dumped? This may result in additional heating, which will degrade the performance of the low-energy bandgap cells.
- Does the configuration contain solar cells which need to be developed; that is, Ge and/or GaP?

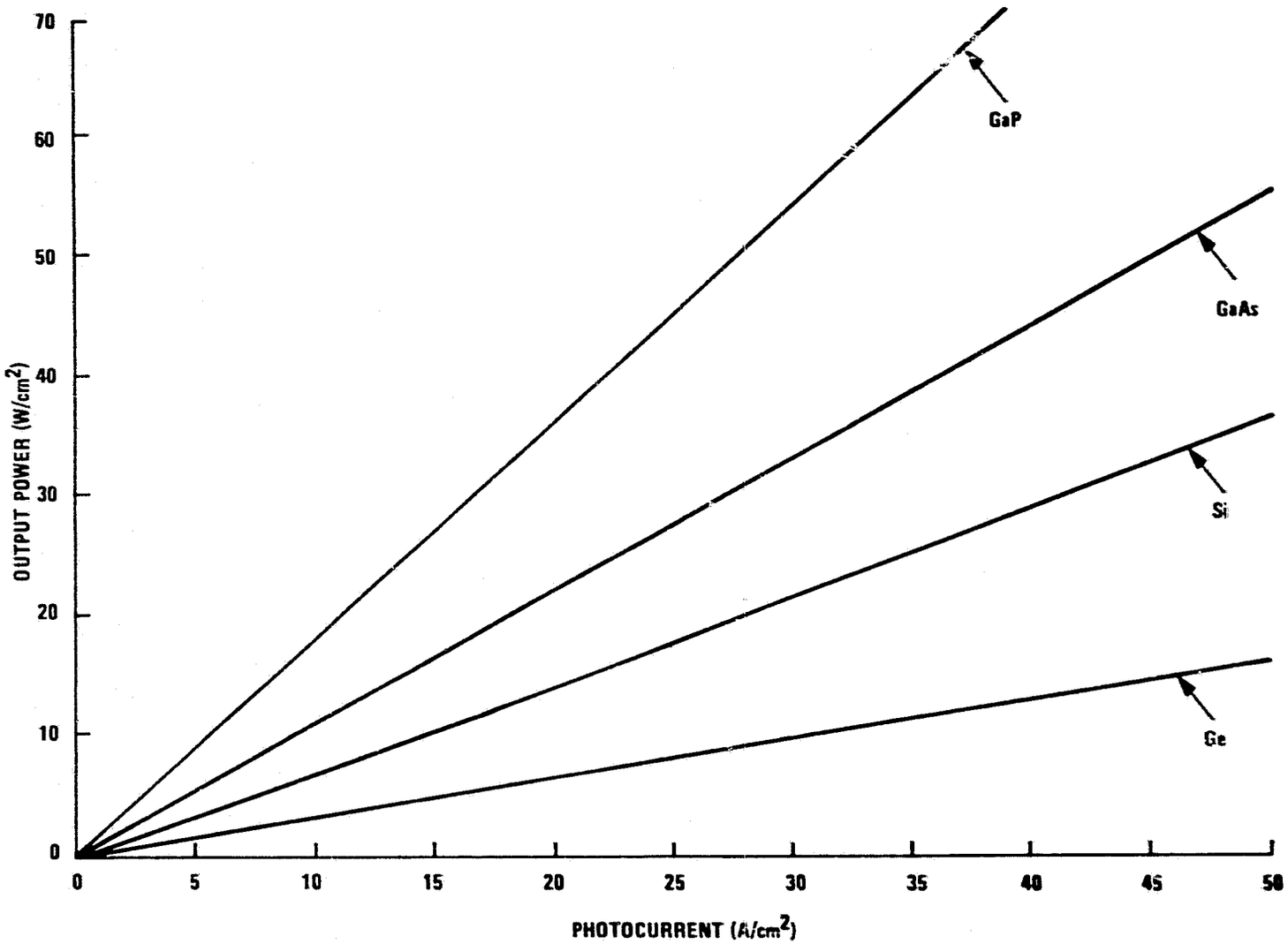

Figure 48. Output Power as a Function of Photocurrent for Ge, Si, GaAs, and GaP Solar Cells (T = 300K, $R_sA_d = 0$)

TABLE 17. RESULTS FOR ONE-CELL CONFIGURATIONS

Cell Configuration	Efficiency (percent)	Excess Power Absorbed in Cell (watts/cm^2)	Low Energy Power Not Absorbed (percent)	Disadvantages
GaAs	23.7	23.22	39.4	
Si	21.4	30.52	25.4	• Large amount of excess energy
Ge	14.8	57.53	7.6	• Ge development • Large amount of excess energy
GaP	11.8	5.56	70.4	• GaP development

TABLE 18. RESULTS FOR TWO-CELL CONFIGURATIONS

Cell Configuration	Efficiencies (percent)	Excess Power Absorbed in Cells (watts/cm^2)	Low Energy Power Not Absorbed (percent)	Disadvantages
GaAs Ge	24.8 7.0 31.8	23.0 10.6 33.6	10.3	• Ge development • Large amount excess energy in Ge • Long λ energy on Ge
Ge GaAs	7.8 22.5 30.3	11.6 20.9 32.5	10.3	• Ge development • Large amount excess energy in Ge
GaAs Si	24.8 3.6 28.4	23.0 0.5 23.5	34.3	• Long λ energy on Si
Si GaAs	4.1 22.5 26.6	0.6 20.9 21.5	34.3	
GaAs GaP	15.5 10.7 26.2	6.82 5.0 11.82	53.3	• GaP development
GaP GaAs	11.8 14.0 25.8	5.5 6.2 11.7	53.3	• GaP development
Si Ge	21.1 4.4 25.5	30.2 4.7 34.9	10.3	• Ge development • Large amount excess energy in Si • Long λ energy on Ge
Si GaP	14.6 10.7 25.3	11.8 5.0 16.8	34.3	• GaP development • Large amount excess energy in Si
GaP Si	11.8 13.3 25.1	5.5 10.7 17.2	34.3	• GaP development • Large amount excess energy in Si • Long λ energy on Si

TABLE 18. RESULTS FOR TWO-CELL CONFIGURATIONS (concluded)

Cell Configuration	Efficiencies (percent)	Excess Power Absorbed in Cells (watts/cm^2)	Low Energy Power Not Absorbed (percent)	Disadvantages
Ge Si	5.0 19.2 24.2	5.2 27.5 32.7	10.3	• Ge development • Large amount excess energy in Si
Ge GaP	12.7 10.7 23.4	32.8 5.0 37.8	10.3	• Ge and GaP development • Large amount excess energy in Ge
GaP Ge	11.8 11.5 23.3	5.5 29.9 35.4	10.3	• Ge and GaP development • Large amount excess energy in Ge • Long λ energy on Ge

TABLE 19. RESULTS FOR THREE-CELL CONFIGURATIONS

Cell Configuration	Efficiencies (percent)	Excess Power Absorbed in Cells (watts/cm^2)	Low Energy Power Not Absorbed (percent)	Disadvantages
GaAs Si Ge	24.8 3.7 4.1 32.6	23.0 0.5 4.2 27.7	10.3	• Long λ energy on Ge • Large amount excess energy in GaAs
GaAs GaP Ge	15.5 10.7 6.4 32.6	6.8 5.0 9.5 21.3	10.3	• Ge and GaP development • Two UV resistant mirrors • Large amount excess energy in Ge • Long λ energy on Ge
GaAs Ge Si	24.8 4.4 3.3 32.5	23.0 4.7 0.5 28.2	10.3	• Long λ energy on Si • Large amount excess energy in GaAs
GaP GaAs Ge	11.8 14.0 6.4 32.2	5.5 6.1 9.5 21.1	10.3	• Ge and GaP development • Large amount excess energy in Ge • Long λ energy on Ge
GaAs Ge GaP	15.5 7.0 9.6 32.1	6.8 10.5 4.5 21.8	10.3	• Ge and GaP development • Two UV resistant mirrors • Large amount excess energy in Ge
GaP Ge GaAs	11.8 7.0 12.6 31.4	5.5 10.5 5.6 21.6	10.3	• Ge and GaP development • Large amount excess energy in Ge
Ge GaAs GaP	7.8 14.0 9.6 31.4	11.6 6.1 4.5 22.2	10.3	• Ge and GaP development • Two UV resistant mirrors • Large amount excess energy in Ge

TABLE 19. RESULTS FOR THREE-CELL CONFIGURATIONS (continued)

Cell Configuration	Efficiencies (percent)	Excess Power Absorbed in Cells (watts/cm^2)	Low Energy Power Not Absorbed (percent)	Disadvantages
Ge GaP GaAs	7.8 10.7 12.6 31.1	11.6 5.0 5.6 22.2	10.3	• Ge and GaP development • Two UV resistant mirrors • Large amount excess energy in Ge
Ge GaAs Si	5.0 22.2 3.3 30.5	5.2 20.7 0.5 26.4	10.3	• Two UV resistant mirrors • Large amount excess energy in GaAs • Long λ energy on Si
Si GaAs Ge	4.1 22.2 4.1 30.4	0.6 20.7 4.2 25.5	10.3	• Two UV resistant mirrors • Large amount excess energy in GaAs • Long λ energy on Ge
GaAs GaP Si	15.5 10.7 3.3 29.5	6.8 5.0 0.5 12.3	34.3	• Two UV resistant mirrors • Long λ energy on Si
Si GaP Ge	14.6 10.7 4.1 29.4	11.8 5.0 4.2 21.0	10.3	• Ge and GaP development • Two UV resistant mirrors • Large amount excess energy in Si • Long λ energy on Ge
GaP Si Ge	11.8 13.3 4.1 29.2	5.5 10.6 4.2 20.3	10.3	• Ge and GaP development • Large amount excess energy in Si • Long λ energy on Ge
GaP GaAs Si	11.8 14.0 3.3 29.1	5.5 6.1 0.5 12.1	34.3	• Long λ energy on Si

TABLE 19. RESULTS FOR THREE-CELL CONFIGURATIONS (continued)

Cell Configuration	Efficiencies (percent)	Excess Power Absorbed in Cells (watts/cm^2)	Low Energy Power Not Absorbed (percent)	Disadvantages
Ge Si GaAs	5.0 3.7 20.3 29.0	5.2 0.5 18.8 24.5	10.3	• Two UV resistant mirrors • Large amount excess energy in GaAs
Si Ge GaAs	4.1 4.4 20.3 28.8	0.6 4.7 18.8 24.1	10.3	• Two UV resistant mirrors • Large amount excess energy in GaAs
GaAs Si GaP	15.5 3.7 9.6 28.8	6.8 0.5 4.5 11.8	34.3	• Two UV resistant mirrors
Si Ge GaP	14.6 4.4 9.6 28.6	11.8 4.7 4.5 21.0	10.[illegible]	• Ge and GaP development • Two UV resistant mirrors • Large amount excess energy in Si
GaP Si GaAs	11.8 3.7 12.6 28.1	5.5 0.5 5.6 11.6	34.3	
GaP Ge Si	11.8 4.4 11.9 28.1	5.5 4.7 9.7 19.9	10.3	• Ge and GaP development • Long λ energy on Si
Ge Si GaP	5.0 13.3 9.6 27.9	5.2 10.6 4.5 20.3	10.3	• Ge and GaP development • Two UV resistant mirrors • Large amount excess energy in Si

TABLE 19. RESULTS FOR THREE-CELL CONFIGURATIONS (concluded)

Cell Configuration	Efficiencies (percent)	Excess Power Absorbed in Cells (watts/cm^2)	Low Energy Power Not Absorbed (percent)	
Si GaAs GaP	4.1 14.0 9.6 27.7	0.6 6.1 4.5 11.2	34.3	• Two UV resistant mirrors
Ge GaP Si	5.0 10.7 11.9 27.6	5.2 5.0 9.7 19.9	10.3	• Ge and GaP development • Two UV resistant mirrors • Large amount excess energy in Si • Long λ energy on Si
Si GaP GaAs	4.1 10.7 12.7 27.4	0.6 5.0 5.6 11.2	34.3	• Two UV resistant mirrors

TABLE 20. RESULTS FOR FOUR-CELL CONFIGURATIONS

Cell Configuration	Efficiencies (percent)	Excess Power Absorbed in Cells (watts/cm^2)	Low Energy Power Not Absorbed (percent)	Disadvantages
GaAs GaP Ge Si	15.5 10.7 4.1 3.0 33.3	6.8 5.0 4.2 0.4 16.4	10.3	• 2 UV-resistant mirrors • Long λ energy on Si
GaAs GaP Si Ge	15.5 10.7 3.3 3.7 33.2	6.8 5.0 0.4 3.8 16.0	10.3	• 2 UV-resistant mirrors • Long λ energy on Ge
GaP GaAs Ge Si	11.8 14.0 4.1 3.0 32.9	5.5 6.1 4.2 0.4 16.2	10.3	• Long λ energy on Si
GaP GaAs Si Ge	11.8 14.0 3.3 3.7 32.8	5.5 6.1 0.4 3.8 15.8	10.3	• Long λ energy on Ge
GaAs Si GaP Ge	15.5 3.7 9.5 3.7 32.4	6.8 0.5 4.5 3.8 15.6	10.3	• 3 UV-resistant mirrors • Long λ energy on Ge
GaAs Ge GaP Si	15.5 4.4 9.5 3.0 32.4	6.8 4.7 4.5 0.4 16.4	10.3	• 3 UV-resistant mirrors • Long λ energy on Si

TABLE 20. RESULTS FOR FOUR-CELL CONFIGURATIONS (continued)

Cell Configuration	Efficiencies (percent)	Excess Power Absorbed in Cells (watts/cm^2)	Low Energy Power Not Absorbed (percent)	Disadvantages
GaAs	15.5	6.8	10.3	• 3 UV-resistant mirrors
Si	3.7	0.5		
Ge	4.1	4.2		
GaP	8.6	4.0		
	31.9	15.5		
GaP	11.8	5.5	10.3	• Long λ energy on Ge
Si	3.7	0.5		
GaAs	12.6	5.5		
Ge	3.7	3.8		
	31.8	15.3		
GaP	11.8	5.5	10.3	• Long λ energy on Si
Ge	4.4	4.7		
GaAs	12.6	5.5		
Si	3.0	0.4		
	31.8	16.1		
GaAs	15.5	6.8	10.3	• 3 UV-resistant mirrors
Ge	4.4	4.7		
Si	3.3	0.4		
GaP	8.6	4.0		
	31.8	15.9		
Ge	5.0	5.2	10.3	• 3 UV-resistant mirrors
GaAs	14.0	6.1		• Long λ energy on Si
GaP	9.5	4.5		
Si	3.0	0.4		
	31.5	16.2		
Ge	5.0	5.2	10.3	• 2 UV-resistant mirrors
GaP	10.7	5.0		• Long λ energy on Si
GaAs	12.6	5.5		
Si	3.0	0.4		
	31.3	16.1		

TABLE 20. RESULTS FOR FOUR-CELL CONFIGURATIONS (continued)

Cell Configuration	Efficiencies (percent)	Excess Power Absorbed in Cells (watts/cm^2)	Low Energy Power Not Absorbed (percent)	Disadvantages
Si	4.1	0.6	10.3	• 3 UV-resistant mirrors
GaAs	14.0	6.1		• Long λ energy on Ge
GaP	9.5	4.5		
	3.7	3.8		
Ge	31.3	15.0		
GaP	11.8	5.5	10.3	
Si	3.7	0.5		
Ge	4.1	4.2		
	11.5	5.0		
GaAs	31.1	15.2		
Si	4.1	0.6	10.3	• 2 UV-resistant mirrors
GaP	10.7	5.0		• Long λ energy on Ge
GaAs	12.6	5.5		
	3.7	3.8		
Ge	31.1	14.9		
GaP	11.8	5.5	10.3	
Ge	4.4	4.7		
Si	3.3	0.4		
	11.5	5.0		
GaAs	31.0	15.6		
Ge	5.0	5.2	10.3	• 3 UV-resistant mirrors
GaAs	14.0	6.1		
Si	3.3	0.4		
	8.6	4.0		
GaP	30.9	15.7		
Si	4.1	0.6	10.3	• 3 UV-resistant mirrors
GaAs	14.0	6.1		
Ge	4.1	4.2		
	8.6	4.0		
GaP	30.8	14.9		

TABLE 20. RESULTS FOR FOUR-CELL CONFIGURATIONS (concluded)

Cell Configuration	Efficiencies (percent)	Excess Power Absorbed in Cells (watts/cm^2)	Low Energy Power Not Absorbed (percent)	Disadvantages
Ge	5.0	5.2	10.3	• 2 UV-resistant mirrors
GaP	10.7	5.0		
Si	3.3	0.4		
	11.5	5.0		
GaAs	30.5	15.6		
Si	4.1	0.6	10.3	• 2 UV-resistant mirrors
GaP	10.7	5.0		
Ge	4.1	4.2		
	11.5	5.0		
GaAs	30.4	14.8		
Ge	5.0	5.2	10.3	• 3 UV-resistant mirrors
Si	3.7	0.5		
GaAs	12.6	5.5		
	8.6	4.0		
GaP	29.9	15.2		
Si	4.1	0.6	10.3	• 3 UV-resistant mirrors
Ge	4.4	4.7		
GaAs	12.6	5.5		
	8.6	4.0		
GaP	29.7	14.8		
Ge	5.0	5.2	10.3	• 3 UV-resistant mirrors
Si	3.7	0.5		
GaP	9.5	4.5		
	11.5	5.0		
GaAs	29.7	15.2		
Si	4.1	0.6	10.3	• 3 UV-resistant mirrors
Ge	4.4	4.7		
GaP	9.5	4.5		
	11.5	5.0		
GaAs	29.5	14.8		

- How much extra power is absorbed by the cell because of the mismatch between photon energy and the cell energy bandgap? This power must be removed.

These disadvantages, where applicable, are noted in the tables.

The excess power absorbed by the nth cell is given by

$$P_{heat} = S_n \int_{E_1}^{E_2} SR(E)\, F(E)(E - E_g)\, dE \approx S_n A_n \int_{E_1}^{E_2} F(E)(E - E_g)\, dE$$

These values are listed in the tables. The 5% out-of-band photons, reflected by the mirrors, may also contribute a small amount to this power but this effect was not included.

The percent of power not absorbed because the photon energy is less than the bandgap of any cell in the system is given by

$$\text{fraction of power not absorbed} = \int_0^{\text{lowest } E_g} F(E)\, E dE \Big/ \int_0^{\infty} F(E)\, E dE$$

These values are also listed in the tables.

For a one-cell system, GaAs has the highest efficiency (23.7%) and requires the least excess heat removal (23.22W/cm^2). Si has an efficiency of 21.4% and requires more excess heat removal (30.52W/cm^2). Ge and GaP have much lower efficiencies and also are not presently available as well-developed solar cells.

For a two-cell system, the highest efficiencies are obtained with the combinations GaAs/Ge (31.8%), Ge/GaAs (30.3%), GaAs/Si (28.4%), and Si/GaAs (26.6%). All other combinations have lower efficiencies and require the development of one or two new solar cells. Within the two GaAs-Ge systems and within the two GaAs-Si systems, the slightly higher efficiency configurations (those with GaAs as the first cell) have slightly larger excess heat removal requirements and also require that the long-wavelength energy fall on the smaller energy bandgap materials. The effect of this long-wavelength energy falling on a solar cell depends on the back metal contact and the structure beneath it because they will determine how much of this energy is absorbed by the system. Hence, the tradeoff between the two configurations with the same materials must be done at the system level. The main difference between the GaAs-Ge systems and the GaAs-Si systems is that the former require development of a new solar cell. Hence, the cost of this development must be traded off against the potential 3.5% increase in efficiency. Also, the excess power in the GaAs-Ge systems ($\sim 33 W/cm^2$) is much larger than that in the GaAs-Si systems ($\sim 22.5 W/cm^2$). This heat removal tradeoff is considered in Section 5.

A comparison of the one- and two-cell systems shows that a GaAs-Ge system would have an efficiency 1.28 to 1.34 times that of a GaAs system. However, the excess power removal requirement is 1.40 to 1.45 times as large. The GaAs-Si systems would have an efficiency 1.12 to 1.20 times that of a GaAs system, with an excess power removal requirement 0.93 to 1.01 times as large.

For a three-cell system, many of the highest efficiencies (31.1 to 32.6%) can be obtained with the Ge-GaAs-GaP systems. The excess power removal requirements are 21.1 to 22.2W/cm^2. However, these require the development of two new solar cells. This development is also required for the Ge-Si-GaP systems, which have efficiencies from 27.6 to 29.4% and excess power removal requirements of 19.9 to 21.0W/cm^2. There appears to be no clear advantage of any of these systems over the Ge-Si-GaAs systems or the Si-GaAs-GaP systems. The Ge-Si-GaAs systems have efficiencies from 28.8 to 32.6% and excess power removal requirements of 24.1 to 28.2W/cm^2. The Si-GaAs-GaP systems have efficiencies from 27.4 to 29.5% and excess power removal requirements of 11.2 to 12.3W/cm^2. Hence, a tradeoff must be made between efficiency and power removal. Also, a comparison of the cost and potential quality of solar cells made from Ge and GaP must be considered.

The best of the Ge-Si-GaAs systems are GaAs/Si/Ge and GaAs/Ge/Si. They have the highest efficiencies (32.5 and 32.6%) and require only one UV-resistant mirror. Their disadvantage is that the long-wavelength radiation falls on the smaller energy bandgap cells. In order to avoid this, Ge/Si/GaAs or Si/Ge/GaAs configurations with efficiencies of 28.8 and 29% could be chosen. Their excess power requirements (29W/cm^2) are essentially the same but they do require two UV-resistant mirrors.

The Si-GaAs-GaP systems which do not require two UV-resistant mirrors are GaP/GaAs/Si and GaP/Si/GaAs, with efficiencies of 29.1 and 28.1, respectively. The latter case has the advantage of long-wavelength energy falling on the GaAs. The GaAs/GaP/Si system has the highest efficiency (29.5%) but requires two UV-resistant mirrors and also has the long-wavelength energy falling on the Si cell.

A comparison of two-cell and three-cell systems results in some obvious tradeoffs. If Ge can be developed as a high-quality solar cell, a two-cell system of Ge-GaAs has almost as high an efficiency as a three-cell system of Ge-Si-GaAs. However, the power removal requirement is 1.4 times as great. If a high performance Ge solar cell cannot be made, the tradeoff is then between a GaAs/Si system with an efficiency of 28.4% and a GaAs/GaP/Si system with an efficiency of 29.5%.

All the four-cell systems require development of two new solar cells. The possible efficiencies are from 29.5 to 33.3% and the excess power removal requirements are from 14.8 to 16.4W/cm^2. All but six configurations (those with GaP as the first cell) require two UV-resistant mirrors. Two of these configurations have the long-wavelength energy falling on the GaAs cell. Their efficiencies are 31.0 and 31.1% and their excess power removal requirements are 15.2 and 15.6W/cm^2. The main advantage of a four-cell system over a three-cell Ge-Si-GaAs system is that the excess power removal requirement is essentially cut in half. The main disadvantage is the required development of two new solar cells.

All of the above systems are compared in the tradeoff analysis in Section 5. The tradeoff factors are:

- Efficiency
- Development of new solar cells
- Excess heat removal
- Effect of long-wavelength energy falling on a small-energy bandgap solar cell

- Number of UV-resistant mirrors
- Additional structures required for additional cells
- Potential performance of Ge and GaP
- Required solar cell area

SECTION 5

SYSTEM TRADE-OFF ANALYSIS

A trade-off analysis was performed to determine the most cost-effective optical and solar-cell/beam-splitter system. The primary mirror focal length was restricted to $f_1/D_1 \geq 0.7$ in order to control surface accuracies. Four-cell systems were not included in the tradeoff analysis because they were shown to be less cost-effective than three-cell systems.

Cost estimates were made for the optics, solar cells, and beam splitters. It was found that the smallest cost per peak watt would be obtained with an optical system composed of an f/0.7 primary mirror and a system f-number of f/3.5. The solar cell system chosen was GaAs/Si although a GaAs/Ge system has the potential of a slightly smaller cost per peak watt if the cost of solar cell development is not prohibitive.

5.1 LIMITS ON SYSTEM PARAMETERS

The primary mirror focal length cannot be smaller than $f_1/D_1 = 0.7$, as discussed in Section 2.

The four-cell systems were not included in the system level trade-off analysis because their efficiencies were not much better than those of the three-cell systems and excess power removal requirements had little effect on overall system cost. Also, four-cell systems require the development of two new solar cells.

In order to avoid damage to the beam splitters due to excessive heating, their temperature must be kept below 350°C. The power absorbed by the beam splitters can be expressed in terms of their temperature by:

$$P_{absorbed} = P_{bs}\alpha_{bs}A_{bs} = \sigma\,\epsilon\,(T_{bs}^{4} - T_{o}^{4})\,A_{bs}$$

where

P_{bs} = power per unit area incident on the beam splitters

α_{bs} = fraction of incident power absorbed by the beam splitters

= 0.02 (as discussed in Section 4)

A_{bs} = beam splitter area (defined in Section 2)

σ = 5.67×10^{-12} W/cm^2-K

ϵ = beam-splitter emissivity

= 0.5

T_{bs} = beam-splitter temperature

$\leq$ 350°C = 623K

T_o = environmental temperature

= 300K

This equation requires that P_{bs} be less than 2.02×10^5 W/m^2. The power incident on the beam splitters is given by:

$$P_{bs}A_{bs} = P_{in}\,\pi\,(D_1/2)^2\,\epsilon_{Cass}\,\epsilon_{OBS}C$$

where

P_{in} = incident solar power density

= $1353 W/m^2$

$\pi(D_1/2)^2$ = primary mirror area

ϵ_{Cass} = collector efficiency

= 0.90

ϵ_{OBS} = fraction of power not obscured by the secondary mirror

= $(1 - (D_2/D_1)^2)$

C = fraction of radiation passed by preceding mirrors ≤ 1

In order to keep the beam-splitter temperature below 350°C we must have

$$P_{bs} \leq 2.02 \times 10^5 W/m^2$$

so

$$\frac{A_{bs}}{D_1^2} \geq (1 - (D_2/D_1)^2)\ (4.73 \times 10^{-3})C$$

The righthand side of this equation for the worst case C = 1, is plotted in Figure 49 as a function of system f-number and primary focal length. The actual beam-splitter areas, which were plotted in Figure 8, are larger than 0.006 so the beam splitter temperatures will be less than 350°C.

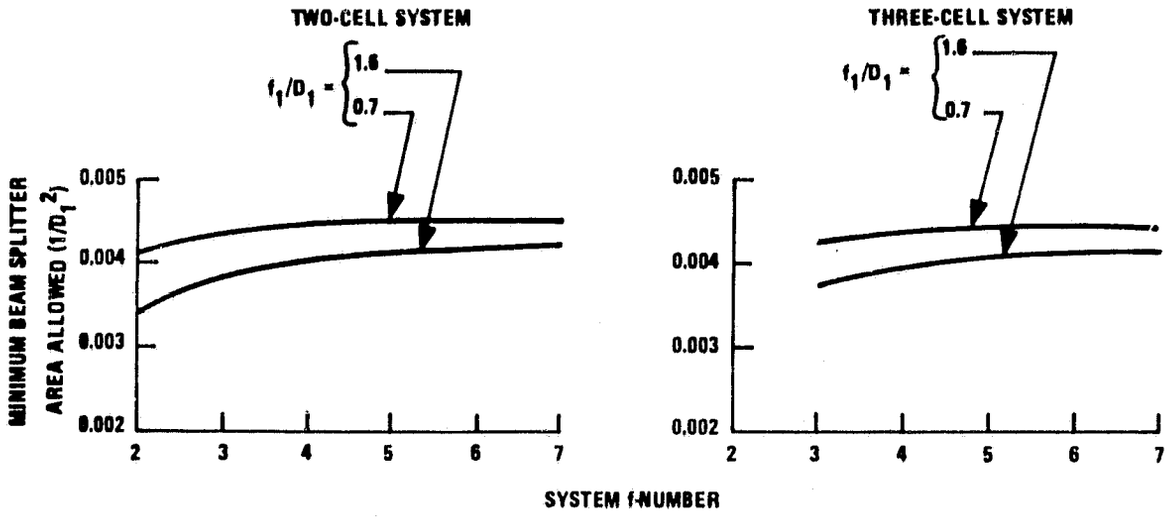

Figure 49. Minimum Beam-Splitter Areas Allowed for $T_{bs} \leq 350°C$

In order to avoid performance degradation in the solar cells, their temperature must be kept low. For our analysis we have assumed that the solar cells are held at a temperature of 300K. The excess power in the solar cells can be removed by means of a radiator at a temperature of 290K. A discussion of this means of removing the excess power is presented in Section 6. The excess power to be dissipated by the radiator is:

$$P = P_{excess} A_{sc} = \sigma \epsilon (T_{rad}^4 - T_{space}^4) A_{rad}$$

where

P_{excess} = excess power per unit area absorbed in the solar cells (given in Tables 17, 18, and 19)

A_{sc} = solar cell array area

ϵ = radiator emissivity = 1

T_{rad} = radiator temperature = 290K

T_{space} = space temperature $\approx$ 0 K

A_{rad} = radiator area

Hence the required radiator area depends on the solar cell array areas and the excess power absorbed in the solar cells.

5.2 COMPONENT COST ESTIMATES

It was assumed that the cost of each of the components was proportional to its area. Since each of the areas has been shown to be proportional to the area of the primary mirror, we chose to express all costs in the units of $1/D_1^2$ where D_1 is in meters. The normalized cost of the primary mirror was taken to be

$$C_{PM} = \frac{\pi}{4} \quad c_{PM}$$

where

c_{PM} = cost per unit area of the primary mirror

= $\$600/m^2$

It is assumed that the cost of mounting all of the components is included in the cost per unit area, which we have stated.

In 1977 Honeywell estimated a cost of $\$420/m^2$ for the Solar-Powered Deep-Well Irrigation Facility Report,[12] which used primary collectors of approximately the same size as required for this program. Meinel[13] recently discussed the cost of the "Next Generation Telescope," for which a 25-meter aperture and surface accuracy comparable to that required for this program has an estimated cost of $\$407/m^2$. For the cost of the primary mirror we estimated $\$400/m^2$ and $\$200/m^2$ for the mount. This cost per unit area is consistent with previous estimates for collector costs. In 1978 H.A. Wilkening[14] quoted a cost of $\$10/ft^2 = \$108/m^2$. In 1976 S.W. Zehr[15] quoted a cost of $\$50$ to $\$150/m^2$ for tracking concentrators. In 1980$ D.C. Schueler[16] estimated that reliable concentrators should have an installed cost in the $\$200$ to $\$300/m^2$ range.

---

[12] "150 kWe Solar-Powered Deep-Well Irrigation Facility," Final Report to ERDA, Contract # EG-77-C-04-3918, Honeywell Energy Resources Center Minneapolis, Minnesota, August 31, 1977.

[13] A.B. Meinel, "Cost-Scaling Laws Applicable to Very Large Optical Telescopes," Optical Engineering, Vol. 18, No. 6, November-December, 1979, pp. 645-647.

[14] H.A. Wilkening, "Design of a 10 kW Photovoltaic 200/1 Concentrator," 13th IEEE Photovoltaic Specialists Conference, Piscataway, New Jersey, 1978, pp. 669-672.

[15] S.W. Zehr, "High Efficiency Multijunction Concentrator Solar Cells," Report No. RS 8313/203, Sandia Laboratories, Albuquerque, New Mexico, 1976, p. 29.

[16] D.G. Schueler, "Status of Photovoltaic Concentrator Development," Proceedings of the Photovoltaics Advanced R&D Annual Review Meeting, Solar Energy Research Institute, Golden, Colorado, 1979, pp. 325-327.

The normalized cost of the secondary mirror was taken to be:

$$C_{SM} = \frac{\pi}{4} (D_2/D_1)^2 (\Delta m_1°/\Delta m_2°) c_{PM}$$

where $\Delta m_1°$ and $\Delta m_2°$ are slope errors associated with the surface profiles of the primary and secondary mirrors, respectively. Their ratio is discussed in subsection 2.3.

The normalized cost of each CPC was taken to be:

$$C_{CPC} = (A_{CPC}/D_1^2) c_{CPC}$$

where

$$c_{CPC} = \$2100/m^2$$

The cost of the CPC is larger than that for the collector because of its unusual shape, which is more difficult to fabricate.

The normalized cost of the radiator was taken to be:

$$C_{rad} = (A_{rad}/D_1^2) c_{rad}$$

where

$$c_{rad} = \$200/m^2$$

This cost estimate is discussed in Section 6. The normalized cost of each of the beam splitters was taken to be:

$$C_{bs} = (A_{bs}/D_1^2) c_{bs}$$

where

$$c_{bs} = \$3500/m^2$$

The normalized cost of each of the solar cell arrays was taken to be:

$$C_{sc} = (A_{sc}/D_1^{\ 2})\, c_{sc}$$

where

$$c_{sc} = \$5000/m^2$$

The same cost was used for all the solar cell arrays because their cost is very small compared to the other components of the system and their actual costs will be the same within a factor of two or less. Kim Mitchell, who is in charge of the Advanced Concentrator Concepts Programs at the Solar Energy Research Institute, was consulted regarding the current price of Si and GaAs solar cells. The cost for silicon substrates is $\$0.90/in.^2$ = $\$1395/m^2$. A factor of about four is used to include the processing cost, giving a cost per unit area for Si cells of $\$5580/m^2$. This is slightly higher than the amount estimated by S.W. Zehr[15] of $\$3000/m^2$ in 1976$, which would be about $\$5000/m^2$ in 1980$. H.A. Wilkening[14] in 1978 estimated a Si cell cost of $3094 for a collector area of 1600 ft^2 and a concentration ratio of 200. This gives a cost per unit area for Si cells of $\$4163/m^2$. Hence, our assumption of $\$5000/m^2$ is reasonable.

The cost for GaAs substrates is $\$22/in.^2$ = $\$34,100/m^2$. Assuming that the cost of processing is the same as that for Si, the cost for GaAs cells is $\$38,285/m^2$. One method for reducing this cost is to use a silicon substrate and deposit $GaP\text{-}GaP_{1-x}\text{-}GaAs_x\text{-}GaAs$ by gradually varying the

relative amounts of GaAs and GaP. This method is possible because of the good lattice match of Si and GaP. Hence, GaAs cells could be produced for approximately the same cost as Si cells. This amount is consistent with Ron Bell's estimate* (Varian Associates) of $3000/m^2$ in 1976$ for production quantities of GaAs solar cells. In 1980$ this is also about $5000/m^2$.

The same argument can be used for GaP cells if the cost of developing a new solar cell, addressed in subsection 5.5, is excluded. Although GaP is much more costly than Si, GaP can be deposited on Si and hence the cost of a GaP solar cell is approximately the same as that of a Si solar cell.

Germanium costs about three times as much as Si. If the cost of developing a new solar cell is excluded and the processing costs are assumed to be the same as those for Si, the cost of Ge cells will be 1.5 times that of Si cells, or $7500.

The cost of the system is computed as a sum of the costs of the primary mirror, secondary mirror, beam splitters, CPCs, solar cell arrays, and radiator area required to keep the solar cell arrays at a temperature of 300K. An N-cell system has a normalized cost of:

$$C = \frac{\pi}{4} c_{PM} + \frac{\pi}{4} (D_2/D_1)^2 (\Delta m_1{}^\circ/\Delta m_2{}^\circ) c_{PM} + \sum_{n=2}^{N} (A_{bs}/D_1{}^2)_n c_{bs}$$

$$+ \sum_{n=1}^{N} (A_{CPC}/D_1{}^2) c_{CPC} + \sum_{n=1}^{N} (A_{sc} c_{sc})_n$$

$$+ (A_{rad}/D_1{}^2) c_{rad}$$

*Personal Communication, January 1980.

5.3 SELECTION OF AN OPTICAL SYSTEM

The most cost-effective optical system was selected by computing the cost per peak watt of each system. It is given by:

$$\text{COST} = C \Big/ (P_{out}/D_1^{\,2})$$

where C is the system cost divided by $D_1^{\,2}$. For a given number of cells the only dependence of COST on the particular solar cells used is in the radiator cost term in C and the fact that P_{out} is proportional to the solar-cell/beam-splitter efficiency η. Since the radiator cost is only about ten percent of the system cost, a radiator cost based on an average value of the excess power to be removed from the solar cells can be used to compare the various optical systems. Since COST is proportional to $1/\eta$, the choice of optical systems is independent of η for a given number of cells. For our comparison we used:

$$P_{excess} = 20\text{W/cm}^2$$

$$\eta = 30\%$$

This value of η is low for the best two- and three-cell systems, which have efficiencies as high as 32.6%; and high for the best one-cell system, which has an efficiency of 23.7%. Hence, in the following comparison the cost per peak watt of the one-cell systems should not be compared with those of the two- and three-cell systems. An optimum optical system is chosen for each of the three sets of systems. In the next subsection the actual values of η and P_{excess} are used to determine the most cost-effective system.

The output power and cost are assumed to be proportional to the area of the primary mirror. Hence, the cost per peak watt can be minimized independent of the square of the primary mirror diameter, D_1^2.

The output power per D_1^2 is:

$$P_{out}/D_1^2 = \frac{\pi}{4} \epsilon_{Cass} \epsilon_{CPC} \epsilon_{sc} \epsilon_{OBS} H_{in}$$

where

$$\epsilon_{Cass} = 0.9$$

$$\epsilon_{CPC} = 0.95$$

$$\eta = \epsilon_{bs} \epsilon_{sc} = \text{solar-cell/beam-splitter efficiency}$$

$$\epsilon_{OBS} = (1 - (D_2/D_1)^2)$$

$$H_{in} = 1353 W/m^2 \text{ (1000 suns, AM0)}$$

P_{out}/D_1^2 is plotted in Figure 50 as a function of system f-number for various values of the primary mirror focal length, f_1. The system efficiency is taken to be 30%. The dependence of the output power on obscuration efficiency (see Figure 12) is evident. For all systems the output power is largest for low primary mirror focal lengths and large system f-numbers. For a one-cell system the output power appears to be higher than that of the two- and three-cell systems. However, this is because we have used too large an efficiency. The correct efficiency would lower these curves.

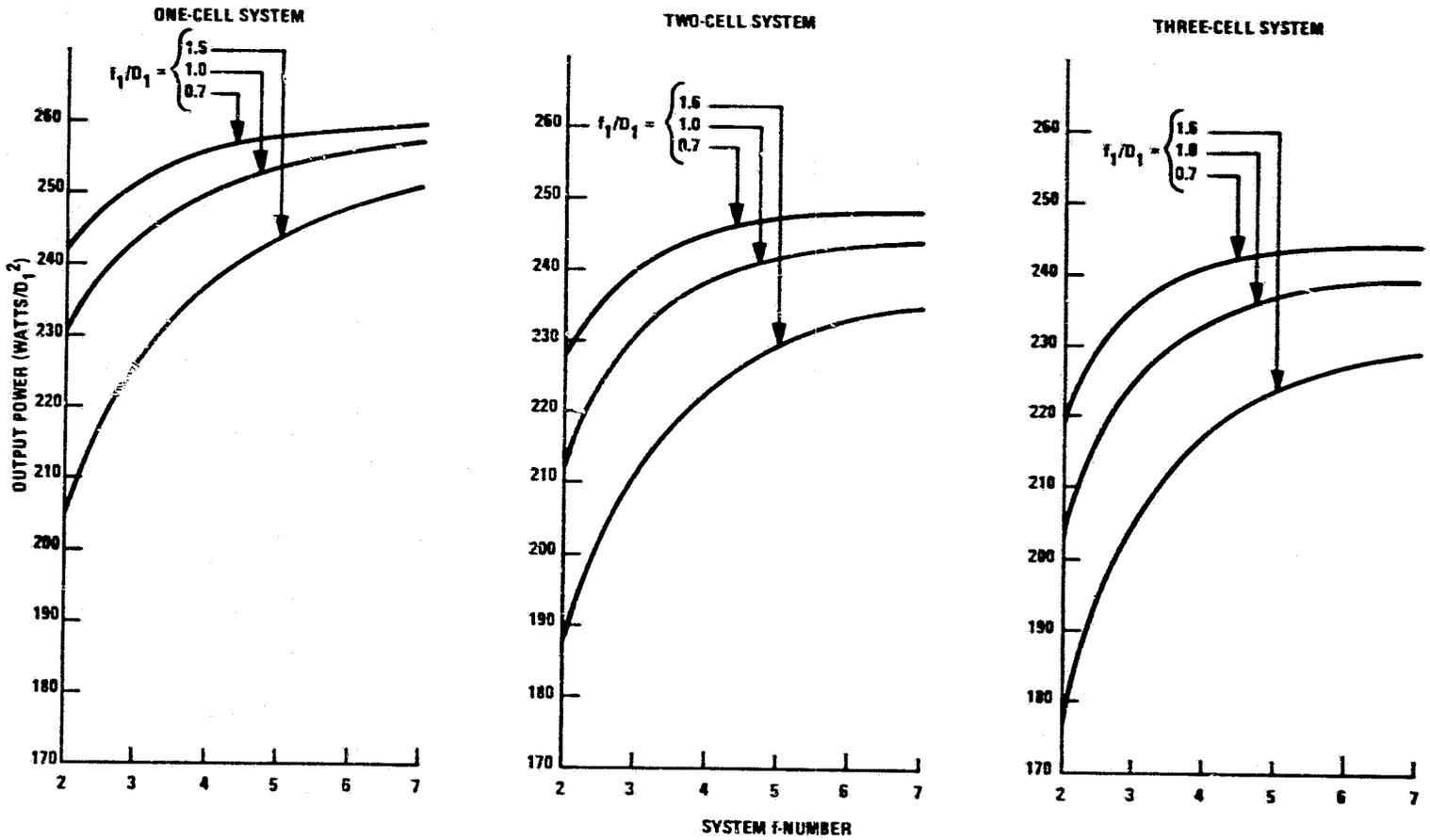

Figure 50. Normalized Output Power (P_{out}/D_1^2) where D_1^2 is in Square Meters as a Function of System f-Number and Primary Focal Length (f_1) (The solar-cell/beam-splitter efficiency is taken to be 30%.)

The cost of the various system components is illustrated in Figures 51 through 55. The cost of the primary mirror is $\$471/m^2$. The cost of the secondary mirror, shown in Figure 51, is smallest for low values of the primary mirror focal length and for large f-numbers. For these values the cost is less than $\$10/m^2$.

The radiator cost, as shown in Figure 52, is lowest for high values of the primary mirror focal length and is lowest for low f-numbers. However, all the values lie in the range from \$55 to \$65 per square meter for $f_1/D_1 = 0.7$. The cost is lowest for the three-cell systems.

The cost of the CPCs, as shown in Figure 53, rises sharply with increasing system f-number. Its dependence on the primary focal length is too slight to appear on the graph. For low system f-numbers the cost is in the range from \$5 to \$30 per square meter.

The cost of the beam splitters, as shown in Figure 54, is a minimum at system f-number f/3. For the two-cell system the cost is $\$23/m^2$; for the three-cell system it is $\$60/m^2$.

The cost of the solar cells, as shown in Figure 55, is a minimum for high primary focal length and low system f-numbers. However, all costs are less than $\$10/m^2$.

The total system cost is shown in Figure 56. For all of the systems it is a minimum for small primary focal lengths and at a system f-number of approximately f/3. The minimum values range from \$550 to \$650 per square meter.

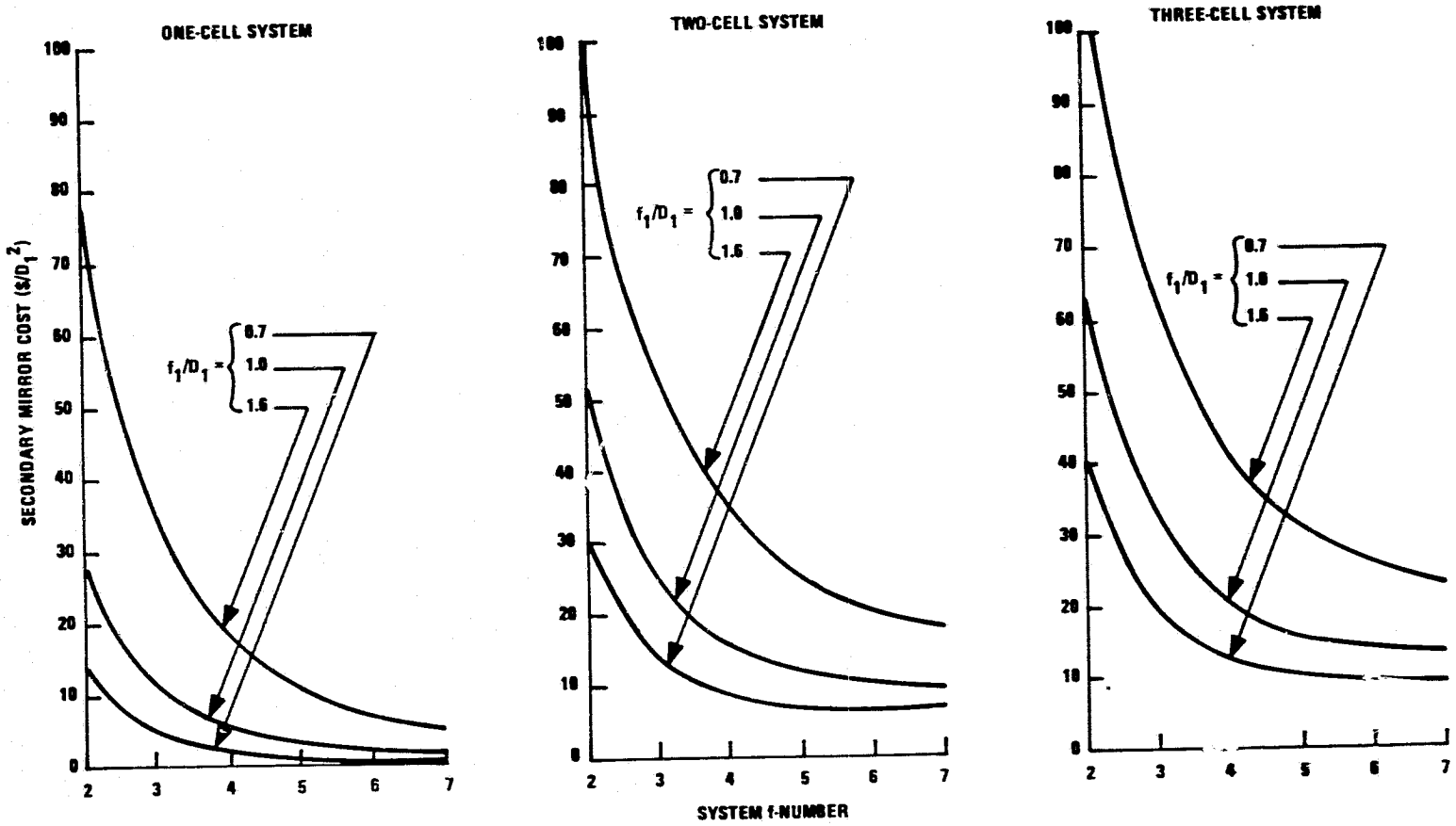

Figure 51. Normalized Cost of the Secondary Mirror as a Function of System f-Number and Primary Focal Length (f_1)

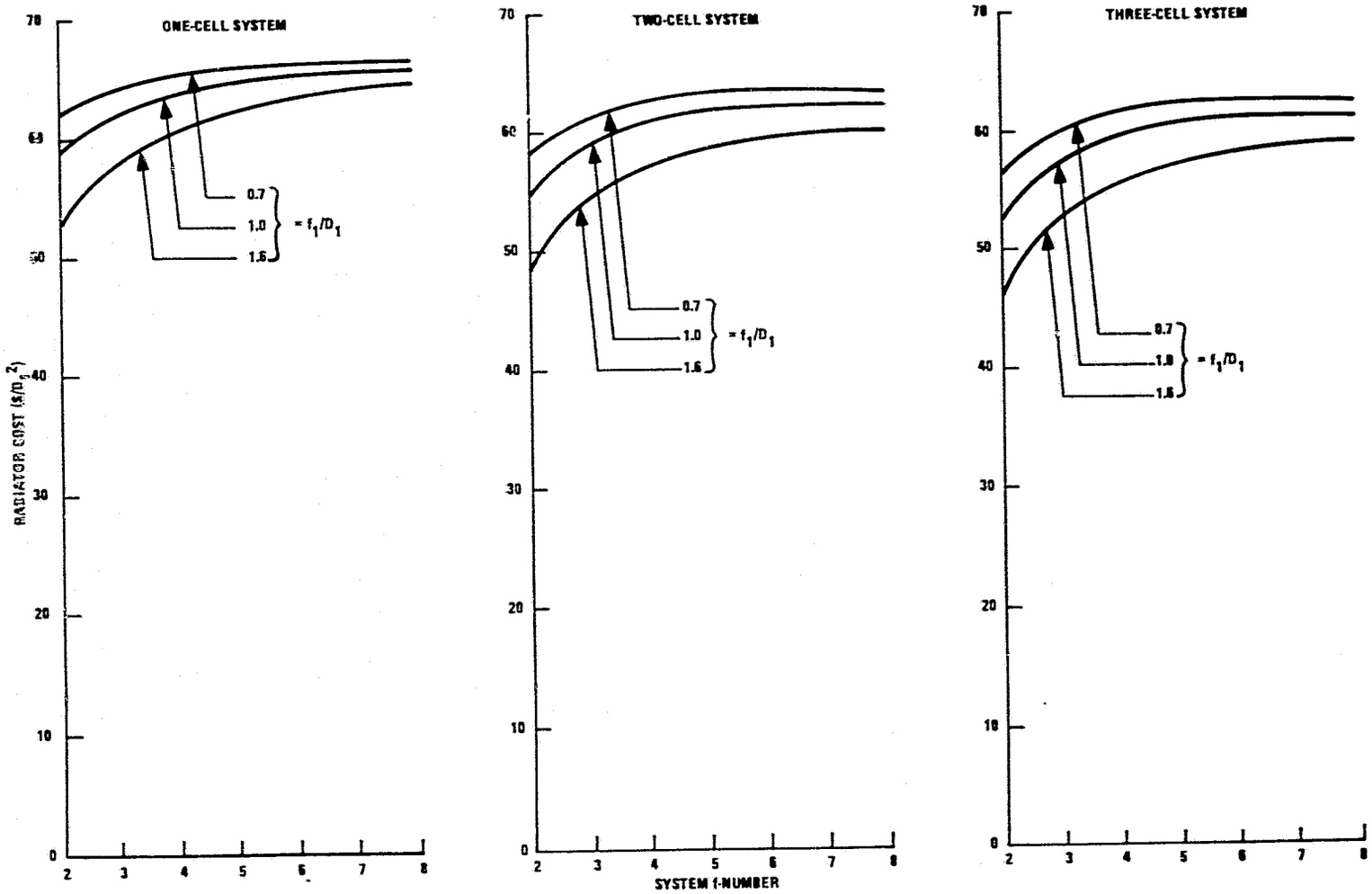

Figure 52. Normalized Cost of Radiator as a Function of System f-Number and Primary Focal Length (f_1) (It is assumed that the excess power to be removed from the cells is $20 W/cm^2$.)

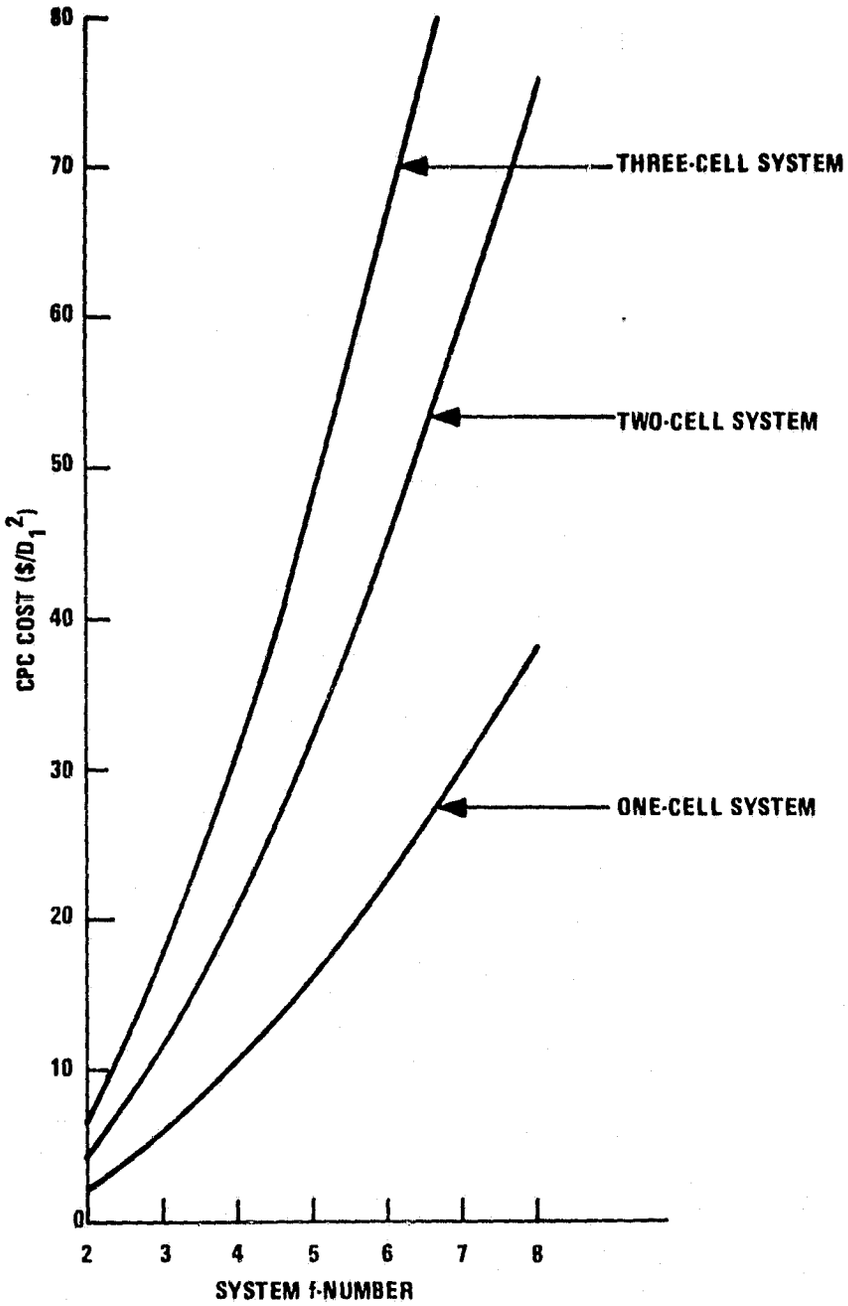

Figure 53. Normalized Cost of CPCs as a Function of System f-Number (Dependence on primary focal length f_1 is too slight to be seen.)

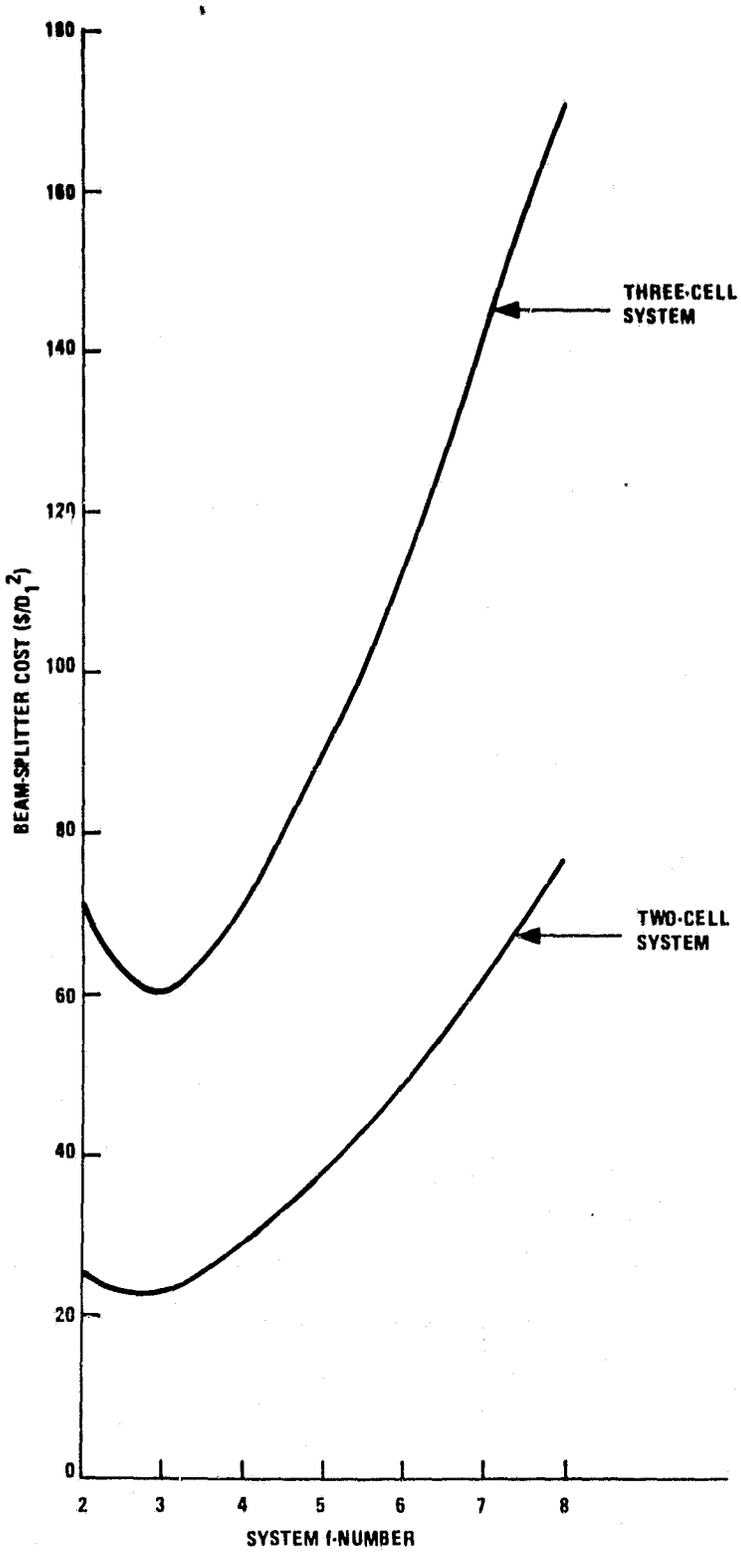

Figure 54. Normalized Cost of the Beam Splitters as a Function of System f-Number

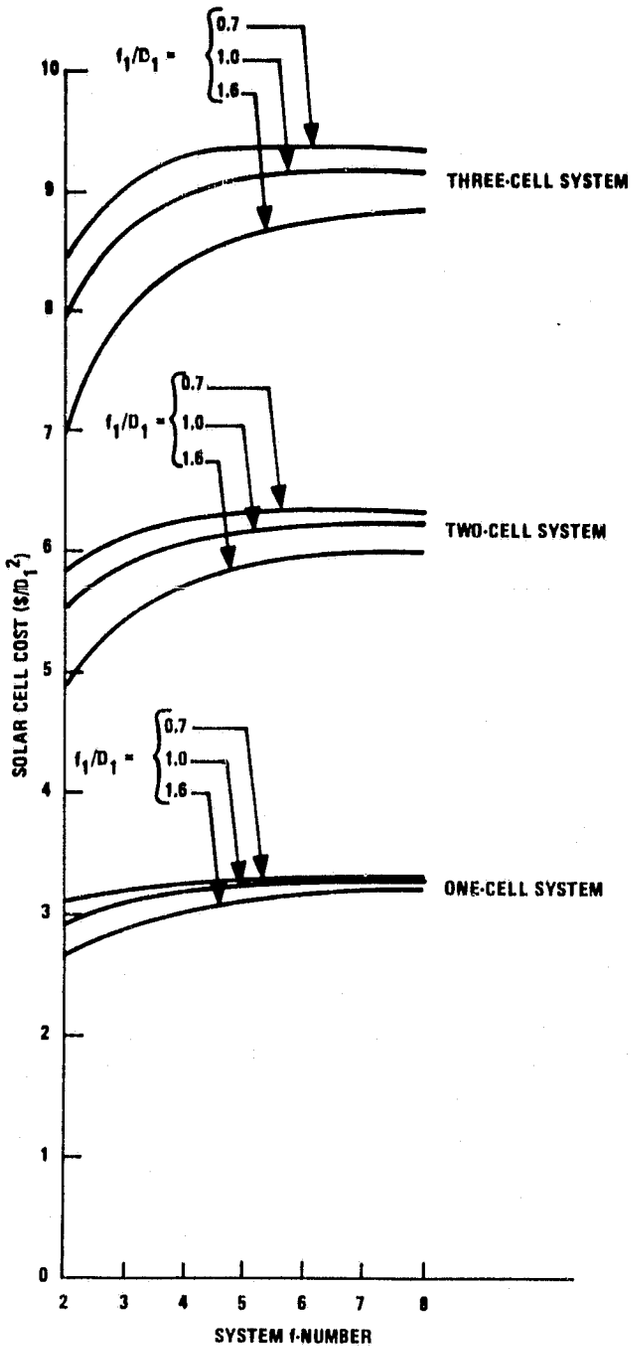

Figure 55. Normalized Cost of the Solar Cells as a Function of System f-Number and Primary Focal Length (f_1)

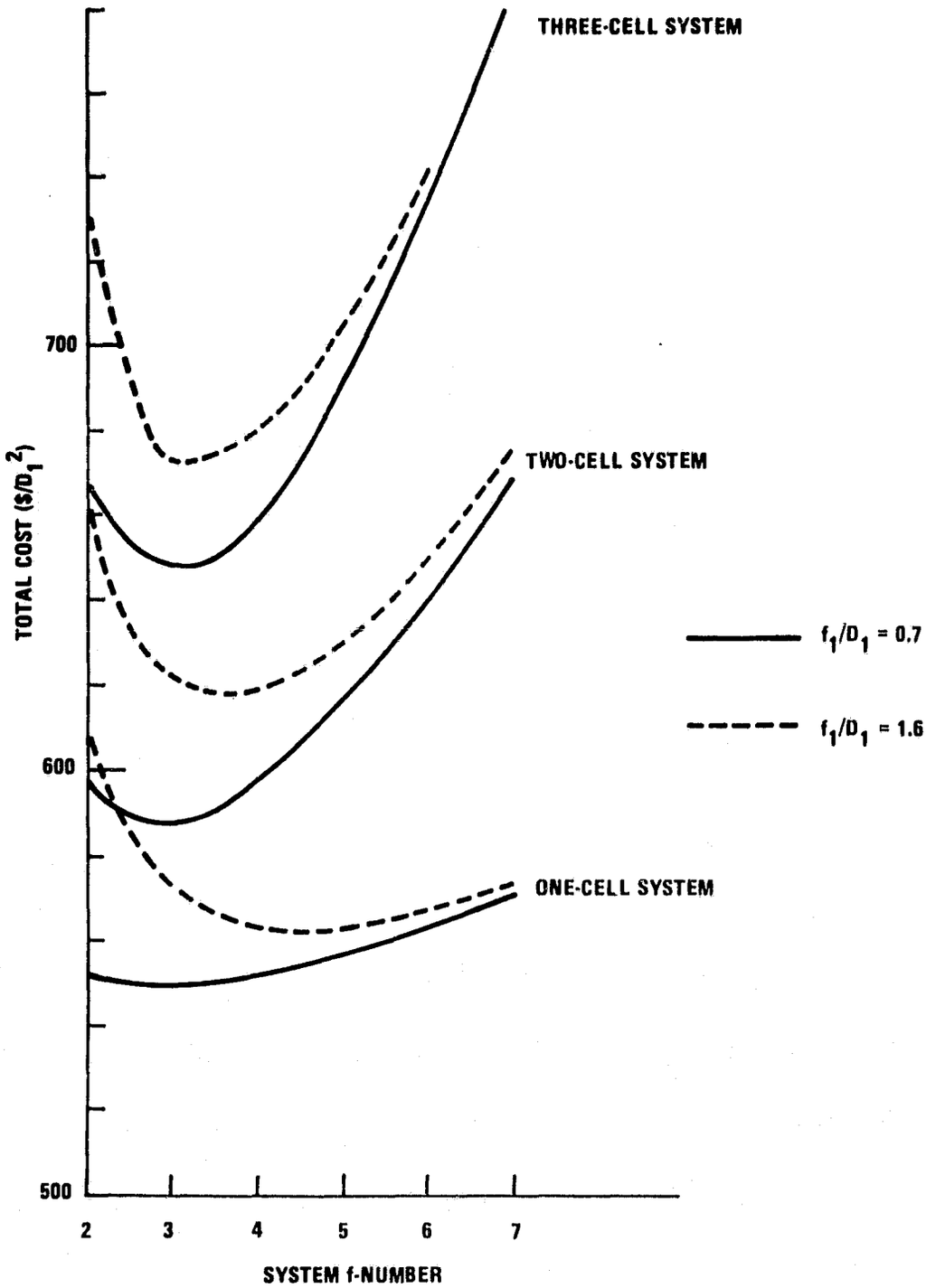

Figure 56. Normalized System Cost as a Function of System f-Number and Primary Focal Length (f_1)

The cost per peak watt of each system is shown in Figure 57. In all the systems it is lowest for low values of the primary focal length. In the two- and three-cell systems it is a minimum at a system f-number of about f/3.5. In the one-cell system it reaches a minimum value at f/4. Although the one-cell system appears to be more cost effective, it must be noted that the assumed efficiency is too high and the assumed excess power is too low.

In Figure 58 the various system component costs for a primary focal length of $f_1/D_1 = 0.7$ are compared. The main cost is the primary mirror, which represents about 70 to 85% of the cost. As can be seen, the solar cell costs are almost negligible.

In conclusion, the best optical system for two- and three-cell systems has a system f-number of f/3.5. For the one-cell system the system f-number should be f/4. For all systems the best primary focal length is $f_1/D_1 = 0.7$.

5.4 SELECTION OF CANDIDATE SOLAR-CELL/BEAM-SPLITTER SYSTEMS

In order to compare the solar-cell/beam-splitter systems described in subsection 4.4, we calculated the cost per peak watt for each system with an optical system having a system f-number of f/3 for the two- and three-cell systems, f/4 for the one-cell systems, and a primary focal length of $f_1/D_1 = 0.7$. The values of the efficiencies and excess power used were given in Tables 17, 18, and 19. In all cases, the cost of development of new solar cells was not included. This issue is discussed in subsection 5.5.

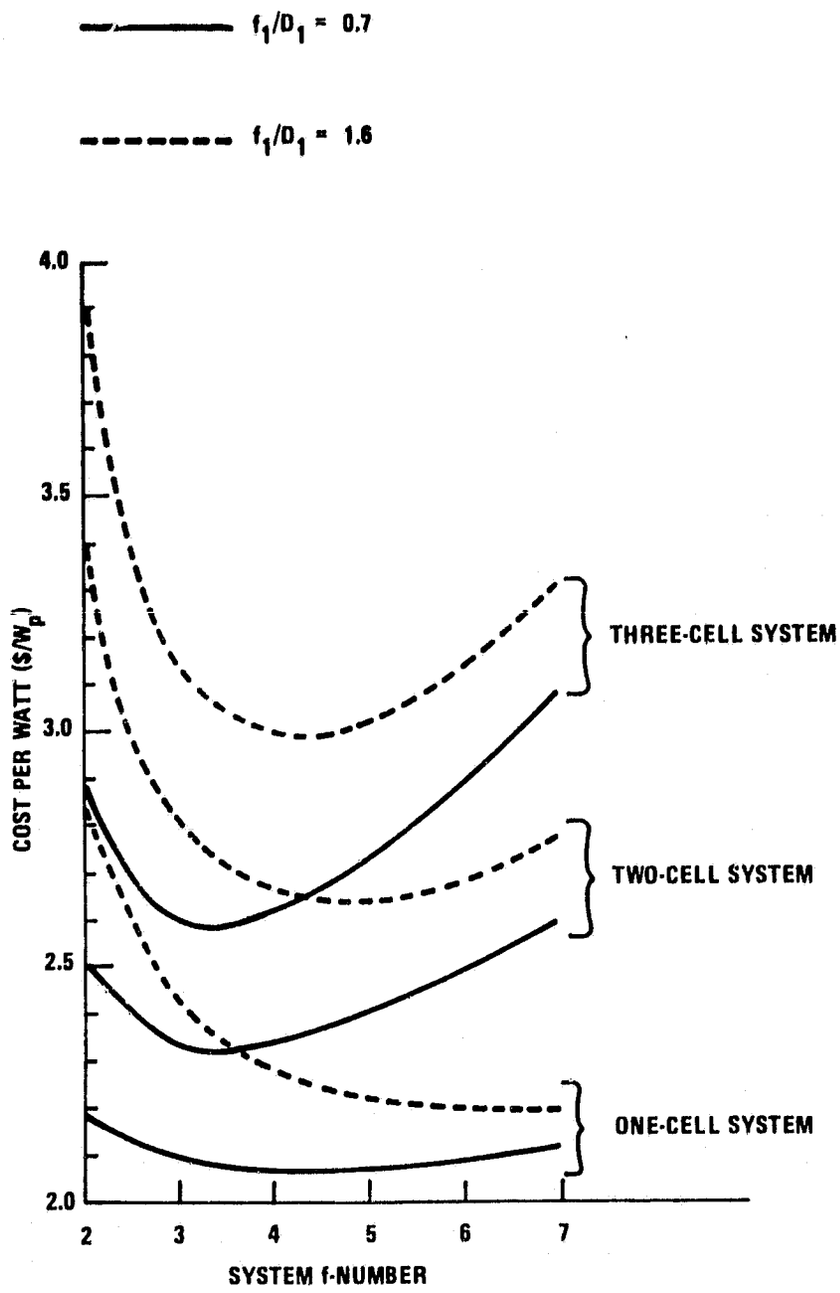

Figure 57. System Cost per Peak Watt as a Function of System f-Number and Primary Focal Length, f_1 (An efficiency of 30% is assumed, as well as an excess power of $20W/cm^2$.)

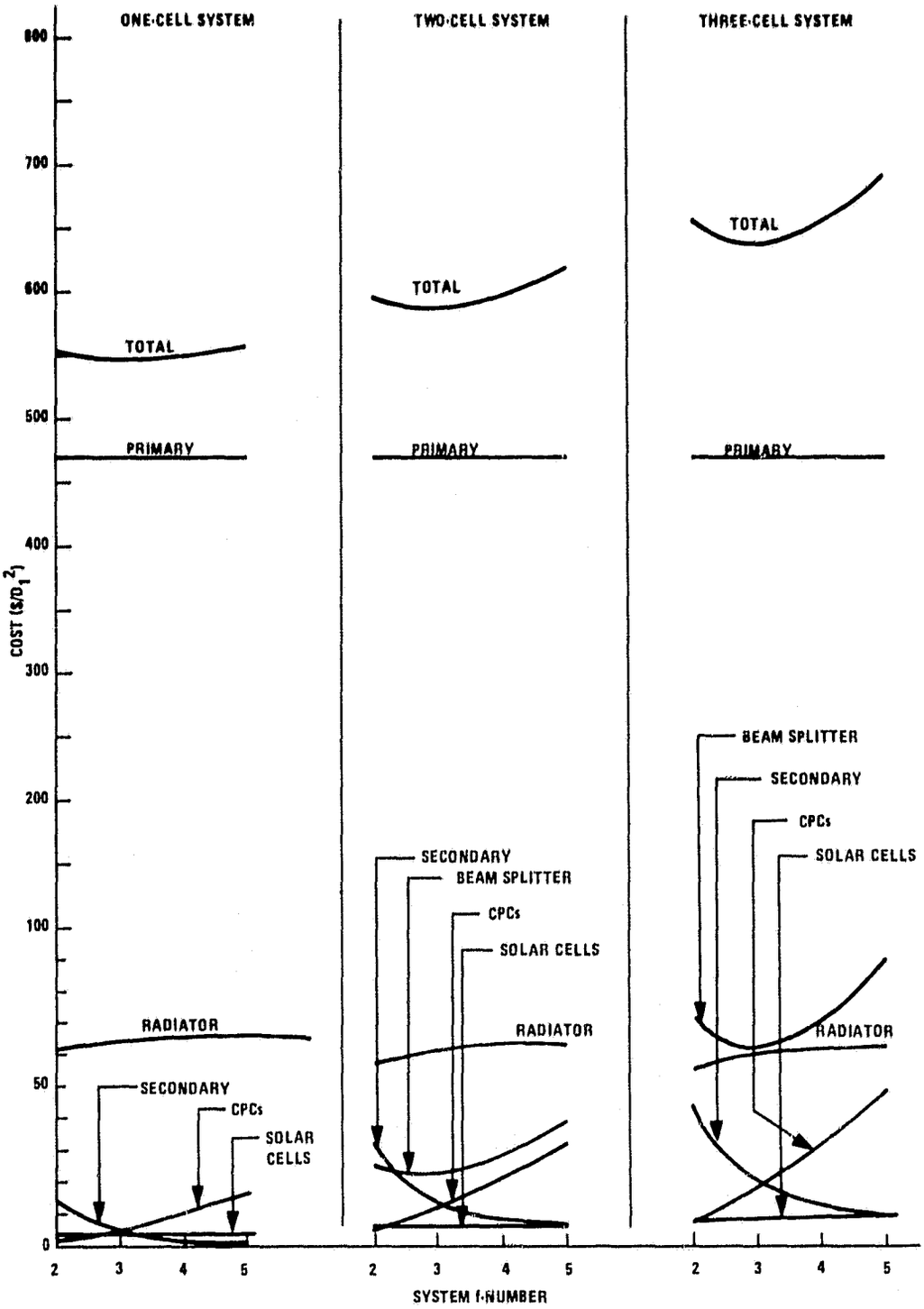

Figure 58. Breakdown of System Costs as a Function of f-Number for a Primary Focal Length of $f_1/D_1 = 0.7$ (An excess power of $20 W/cm^2$ is assumed.)

Other solar cell tradeoff factors were discussed in subsection 4.4. The effect of long-wavelength energy falling on small energy bandgap solar cells was not considered a problem because the back side of the solar cells can be treated so that they do not absorb this energy. The number of UV-resistant mirrors was also not taken into account because although it is more difficult to design such mirrors, it will not impact the overall cost of the beam splitters.

The results for systems that require no new solar cell development are listed in Table 21. The best system is GaAs/Si with a cost of $\$2.522/W_p$. The best single-cell system is GaAs with a cost of $\$2.684/W_p$.

TABLE 21. COST OF SYSTEMS REQUIRING NO NEW SOLAR CELL DEVELOPMENT

Cell Configuration	Efficiency (percent)	Excess Power Absorbed in Cell (W/cm^2)	Cost ($\$/W_p$)
GaAs / Si	28.4	23.5	2.522
Si / GaAs	26.6	21.5	2.665
GaAs	23.7	23.22	2.684
Si	21.4	30.52	3.098

The results for systems requiring development of one new solar cell are listed in Table 22. The best is GaAs/Ge with a cost of $\$2.369/W_p$. It should be noted that adding Si to this system increases its cost to $\$2.483/W_p$. The best system with GaP is GaAs/GaP/Si with a cost of $\$2.551/W_p$. Close in cost to it is a GaAs/GaP system with a cost of $\$2.569/W_p$.

The results for systems requiring development of two new solar cells are listed in Table 23. The best is GaAs/GaP/Ge with a cost of $\$2.410/W_p$.

The cost per peak watt of the systems discussed above are plotted in Figure 59 as a function of f-number for a primary focal length of $f_1/D_1 = 0.7$. The potentially most cost-effective systems are GaAs/Ge and GaAs/Si. The optimum f-number is f/3.5. The trade-offs between these costs and the cost of solar cell development are discussed next.

5.5 IMPACT OF NEW SOLAR CELL DEVELOPMENT ON TOTAL SYSTEM COST

The multi-cell systems shown to be most cost-effective are GaAs/Ge and GaAs/Si. If the cost of cell development is excluded, the cost per peak watt of the GaAs/Ge system is $\$2.37/W_p$. The GaAs/Si system, for which solar cells have already been developed, has a cost per peak watt of $\$2.52/W_p$.

The impact of new solar cell development on total system cost can be evaluated by considering the number of systems to be built. Assuming that the systems each have an output power of 100 kW, the required primary mirror diameter, D_1, can be determined from

$$P_{out} = 100 \text{ kW} = (P_{out}/D_1^2)\, D_1^2$$

TABLE 22. COST OF SYSTEMS REQUIRING DEVELOPMENT OF ONE NEW SOLAR CELL

Cell Configuration	Efficiencies (percent)	Excess Power Absorbed in Cells (W/cm^2)	Cost* ($\$/W_p$)
GaAs Ge	31.8	33.6	2.369
Ge GaAs	50.3	32.5	2.473
GaAs Si Ge	32.6	27.7	2.483
GaAs Ge Si	32.5	28.2	2.496
GaAs GaP Si	29.5	12.3	2.551
GaAs GaP	26.2	11.82	2.569
GaP GaAs Si	29.1	12.1	2.583
GaAs Si GaP	28.8	11.8	2.607
GaP GaAs	25.8	11.7	2.608
Si GaAs Ge	30.4	25.5	2.635
Ge GaAs Si	30.5	26.4	2.638

*Does not include cost of new solar cell development.

TABLE 22. COST OF SYSTEMS REQUIRING DEVELOPMENT OF ONE NEW SOLAR CELL (concluded)

Cell Configuration	Efficiencies (percent)	Excess Power Absorbed in Cells (W/cm^2)	Cost* ($\$/W_p$)
GaP Si GaAs	28.1	11.6	2.669
Si GaAs GaP	27.7	11.2	2.702
Si GaP GaAs	27.4	11.2	2.732
Si GaP	25.3	16.8	2.733
Ge Si GaAs	29.0	24.5	2.750
GaP Si	25.1	17.2	2.761
Si Ge GaAs	28.8	24.1	2.764
Si Ge	25.5	34.9	2.974
Ge Si	24.2	32.7	3.100
GaP	11.8	5.56	4.839
Ge	14.8	57.53	5.152

*Does not include cost of new solar cell development.

TABLE 23. COST OF SYSTEMS REQUIRING DEVELOPMENT OF TWO NEW SOLAR CELLS

Cell Configuration	Efficiencies (percent)	Excess Power Absorbed in Cells (W/cm^2)	Cost* ($\$/W_p$)
GaAs GaP Ge	32.6	21.3	2.410
GaP GaAs Ge	32.2	21.1	2.438
GaAs Ge GaP	32.1	21.8	2.453
GaP Ge GaAs	31.4	21.6	2.506
Ge GaAs GaP	31.4	22.2	2.513
Ge GaP GaAs	31.1	22.2	2.537
Si GaP Ge	29.4	21.0	2.669

*Does not include cost of new solar cell development.

TABLE 23. COST OF SYSTEMS REQUIRING DEVELOPMENT OF TWO NEW SOLAR CELLS (concluded)

Cell Configuration	Efficiencies (percent)	Excess Power Absorbed in Cells (W/cm^2)	Cost* ($\$/W_p$)
GaP Si Ge	29.2	20.3	2.678
Si Ge GaP	28.6	21.0	2.743
GaP Ge Si	28.1	19.9	2.778
Ge Si GaP	27.9	20.3	2.803
Ge GaP Si	27.6	19.9	2.828
GaP Ge	23.3	35.4	3.262
Ge GaP	23.4	37.8	3.286

*Does not include cost of new solar cell development.

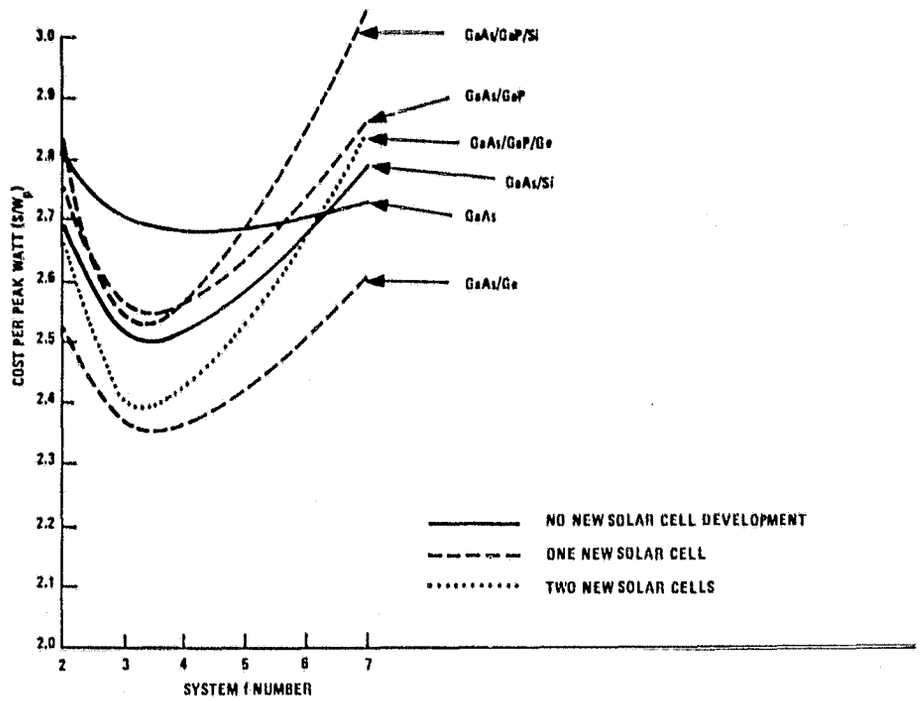

Figure 59. System Costs per Peak Watt of the Best Candidate Systems (A primary mirror focal length of $f_1/D_1 = 0.7$ was assumed. No account was taken of the cost of solar cell development.)

For a system f-number of f/3.5, which is optimum for a two-cell system, P_{out}/D_1^2 is $253 W/m^2$ for a 30% efficient solar-cell/beam-splitter system. The GaAs/Ge and GaAs/Si systems have efficiencies of 31.8 and 28.4%, respectively. Since P_{out}/D_1^2 is proportional to the efficiencies,

$$P_{out}/D_1^2 = \begin{cases} \$268.2/m^2, & \text{GaAs/Ge} \\ \$239.5/m^2, & \text{GaAs/Si} \end{cases}$$

Hence, the required primary mirror diameters are

$$D_1 = \begin{cases} 19.3\text{m}, & \text{GaAs/Ge} \\ 20.4\text{m}, & \text{GaAs/Si} \end{cases}$$

For a one-meter primary mirror, the cost of the two-cell systems, excluding the cost of new solar cell development, is

$$C = \begin{cases} \$630.27, \text{ GaAs/Ge} \\ \$598.27, \text{ GaAs/Si} \end{cases}$$

where the appropriate excess power requirements of the two systems are used in determining the radiator costs. For 100 kW systems these costs must be multiplied by the square of the appropriate primary mirror diameter, so

$$\text{Cost} = \begin{cases} \$2.35 \times 10^5, \text{ GaAs/Ge} \\ \$2.49 \times 10^5, \text{ GaAs/Si} \end{cases}$$

Assuming that n 100 kW systems are to be built, the total cost per peak watt is given by

$$\text{Cost per peak watt} = \frac{n \text{ Cost} + P_{sc}}{n(100 \text{ kW})}$$

where P_{sc} is the initial cost of development of a new solar cell. In Figure 60 the costs per peak watt of the two systems are compared as a function of n for several values of P_{sc} ranging from \$2M to \$5M. In order to be competitive with a GaAs/Si system, the number of GaAs/Ge systems to be built would need to be 143, 214, 285, and 357 for Ge solar cell development costs of \$2M, \$3M, \$4M, and \$5M, respectively. Hence for the near-term applications, GaAs/Si systems are the most cost-effective. In addition, development of Ge solar cells should be started in order to make a more accurate assumption as to the total cost of the development effort required.

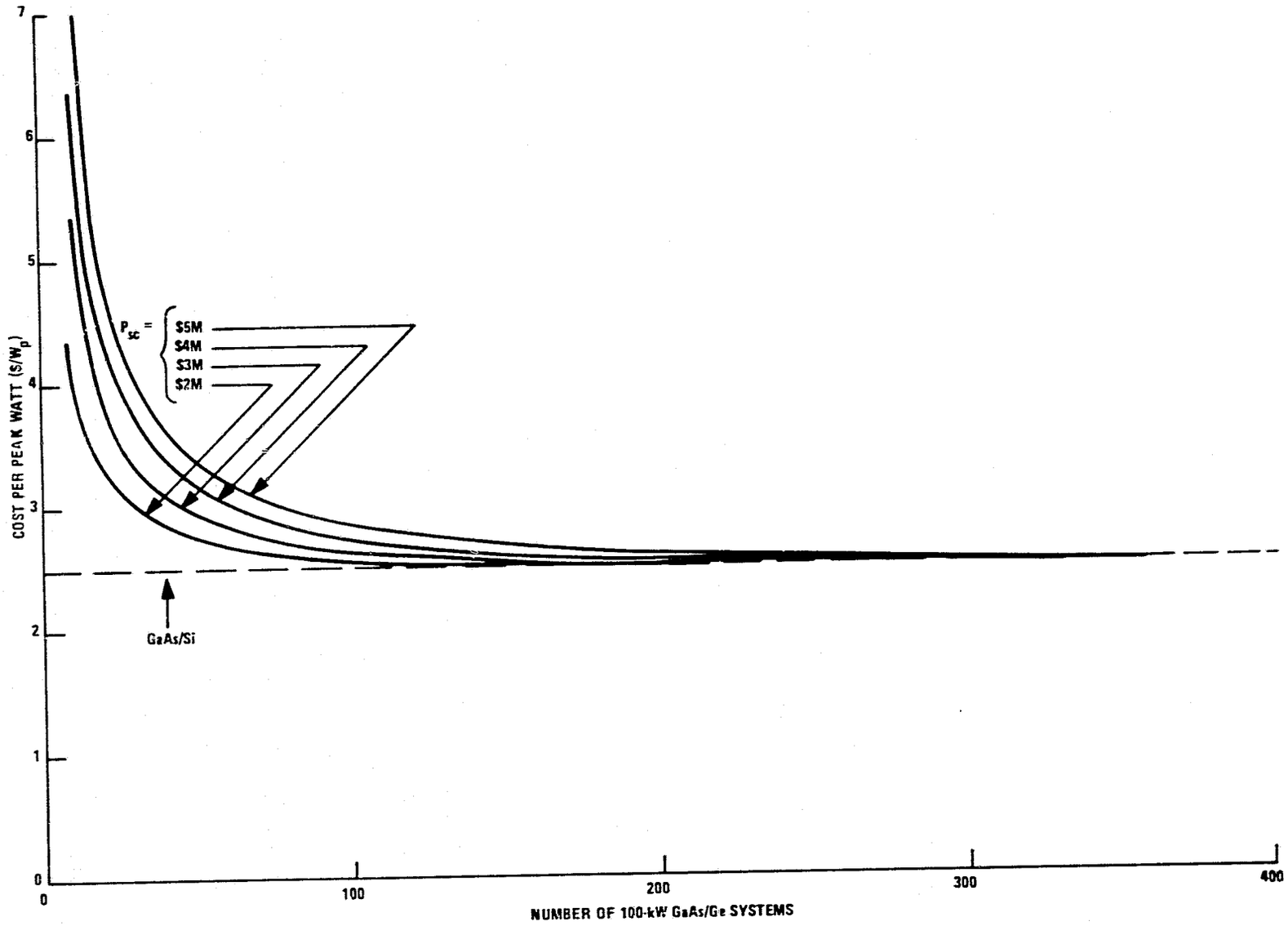

Figure 60. Estimate of Total Cost per Peak Watt of a GaAs/Ge System as a Function of the Number of 100-kW Systems to Be Built

SECTION 6

FINAL DESIGN OF OPTIMUM SYSTEM

The proposed final design for the solar power system consists of a Cassegrain telescope and two CPCs for solar energy concentration of 1000 to 1, a single dichroic beam splitter, and GaAs and Si solar cell arrays. All of the light entering the CPC emerges at the solar cells located at its exit aperture. Fresnel lenses may be used to facilitate fabrication and deployment.

A preliminary thermal design analysis was conducted to estimate sizing and performance data which can be used in the optimization of a cooling system. A two-sided, finned radiator concept was analyzed in order to illustrate the methodology which can be used to determine potential performance characteristics.

6.1 OPTICAL DESIGN

The final optical system design consists of a Cassegrain telescope for the first stage of concentration followed by a CPC for each solar cell array for the second stage of concentration, as depicted in Figure 61. The Cassegrain uses a parabolic primary and a hyperbolic secondary to relay the image of the sun to the CPCs. The dichroic beam splitter, inclined 68 deg from the optical axis, reflects the solar energy of wavelengths less than 0.9 μm to the first CPC while transmitting the rest to the second CPC. The solar cell arrays are located at the ends of the CPCs, with GaAs used in the first array and Si used in the last.

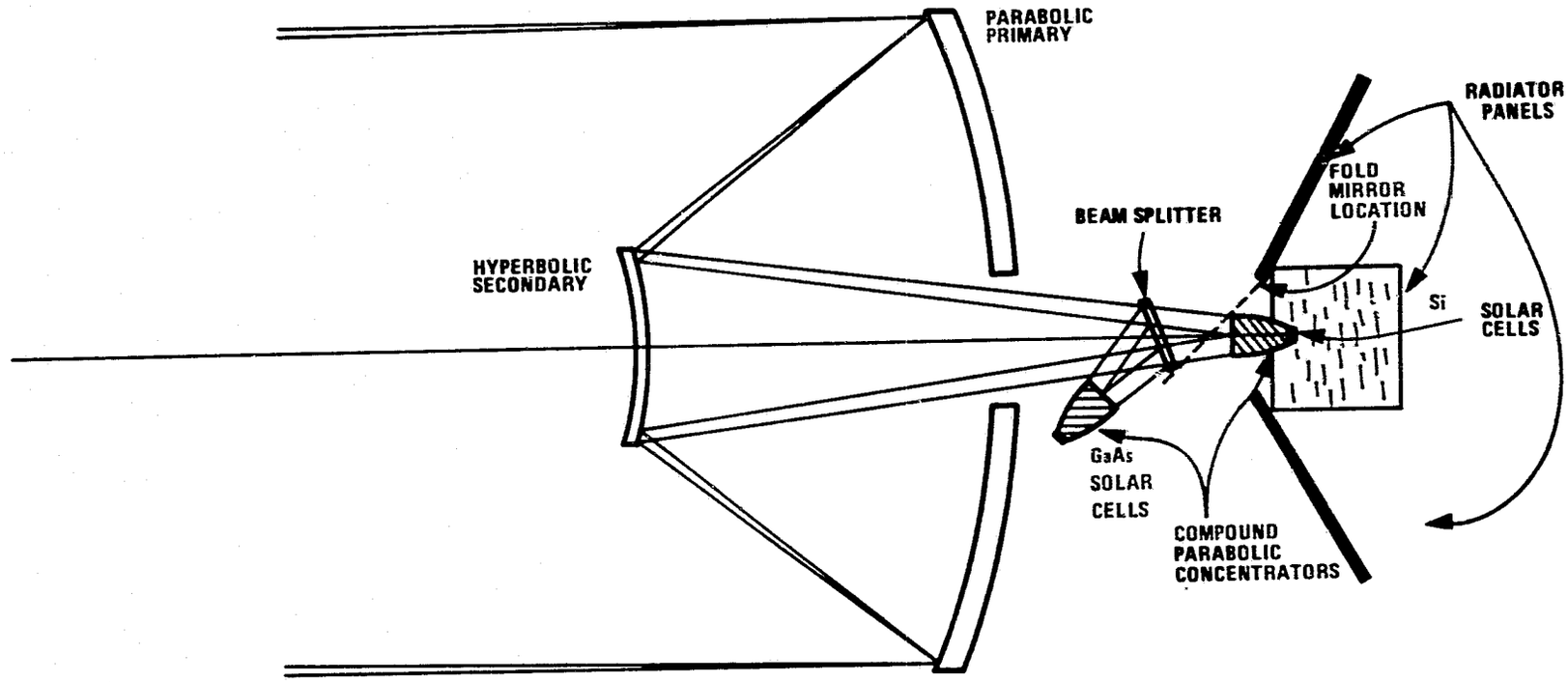

Figure 61. Final Optical System Design Schematic

It should be noted that the overall system length can be further shortened by the insertion of a folding mirror, as shown by the dashed line in Figure 61. With this configuration the second CPC and solar cell array would be located near the top of the beam splitter.

A computer listing of the optical constructional parameters of the final system is given in Figure 62. The basic lens data details the surface profiles and surface separations for the Cassegrain and CPC components. Note that all linear dimensions have been normalized to a primary diameter value of 1.0, thus allowing the system to be easily scaled up to a particular size for a given power output. Surfaces 1 and 2 are the Cassegrain primary and secondary; surface 3 is the entrance aperture of the CPC. Surface 4 is the nominal location of the solar cells while surface 5 defines the CPC profile. Because a given ray can undergo multiple reflections from the surface of the CPC before striking the solar cell plane, the surface profile of the CPC must be entered a number of times, as is indicated by surfaces 6-15. This representation is sufficient to allow up to six reflections of the ray on the CPC. Although it is easy to extend the number of surfaces even further should the ray require more than six CPC reflections, most rays only require one CPC reflection before striking the solar cells. Thus we have arbitrarily limited the number of CPC reflections to six.

Since this concentration system is not an imaging system, a conventional image analysis does not result in the most useful information regarding the system's ability to concentrate energy. While certain key rays were traced to determine that the system was input to the computer correctly, we chose to evaluate an entire aperture bundle of rays from selected field points to determine that all of the rays hit the solar cells. Examples of

```
****************************************

SOLAR CONCENTRATOR - FINAL DESIGN
SYSTEM SCALED TO PRIMARY DIAMETER = 1
CPC REPRESENTED AS ELLIPSE

****************************************
```

LENS UNITS ARE INCHES

REF OBJ HT		REF AP HT	OBJ SURF	REF SURF	IMG SURF
-.436335E+08 (	.25 DG)	.50000	0	1	17

EFL	BF	F/NBR	LENGTH	GIH
3.5000	0.0000	3.50	.4532	.0165

WAVL NBR	1	2	3	4	5
WAVELENGTH	.58756	.48613	.65627	.43584	.70652
SPECTRAL WT	1.0000	1.0000	1.0000	1.0000	1.0000

BASIC LENS DATA

SURF	CV	RD	TH	MEDIUM
0	0.000000	0.000000	1.000000E+10	AIR
1	-.714286	-1.400000	-.522000	REFL
2	-2.247191	-.445000	.890000	REFL
3	0.000000	0.000000	.085244	AIR
4	0.000000	0.000000	.010942	AIR
5	-103.737668	-.009640	-.010942	REFL
6	0.000000	0.000000	.010942	AIR
7	-103.737668	-.009640	-.010942	REFL
8	0.000000	0.000000	.010942	AIR
9	-103.737668	-.009640	-.010942	REFL
10	0.000000	0.000000	.010942	AIR
11	-103.737668	-.009640	-.010942	REFL
12	0.000000	0.000000	.010942	AIR
13	-103.737668	-.009640	-.010942	REFL
14	0.000000	0.000000	.010942	AIR
15	-103.737668	-.009640	-.010942	REFL
16	0.000000	0.000000	0.000000	AIR
17	0.000000	0.000000	0.000000	AIR

CC AND ASPHERIC DATA

SURF	CC
1	-1.00000E+00
2	-2.25000E+00
5	-9.91160E-01
7	-9.91160E-01
9	-9.91160E-01
11	-9.91160E-01
13	-9.91160E-01
15	-9.91160E-01

Figure 62. Optical Layout for Solar Concentrator

the output are given in Figures 63 and 64. Figure 63 represents the rays traced into the primary mirror for an on-axis field point. The number 4 on the figure indicates that these rays hit the solar cells directly and do not reflect off the CPC. Thus, no rays entering the primary mirror on-axis reflect off the CPC before striking the solar cells.

To allow for the inherent errors in manufacture of the reflecting surfaces, the image blur size of the sun produced by the Cassegrain was allowed to double ($\alpha = 2$). Thus the entrance aperture of the CPC was taken to be twice the nominal solar image diameter. We chose to approximate the surface errors producing this enlarged and blurred solar image, by raytracing from a field point corresponding to twice the actual extent of the sun. The results are shown in Figure 64. The numbers and letters 6, 8, A, C, E, G indicate 1, 2, 3, 4, 5, 6 CPC reflections, respectively, for that particular ray, while a period (.) indicates rays with more than six CPC reflections. The majority of the rays from this extreme field point hit within six CPC reflections. The same raytrace performed from a field point corresponding to 1.5 times the extent of the sun had all rays requiring only one CPC reflection. Thus, it is only a very few, extreme rays that require more than one CPC reflection, which is just what is to be expected from the CPC.

The surface profile of the CPC is shown in Figure 65. The concentrated solar blur from the Cassegrain telescope enters the CPC entrance aperture, undergoes an average of about one reflection off the CPC, and finally hits the solar cells located at the exit aperture. The elliptical profile used to

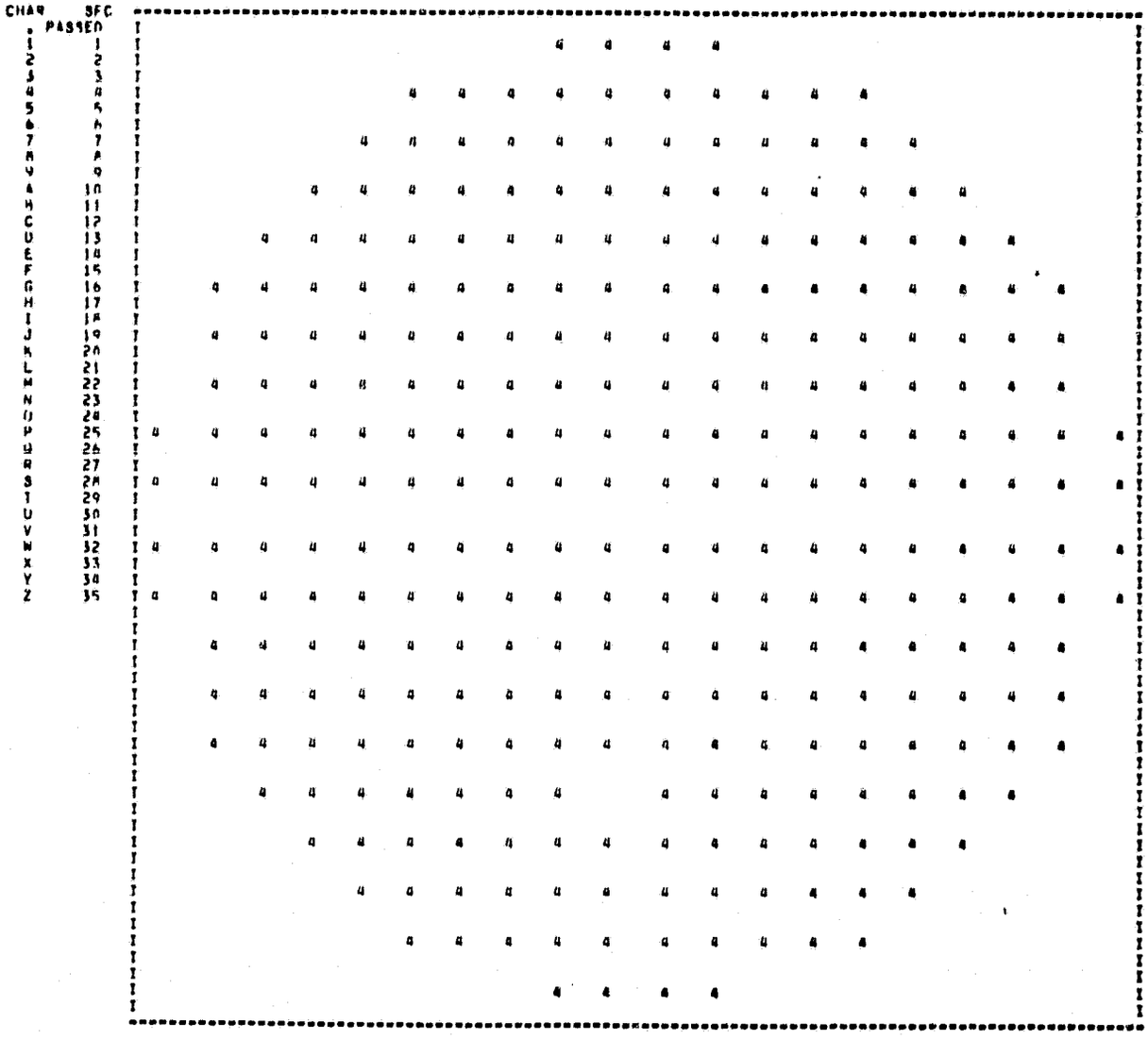

Figure 63. On-Axis Bundle Ray Trace

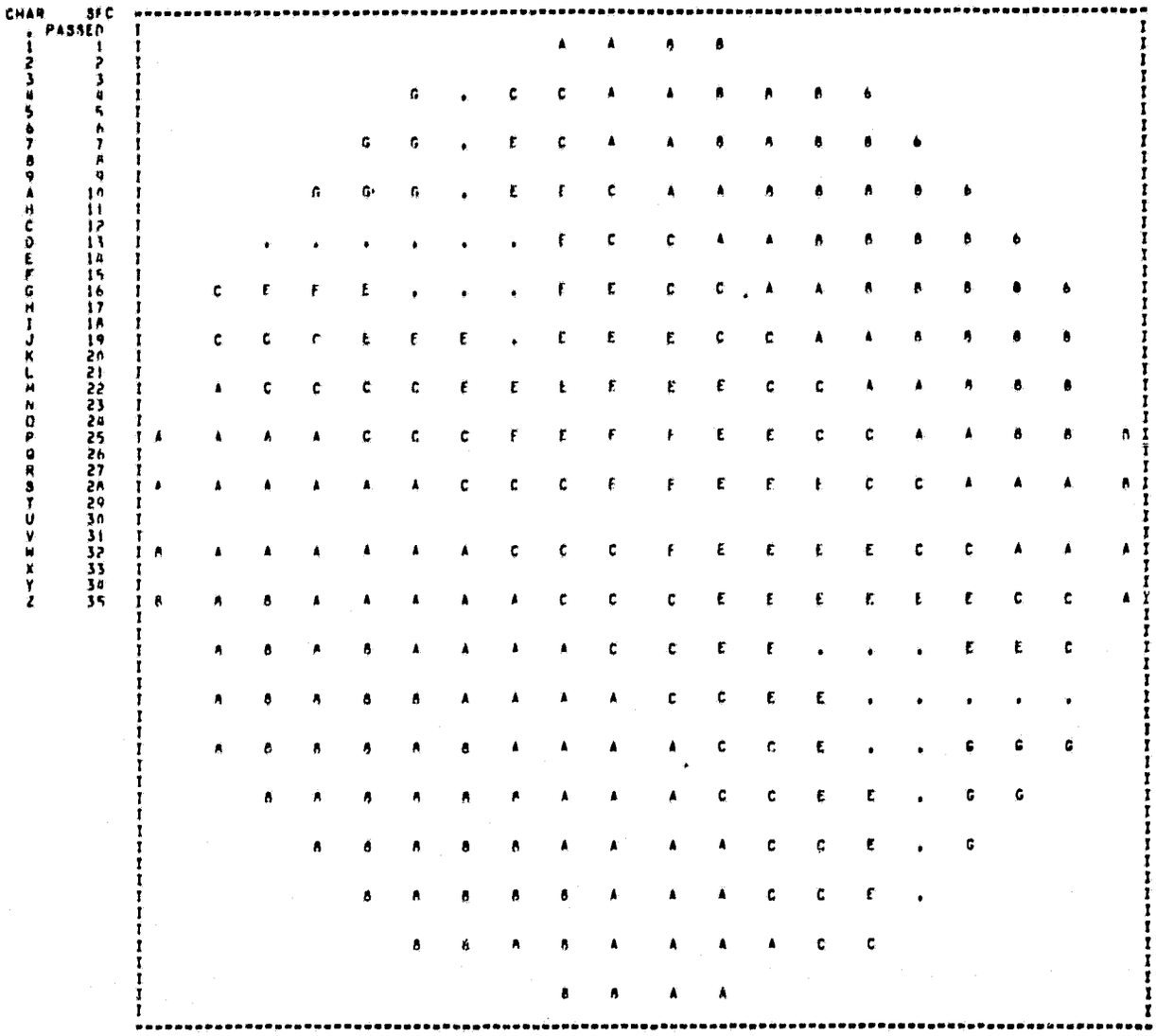

Figure 64. Off-Axis Bundle Ray Trace

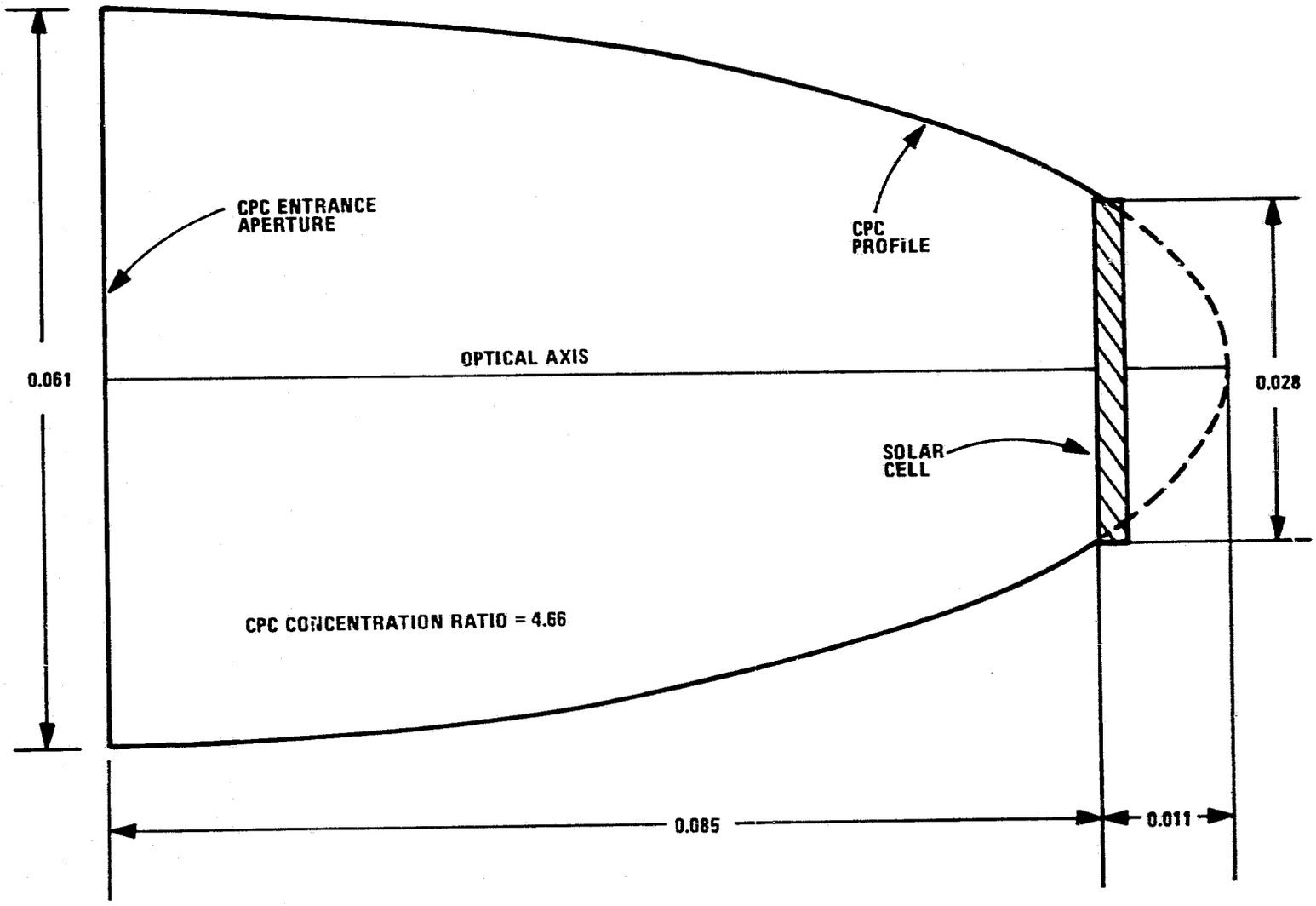

Figure 65. Final System Design CPC Profile, Scaled to Primary Diameter = 1

represent the CPC surface is continued in dashed lines to indicate the position where the exit aperture is situated relative to the entire elliptical profile. Note once again that all dimensions have been scaled to a primary diameter value of 1.0. The CPC concentration ratio of 4.66 results in a CPC only slightly longer than its entrance aperture; thus it appears that no truncation of the CPC is needed at its entrance aperture. Additionally, by not truncating the CPC, the entire surface area can be used to help cool the CPC.

Additional system data is tabulated in Table 24 for the final system design. Note that the secondary diameter is sufficiently small to amount to an area obscuration of only 7.3% of the entering beam. The concentration ratios for the first and second stages, 269.63 and 4.66 respectively, result in a system concentration of 1256.6. This is a design concentration, which when adjusted for the actual optical inefficiencies of the system (reflection losses, obscuration, absorption) results in the nominal system concentration of 1000.

A recent second-stage concentration form has been analyzed by Winston[17] for use as a second stage concentrator following first-stage image-forming concentrators. This concentrator is called the compound elliptical concentrator (CEC) and is a variant of the CPC, with many similar

---

[17] R. Winston and W. T. Welford, "Design of Nonimaging Concentrators as Second Stages in Tandem with Image-Forming First-Stage Concentrators," Applied Optics, Vol. 19, No. 3, 1980, pp. 347-351.

TABLE 24. SOLAR CONCENTRATOR FINAL DESIGN

Parameter	Parameter Value	
	Normalized System	GaAs|Si, 100 kW
Primary diameter	1m	20.43m
Primary focal length	0.7m	14.30m
Primary conic constant	-1	-1
Secondary diameter	0.26m	5.31m
Secondary focal length	0.2225m	4.55m
Secondary conic constant	-2.25	-2.25
Secondary Magnification	5.0	5.0
Obscuration (Area)	7.3%	7.3%
Obscuration efficiency	0.927	0.927
CPC diameter	0.061m	1.25m
CPC length	0.085m	1.74m
Cassegrain concentration	269.63	269.63
CPC concentration	4.66	4.66
System concentration (Design)	1256.60	1256.60
System focal length	3.5m	71.51m
System f-number	3.5	3.5
Beam splitter area	$0.0075m^2$	$3.13m^2$
Solar cell array diameter	0.0282m	0.576m

properties. Its use is advantageous when attempting to reach the ideal thermodynamic limit of concentration for a given system. In such applications, an additional concern is the aberrations associated with highly concentrating first-stage concentrators, such as a simple paraboloid reflector. The proposed system we have analyzed makes no attempt to reach the thermodynamic limit of concentration, nor do the optical aberrations of the Cassegrain telescope result in any significant loss of energy at the entrance aperture of the CPC. Thus, while other variations of the CPC design profile will produce the same system concentration as the CPC, the nominal CPC profile remains quite adequate to efficiently serve as a second-stage concentrator.

While the optical surfaces of the Cassegrain telescope have been depicted in the classical sense of being fabricated as concave and convex dish reflectors, other candidate surface representations should not be ruled out. One possible surface type is the fresnel lens, which has many desirable properties from a fabrication and deployment standpoint. It is conceivable to use flat reflecting fresnel surfaces for the Cassegrain and thus eliminate a large portion of the structural mounting requirements associated with conventional surface fabrication. While radially-cut fresnel surfaces are not likely candidates for apertures as large as 20 meters, crossed linear-cut (embossed) fresnels are easily fabricated in large widths and lengths today. These could be relatively easily packaged and deployed to be used for the first stage of concentration. Of course a number of other problems, such as the long-term effects of solar radiation on the substrates, would have to be considered. However, conceptually the concentrator designs need not be limited to conventional reflecting structures.

6.2 THERMAL DESIGN ANALYSIS

A preliminary thermal design analysis was conducted to provide sizing and performance data that could be used in the optimization of the cooling system for the solar power system. A single non-optimized concept was analyzed in order to illustrate the methodology to be used for determining potential performance characteristics.

The cell cooling system analyzed consisted of a rectangular aluminum extrusion containing axial coolant flow channels. The individual solar-cell arrays were mounted on the extrusion with an electrically insulating, thermally conducting adhesive. Figure 66 shows a cross-sectional view of the cell mounting module. Figure 67 illustrates a possible arrangement for placing the solar cell arrays within the illuminated field. To provide high voltages at modest amperage it is necessary to connect several cells in series. For efficient operation, all series-connected cells must provide the same current; hence all cells must be fully illuminated. This may result in some wasted area or may require other than a circular zone of illumination. For purposes of the cooling system performance evaluation only the central extrusions were considered since they represent the worst-case heat flux to an extrusion.

There are four interdependent heat transfer processes to be considered in analyzing the cooling of the solar cells: 1) heat transfer from the cells through their mount, 2) convective transfer of heat from the mount extrusion to the liquid coolant, 3) convective transfer of heat from the coolant to a finned radiator, and 4) radiation of the heat into space.

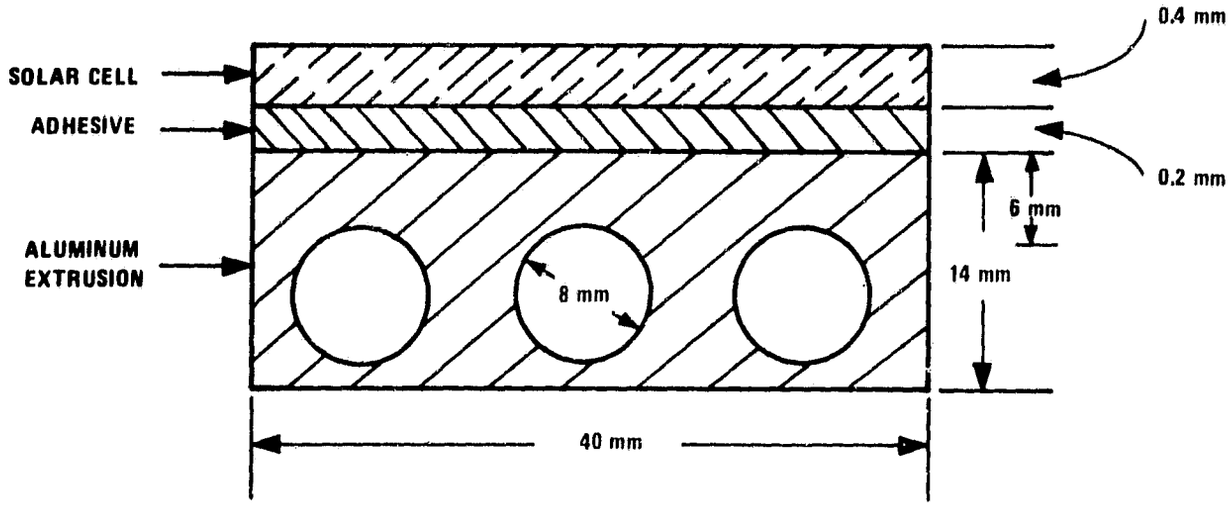

Figure 66. Solar Cell Mount Cross-Section (Not to scale.)

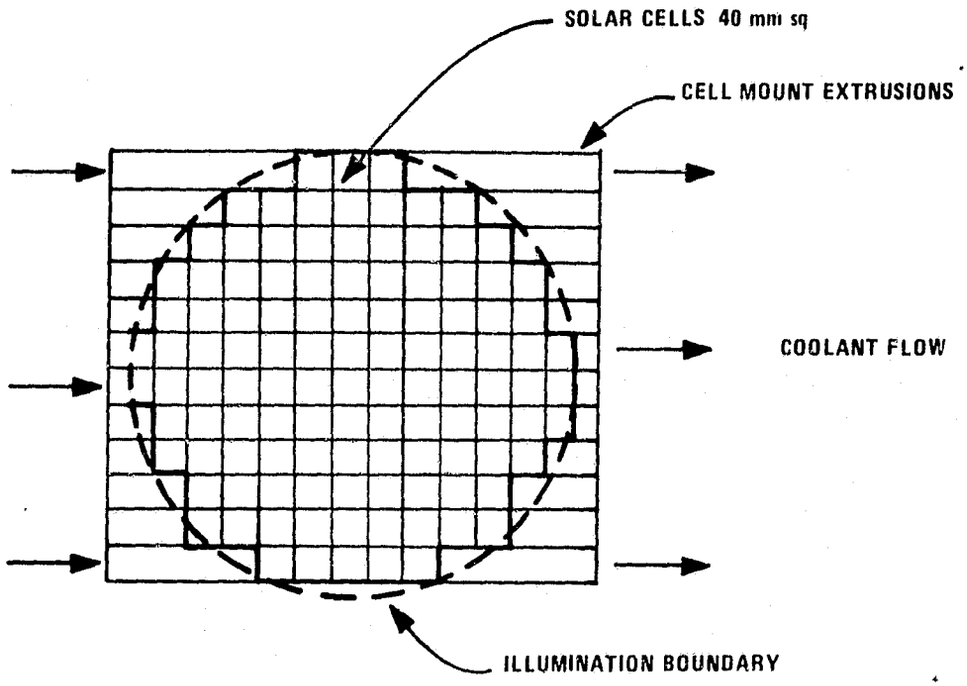

Figure 67. Placement of Solar Cells within the Focal Plane

A pure pumped convection heat transfer system was considered as the baseline system. Its performance was calculated to illustrate the methodology without regard to optimization of the design. From a thermal design standpoint, the cooling system performance is believed to represent a good approximation of the performance that can be expected from a fully optimized system. Optimization would reduce weights and may create small shifts in temperature distributions but will not strongly influence the overall size and the total cell-to-radiator temperature drop.

First consideration was given to the conductive heat transfer from the solar cell array to the coolant passageway. The assumed materials and dimensions are tabulated in Table 25.

TABLE 25. SOLAR CELL MOUNT COMPONENT DIMENSIONS

Component	Material	Thickness
Solar Cell	Silicon	0.4 mm
Adhesive	Eccobond 285	0.02 mm
Extrusion Wall	Aluminum	6 mm

The thermal properties of the mount, the heat flux and the calculated temperature drop ($\Delta T = Q/A)/(k/\Delta x)$) across each component is tabulated in Table 26.

The temperature drop between solar cell and extrusion cannot be reduced significantly further. The aluminum wall could be reduced slightly and internally finned tubes used to increase convection but substantial amounts of metal must be used to minimize lateral temperature gradients across the solar cells. The adhesive layer thickness is the most critical item since it is already very thin--0.02 mm (0.001 inch). The adhesive is a high-conductivity filled epoxy. To increase the thermal conductivity significantly would require substitution of an electrically conducting solder for the adhesive.

TABLE 26. CONDUCTIVE TEMPERATURE DROPS WITHIN THE SOLAR CELL MOUNT

Material	Conductivity (k) (W/m-K)	Conductance ($k/\Delta x$) (W/m^2-K)	Temperature Drop* (K)
Silicon	105	2.6×10^5	0.88
Adhesive	1.50	7.5×10^4	3.07
Aluminum	200	3.3×10^4	6.97
			Total 10.9K

*Heat flux (Q/A) = 23 W/cm^2.

Convective cooling of the solar cell mount poses several interesting problems. The coolant must have good thermal transport properties and have a low freezing point. While the system is in the earth's shadow with no heat input, the radiator surfaces will still be exposued to the cold space environment with no heat input. The radiators will rapidly cool, freezing most common heat-transfer fluids. The refrigerant dichlorofluoromethane (Freon-21) appears to be one of the best candidates to accommodate the wide temperature range expected. Its freezing point is 138K and at 345K its saturation pressure is only 694 kPa (100 psia).[18]

Several spacecraft heat rejection systems have been designed, using Freon-21 as the coolant, to meet system demands similar to this project,[19, 20, 21] Table 27 lists the fluid properties used to estimate the convective cooling system performance.[18]

TABLE 27. FREON-21 TRANSPORT PROPERTY DATA NEAR T = 270K

Parameter	Value
Thermal Conductivity (k)	0.124 W/m-K
Viscosity (μ)	4.4×10^{-4} Ns/m^2
Specific Heat (C_p)	1.00 J/g-K
Density (ρ)	1442 kg/m^3

[18] ASHRAE Handbook of Fundamentals. New York: American Society of Heating, Refrigerating and Air Conditioning Engineers Inc., 1967.

[19] Ellis, W.E., "Radiator Heat Rejection Options for Shuttle Payloads," ASME Paper No. 79-ENAS-18, 9th Intersociety Conference on Environmental Systems, San Francisco, California, July 1979.

[20] Nelson, W.G., and Howell, H.R., "Orbital Service Module Thermal Control System Design," ASME Paper 79-ENAS-22, 9th Intersociety Conference on Environmental Systems, San Francisco, California, July 1979.

[21] Leach, J.W., and Stalmach, D.D., "Optimum Design of Spacecraft Radiators for Large Capacity or Long Duration Mission Applications," ASME Paper 79-ENAS-10, 9th Intersociety Conference on Environmental Systems, San Francisco, California, July 1979.

The calculation of the extrusion-to-coolant film temperature drop was initiated by first assuming an allowable temperature rise in the coolant for a single pass across the solar cell array. The temperature gradient across the solar cell array must be minimized to attain high uniformity in solar cell output. Again it must be emphasized that this is not an optimized solution but only one that illustrates the significant parameters and the relative magnitudes of the temperature drops and pump work required.

The assumed physical constraints were:

Heat flux absorbed (Q/A):	$23 W/cm^2$
Extrusion-illuminated area (A):	4 cm x 56 cm
Cooling passages:	three--0.8 cm dia x 56 cm
Coolant:	Freon-21

The assumed coolant temperature rise was $T = 4.5K$. From the property data, given in Table 27, the volumetric flow $\dot{V}$ and the velocity $\bar{u}$ of the coolant was calculated

$$\dot{V} = \frac{(Q/A)\,A}{\rho C_p \,\Delta T} = 795 \text{ cm}^3/\text{sec}$$

$$\bar{u} = \dot{V}/A_c = 527 \text{ cm/sec}$$

where $A_c (= 3\,\pi (0.8/2)^2)$ is the cross-sectional area of the three flow channels.

The pressure drop for flow through the extrusion is then found by calculating the friction factor (f) which is a function of the Reynolds number (Re).[22]

$$Re = \rho \bar{u} D / \mu = 1.38 \times 10^5$$

where D (= 0.8 cm) is the diameter of the flow channel.

The friction factor given by the Filonmenko equation is

$$f = [1.82 \log_{10} (Re) - 1.64]^{-2} = 0.0168$$

and the pressure drop is given by

$$\Delta P = (f \rho \bar{u}^2 / 2) (L/D) = 2.35 \times 10^4 N/m^2 = 3.41 \text{ psi}$$

where L (= 56 cm) is the flow channel length.

The pump work required is then equal to volume flow times pressure drop:

$$W_{pump} = \dot{V} \Delta P = 18.7W$$

The film temperature drop was calculated using the Petukov equation[22] for the Nusselt number (Nu). The heat transfer coefficient (h) is a function of this dimensionless number, which is the standard form in which heat transfer data is correlated.

$$Nu = \frac{f/8 \, RePr}{1.07 + 12.7\sqrt{f/8} \, (Pr^{2/3} - 1)} = 558$$

---

[22] Karlekar, B. V., and Desmond, R. M., Engineering Heat Transfer, St. Paul: West Publishing Co., 1977.

where the Prantl number (Pr) is given by

$$Pr = \mu C_p/k = 3.55$$

For the heat transfer coefficient we have

$$h = kNu/D = 0.865\ W/cm^2\text{-}K$$

The ratio of the inner surface area of the coolant passages to the illuminated area of the extrusion is 1.88. Therefore the effective heat transfer coefficient h^* is given by

$$h^* = h \times 1.88 = 1.63 W/cm^2\text{-}K$$

The extrusion-to-coolant temperature drop ΔT_f is given by

$$\Delta T_f = (Q/A)/h^* = 14.1K$$

Pressure losses and temperature gradients in the radiator are relatively small due to the much lower flow velocities necessary to transfer heat to the radiator. The radiator temperature can be estimated by starting with the assumed solar cell temperature and subtracting each of the heat losses.

Solar cell temperature	300K
Δ T across extrusion	-10.9K
ΔT across coolant film	-14.1K
Mean coolant temp rise (4.5K/2)	-2.3K
Assume mean fin temp drop	-3K
Estimated mean radiator temp	270K

The radiator was assumed to consist of four panels inclined at an angle of approximately 60 deg from the optical axis of the telescope (see Figures 61 and 68). This arrangement allows both sides of the panel to radiate into space with a view factor of approximately 0.8. Positioning them closer to the mirror or more normal to the mirror would decrease the effective utilization of the panel surface area. The surface area of the panel required can be estimated from the equation

$$Q = A_{req} F_a \epsilon \sigma (T_{rad}^4 - T_\infty^4)$$

where

A_{req} = radiating area

F_a = view factor to space = 0.8

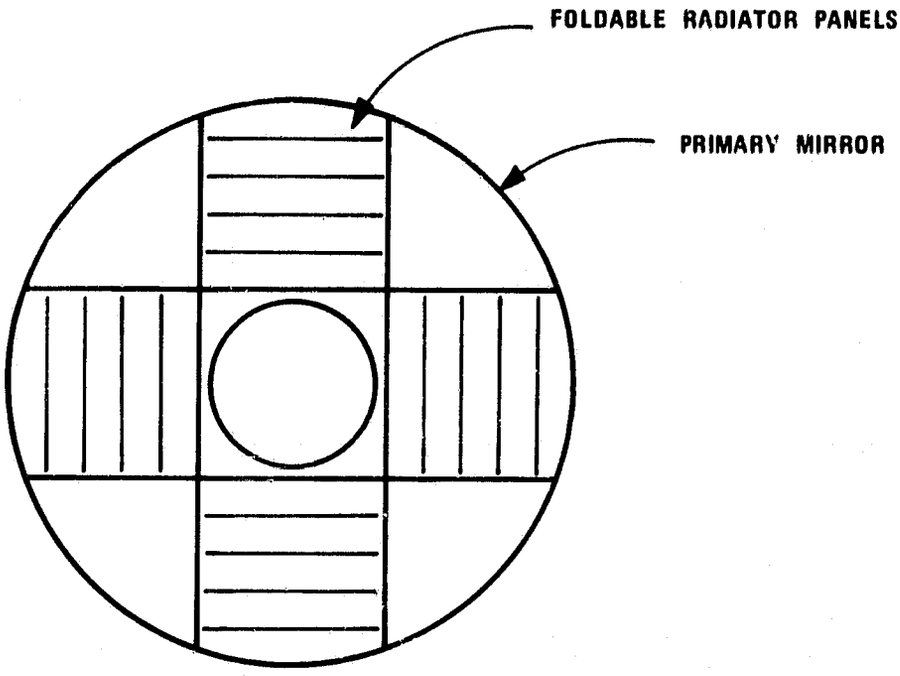

Figure 68. Radiator Panel Location (Back view)

ϵ = emittance 0.95

σ = Stephan Boltzmann constant

T_{rad} = radiator temp = 270K

T_{∞} = temperature of space $\approx$ 0

The total heat flux that must be radiated away is approximately 84 kW. Hence the required radiator area is $A_{rad} = 366\ m^2$. Since that includes both sides of the panel, the real panel area is $A_{rad} = 183\ m^2$. This amount of area can easily be placed behind the primary mirror so that it will never be illuminated by the sun.

In the analysis in Section 5, slightly different parameters were used to estimate the required radiator area. They were

$\epsilon = 1$

$F_a = 1$

$T_{rad} = 290K$

Also it was assumed that only one side of the radiator was used so $A_{rad} = A_{req}$. Hence the radiator area which should have been used in the cost analysis differs from the one used by the factor

$$\frac{(A_{rad})_{correct}}{(A_{rad})_{used}} = \frac{0.5\,[\epsilon\, F_a (T_{rad}^4 - T_{\infty}^4)]_{used}}{[\epsilon\, F_a\, (T_{rad}^4 - T_{\infty}^4]_{correct}} = 0.88$$

Hence the radiator costs used in the tradeoff analysis were about 12% higher than required.

Areas where further work must be done are in the optimization of the coolant flow necessary to cool the solar cells and in the determination of the pumping power required. No pump model or pump efficiency has been defined. Radiator panel construction and heat losses must also be considered. Cyclic temperature operation must be taken into account if the system is used in near-earth orbit and the radiator size may have to be increased significantly to radiate the heat when the system is directly between the sun and earth. Much work has been done in this area recently, in Europe and in the United States, in anticipation of upcoming space shuttle launched experiments.

REFERENCES

1. Winston, R., "Solar Concentrations of a Novel Design," Solar Energy, Vol. 16, 1974, p. 89.

2. Rabl, A., "Optical and Thermal Properties of Compound Parabolic Concentrators," Solar Energy, Vol. 18, 1976, p. 497.

3. Canning, John, S., "The Winston Solar Concentrator Described as an Ellipse," Solar Energy, Vol. 18, 1976, p. 155.

4. Hovel, H.J., Semiconductors and Semimetals, Volume 11: Solar Cells. New York: Academic Press, 1975, Chapter 3.

5. Sze, S.M., Physics of Semiconductor Devices. New York: Wiley-Interscience, 1969, pp. 24, 27, 40, 57.

6. Hovel, H.J., "Novel Materials and Devices for Sunlight Concentrating Systems," IBM Journal of Research and Development, Vol. 22, 1978, p. 112.

7. Masden, G.W., and Backus, C.E., "Increased Photovoltaic Conversion Efficiency Through Use of Spectrum Splitting and Multiple Cells," 13th IEEE Photovoltaic Specialists Conference, Piscataway, New Jersey, 1978, pp. 853-858.

8. Hamilton, B., and Peaker, A.R., "Deep-State-Controlled Minority-Carrier Lifetime in n-Type Gallium Phosphide," Journal of Applied Physics, Vol. 50, 1979, p. 6373.

9. Neuberger, M., Handbook of Electronic Materials, Vol. 12. III-V Semiconducting Compounds. New York: IFI/Plenum, 1971, pp. 68, 70.

10. Stirn, R.J., "Band Structure and Galvanomagnetic Effects in III-V Compounds with Indirect Band Gaps," Semiconductors and Semimetals, Vol. 8, Transport and Optical Phenomena. New York: Academic Press, Inc., 1972, pp. 47, 52.

11. Kittl, E.K., Lammert, M.D., and Schwartz, R.J., "Performance of GeP/N: Photovoltaic Cell at High Incident Radiation Intensity," 11th IEEE Photovoltaic Specialists Conference, Piscataway, New Jersey, 1975.

PAGE 180 INTENTIONALLY BLANK

REFERENCES (continued)

12. "150-kWe Solar-Powered Deep-Well Irrigation Facility," Final Report to ERDA, Contract No. EG-77-C-04-3918, Honeywell Energy Resources Center, Minneapolis, Minnesota, August 31, 1977.

13. Meinel, A.B., "Cost-Scaling Laws Applicable to Very Large Optical Telescopes," Optical Engineering, Vol. 18, No. 6, November-December 1979, pp. 645-647.

14. Wilkdening, H.A., "Design of a 10 kW Photovoltaic 200/1 Concentrator," 13th IEEE Photovoltaic Specialists Conference, Piscataway, New Jersey, 1978, pp. 669-672.

15. Zehr, S.W., "High Efficiency Multijunction Concentrator Solar Cells," Report No. RS 8313/203, Sandia Laboratories, Albuquerque, New Mexico, 1976, p. 29.

16. Schueler, D.G., "Status of Photovoltaic Concentrator Development," Proceedings of the Photovoltaics Advanced R&D Annual Review Meeting, Solar Energy Research Institute, Golden, Colorado, 1979, pp. 325-327.

17. Winston, R., and Welford, W.T., "Design of Nonimaging Concentrators as Second Stages in Tandem with Image-Forming First-Stage Concentrators," Applied Optics, Vol. 19, No. 3, 1980, pp. 347-351.

18. ASHRAE Handbook of Fundamentals. New York: American Society of Heating, Refrigerating and Air Conditioning Engineers Inc., 1967.

19. Ellis, W.E., "Radiator Heat Rejection Options for Shuttle Payloads," ASME Paper No. 79-ENAS-18, 9th Intersociety Conference on Environmental Systems, San Francisco, California, July 1979.

20. Nelson, W.G., and Howell, H.R., "Orbital Service Module Thermal Control System Design," ASME Paper 79-ENAS-22, 9th Intersociety Conference on Environmental Systems, San Francisco, California, July 1979.

C-3

REFERENCES (concluded)

21. Leach, J.W., and Stalmach, D.D., "Optimum Design of Spacecraft Radiators for Large Capacity or Long Duration Mission Applications," ASME Paper 79-ENAS-10, 9th Intersociety Conference on Environmental Systems, San Francisco, California, July 1979.

22. Karlekar, B.V., and Desmond, R.M., Engineering Heat Transfer, St. Paul: West Publishing Co., 1977.